79

Rydberg Atoms in an Oscillating Field: Extracting Classical Motion from Quantum Spectra

by

Neal W. Spellmeyer

B.S., University of Wisconsin, Madison
(1992)

Submitted to the Department of Physics
in partial fulfillment of the requirements for the degree of

Doctor of Philosophy

at the

MASSACHUSETTS INSTITUTE OF TECHNOLOGY

February 1998

Signature of Author_____
Department of Physics
December 5, 1997

Certified by_____
Daniel Kleppner
Lester Wolfe Professor of Physics
Thesis Supervisor

Accepted by_____
George F. Koster
Professor of Physics
Chairman, Departmental Committee on Graduate Students

Rydberg Atoms in an Oscillating Field: Extracting Classical Motion from Quantum Spectra

by

Neal W. Spellmeyer

Submitted to the Department of Physics
on December 5, 1997, in partial fulfillment of the
requirements for the degree of
Doctor of Philosophy

Abstract

We present an experimental and theoretical investigation of the connections between classical and quantum descriptions of Rydberg atoms in external electric fields. The technique of recurrence spectroscopy, in which quantum spectra are measured in a manner that maintains constant classical scaling laws, reveals the actions of the closed orbits in the corresponding classical system. We have extended this technique with the addition of a weak oscillating electric field. The effect of this perturbing field is to systematically weaken recurrences in a manner that reveals the ac dipole moments of the unperturbed orbits, at the frequency of the applied field. We outline a version of closed orbit theory developed to describe these experiments, and show that it is in good agreement with the measurements. The experiments also show good agreement with semiquantal Floquet computations. We describe a computational method that diagonalizes a Floquet Hamiltonian to compute spectra of both hydrogen and lithium in oscillating fields.

We use this new type of recurrence spectroscopy to measure classical trajectories of two closed orbits in the lithium Stark system. We extract the classical trajectories by evaluating the inverse Fourier transform of the ac dipole moment measured over some range of frequencies. Within the resolution of the experiment, the measured trajectories show excellent agreement with computed classical trajectories.

Thesis Supervisor: Daniel Kleppner
Lester Wolfe Professor of Physics

To my parents, Robert and Marjorie.

Contents

List of Figures

List of Tables

Chapter 1

Introduction

Two different theories in physics are employed to describe the physical world: classical mechanics and quantum mechanics. Classical mechanics is used to describe the motion of "large" objects: tops, baseballs, planets. Quantum mechanics is used to describe the world of the very small: atoms, molecules, crystals. Quantum mechanics is incredibly successful: it describes much more than it was ever expected to, including, it is believed, the classical world. However, it is seldom obvious how to extract information about classical motion from quantum mechanics. This thesis attempts to take another step toward this goal through an experimental and theoretical study of the behavior of lithium Rydberg states in external static and oscillating electric fields. The central result is the demonstration that the signature of a classical orbit in a quantum spectrum is diminished in an oscillating field, and that the diminishment can be related to the magnitude of the ac dipole moment of the classical trajectory. We further demonstrate how the motion of an electron in an orbit, if it moved classically, can be found from a study of its spectrum in the oscillating field.

1.1 The Semiclassical Limit

The Correspondence Principle expresses the belief that information about classical motion can be extracted from quantum systems in the so-called semiclassical limit. As originally expressed by Bohr [Boh67], the Correspondence Principle asserts the

equivalence of the frequency spectrum emitted by a quantum system and the frequencies of its classical counterpart. As discussed by Liboff [Lib84], this "frequency" correspondence is distinct from "configuration" correspondence, which asserts that in the semiclassical regime quantum probability densities correspond to their classical probability distributions. The belief that the Correspondence Principle assures that quantum mechanics reduces to classical mechanics in some limit has never been rigorously justified. Essentially, it is taken as a matter of faith. For this reason, the goal of extracting classical information from quantum systems is worth exploring.

A further subtlety is the meaning of "the semiclassical limit". This is used in various texts to mean the limit $\hbar \to 0$ or the limit of large quantum numbers. The two limits are not equivalent [Lib84]. For example, the fine structure constant $\alpha = e^2/\hbar c$ would become infinite only in the $\hbar \to 0$ limit. Here, we use "semiclassical limit" to refer to some limit, loosely defined, in which the system exhibits classical behavior.

An attempt at achieving correspondence can be made by examining the solution of the Schrödinger equation in the limit of small $\hbar$ [Tab89]. Because any complex quantity can be expressed as a real quantity times a phase, the wave function can be written as $\Psi(\mathbf{q},t) = A(\mathbf{q})e^{iS(\mathbf{q},t)/\hbar}$. This is a natural form to choose because it leads to a physical interpretation that the probability amplitude $A^2(\mathbf{q})$ obeys a continuity equation while the probability flux is proportional to the spatial variation of the phase, ∇S. For simplicity we can choose $A(\mathbf{q}) = 1$ because the amplitude A drops out in the limit below [Sak85]. With this ansatz, the Schrödinger equation becomes

$$-\frac{\partial S}{\partial t} = \frac{1}{2m}\nabla S \cdot \nabla S + V(\mathbf{q}) - \frac{i\hbar}{2m}\nabla^2 S. \tag{1.1}$$

In the limit that the term on the right is small (formally, when $\hbar \to 0$), the equation reduces to the classical Hamilton-Jacobi equation of motion,

$$-\frac{\partial S}{\partial t} = \frac{p^2}{2m} + V(\mathbf{q}), \tag{1.2}$$

where

$$\mathbf{p} = \nabla S, \tag{1.3}$$

$$S(\mathbf{q},t) = \int_{t_0}^{t} L(\mathbf{q},\dot{\mathbf{q}},t')dt', \tag{1.4}$$

and $L(\mathbf{q},\dot{\mathbf{q}},t)$ is the Lagrangian. This appears to establish a direct connection between classical and quantum mechanics. However, the formal limit of small $\hbar$ is singular because the exponent of the ansatz $\Psi(\mathbf{q},t) = e^{iS(\mathbf{q},t)/\hbar}$ oscillates rapidly as $\hbar \to 0$. Because of the subtlety of the circumstances for which the above approximation is valid, a general conclusion about correspondence cannot be made.

1.1.1 WKB and EBK Quantization

More can be learned by restricting the problem to one-dimensional time-independent systems. Assuming a solution $\psi(x) = e^{iS(x)/\hbar}$ where $S(x) = S_0 + \hbar S_1 + \cdots$ leads to a series of equations that can be solved to give the wave function. The result of the first order of approximation is of the form [Tab89]

$$\psi(x) = \frac{A}{\sqrt{p}} \exp\left(\frac{i}{\hbar}\int_{x_0}^{x} p(x')dx'\right) + \frac{B}{\sqrt{p}} \exp\left(-\frac{i}{\hbar}\int_{x_0}^{x} p(x')dx'\right), \tag{1.5}$$

where x_0 is the initial point of the trajectory. Equation (1.5) holds in the case that the de Broglie wavelength $\lambda = h/p$ is small compared with the length scale over which the potential varies [Sak85]. For a system with bound states, it can be shown that this leads to the Bohr-Sommerfeld quantization condition,

$$\oint \sqrt{2m(E_n - V(x))}dx = 2\pi\hbar(n + \frac{1}{2}). \tag{1.6}$$

This condition establishes a method for computing the quantum spectra of one-dimensional systems in terms of their classical motion.

Einstein discussed the extension of these methods to higher-dimensional systems in 1917 [Ein17]. A particle described by a Hamiltonian with n degrees of freedom can be viewed as moving in a $2n$-dimensional phase space $(q_1,\ldots,q_n,p_1,\ldots,p_n)$. Classical motion is no longer bound to one-dimensional trajectories as for Bohr-Sommerfeld quantization, but in general wanders in the multi-dimensional phase space. For integrable systems (systems for which there is a constant of motion for each degree of

freedom), the dimensionality of the problem is essentially reduced because the motion is confined to "tori" in phase space [Tab89]. The motion on these tori can be quantized with a method similar to the WKB method. Einstein realized, however, that this method could not be extended to non-integrable (chaotic) systems because tori do not exist on which to perform the quantization. In such systems, the motion wanders through all of phase space. Surprisingly, this paper was ignored for many years until it was rediscovered by Keller [Kel58, Gut90].

Shortly after Bohr's quantization of the hydrogen atom, much effort was devoted to quantizing the helium atom in a similar manner. However, the helium atom is a three-body system, composed of two electrons and a nucleus. The general motion of these particles is chaotic [Gut90], and the early attempts at quantization failed because investigators had not understood that the semiclassical quantization would not work for a chaotic system [HT93]. However, interest in this problem diminished with the introduction of the quantum mechanics of Heisenberg and Schrödinger.

1.1.2 Periodic Orbit Theory

Concern about the failure to quantize complex systems was forgotten as quantum theory developed in the 1920's and 1930's and provided other ways to understand these systems. Interest in the problem redeveloped several decades later. Great progress was made in 1970 with the introduction of the Gutzwiller Trace Formula [Gut70, Gut71, Gut90]. The quantum-mechanical solution to a time-independent Hamiltonian is given by the Green's function, $G(E, \mathbf{q}, \mathbf{q}')$ [Gut70]. It is the probability amplitude for a particle with energy E to travel from position $\mathbf{q}'$ to $\mathbf{q}$, and is related to the eigenfunctions $\phi_j(\mathbf{q})$ by [Gut70]

$$G(E, \mathbf{q}, \mathbf{q}') = \sum_j \frac{\phi_j(\mathbf{q})\phi_j^*(\mathbf{q}')}{E - E_j}, \tag{1.7}$$

where E_j are the eigenvalues of the Hamiltonian.

Gutzwiller's approach was to examine the semiclassical approximation to the *trace*

of the Green's function,

$$g(E) = \int G(E, \mathbf{q}, \mathbf{q}) d\mathbf{q} = \sum_j \frac{1}{E - E_j}. \tag{1.8}$$

The result, $g(E)$, is the density of states of the system. Information about the wave function that was contained in $G(E, \mathbf{q}, \mathbf{q}')$ is lost in the trace process, but the positions of the energy levels remain within $g(E)$, as the right hand side of Eq. (1.8) expresses. To proceed, the semiclassical approximation to $G(E, \mathbf{q}, \mathbf{q}')$ is needed. This can be shown to be given by a sum over all classical trajectories with energy E going from $\mathbf{q}'$ to $\mathbf{q}$ [Gut90],

$$G_C(E, \mathbf{q}, \mathbf{q}') = \sum_n A_n e^{iS_n(E,\mathbf{q},\mathbf{q}')/\hbar - i\mu_n \pi/2}, \tag{1.9}$$

where A_n is related to the classical density of the trajectory, S_n is its classical action, and μ_n is its Maslov index [DD88a, Gut90]. Although a rigorous derivation of this is difficult (it can be shown to follow from the Feynman path integral in the limit $\hbar \to 0$ [Gut90]), its basic form should not be surprising, for it is the same as that which arises for the wave function in WKB quantization.

The semiclassical approximation to $g(E)$ is found by taking the trace of the semiclassical approximation to the Green's function, $G_C(E, \mathbf{q}, \mathbf{q}')$. After the trace, only the periodic orbits contribute to the sum. After much consideration and math, the result can be expressed as [Gut90]

$$g(E) = \frac{1}{i\hbar} \sum_k \frac{T_k}{2 \sinh(\chi_k/2)} e^{iS_k/\hbar - i\mu_k \pi/2}, \tag{1.10}$$

where the sum is over all periodic orbits k in the system, T_k is the period of an orbit, and χ_k is a measure of its stability [Gut90]. Although challenging to implement, this formula establishes a fundamental connection between classical and quantum descriptions for both chaotic and regular systems. In contrast to EBK quantization, which gives the energy level spectrum in terms of classical action integrals, the trace formula relates modulations in the density of states to the actions of periodic orbits. There is no correspondence between an individual eigenstate and an individual orbit.

Periodic orbit theory presents a way to extract quantitatively certain properties of the classical motion. The density of states can in principle be inverted to yield the action, period, and stability of the periodic orbits through Eq. (1.10). Knowledge of the structure of the periodic orbits is key to understanding the general nature of the classical motion in a system. The trace formula therefore provides a fundamental link between quantum systems and their classical counterparts. We will learn that it also provides the motivation for the semiclassical description of Rydberg atoms in external fields.

1.2 Rydberg Atoms

The realization that highly excited "Rydberg" states of an atom can serve as an experimental testing ground for the investigation of the Correspondence Principle transformed the nature of the study of semiclassical systems. A seminal study was carried out by Garton and Tomkins in 1969 [GT69]. They measured the absorption spectrum of barium vapor in a strong magnetic field at energies above the ionization limit. They observed so-called "quasi-Landau" resonances, with an energy spacing between peaks of 1.5 times the cyclotron frequency, which is the spacing of the Landau levels of a free electron in a magnetic field. This discovery stimulated much of the subsequent work on Rydberg atoms in external fields.

Edmonds [Edm70] proposed a WKB approach to explain the quasi-Landau modulation. The idea is that while the electron can escape along the field axis, its motion is bound in the cylindrical-radial direction. WKB quantization of this radial motion gives levels whose spacing at the ionization limit is $1.5\hbar\omega_c$ This discovery motivated the quest for better semiclassical descriptions of these systems.

The introduction of the laser and atomic beam technology enabled detailed experimental studies of the structure of Rydberg atoms in electric and magnetic fields, either separately or together in parallel and perpendicular geometries. The experiments stimulated new methods for solving the quantum problem, which became increasingly feasible as computer technology advanced. However, the thrust of the research took

a new direction when Welge's group in Bielefeld, Germany, deepened the ability to understand quantum spectra in terms of classical orbits. They discovered that there were many modulations in the spectrum of hydrogen in a magnetic field, each related to a different classical orbit [MWHW86]. The first measurements were limited in the size of action (or period) of an orbit that could be resolved because the action of an orbit changed as the laser energy was scanned, and therefore the frequency at which it modulated the spectrum changed over a measurement. A breakthrough occurred in the late 1980's when the same group developed the technique of scaled energy (recurrence) spectroscopy [HMW+88]. The idea was to measure quantum spectra while simultaneously varying the laser energy and external fields so as to maintain classical scaling laws constant. A theoretical framework for interpreting such experiments, built upon the ideas of periodic orbit theory, was introduced by Delos and his collaborators [DD88b, DD88a] and by Bogomol'nyĭ [Bog89].

A number of groups have conducted recurrence spectroscopy on hydrogen and several other atoms in a variety of external fields [ERWS88, RFW91, VWH93, MWW+94, CSJK95]. Methods for measuring the action of orbits with high precision and to high action were developed by this group at MIT [CJSK94], which carried out studies of the bifurcation structure of lithium in an electric field [MWW+94, CJS+95]. However, knowledge of the orbits was essentially limited to measurements of their action, period, and stability. Little could be learned about their initial conditions or trajectories. To fulfill the promise of the Correspondence Principle, new techniques were needed to learn more about the classical motion in these systems. This thesis will demonstrate that the introduction of a field that oscillates near the frequencies of the classical motion yields information that moves one closer to fulfilling this goal. The technique makes it possible to extract the classical orbit along the direction of the oscillating field.

1.2.1 Wave-Packet Experiments

For completeness, we cite here a body of work which is complementary to this study. These are time-domain experiments in which an atom is excited by a short laser

pulse. Known as wave-packet experiments, they study classical motion by localizing the electron in a region of space and following its motion. Wave packets are created by exciting an electron to a superposition of Rydberg states so that the wave function is localized to some region of space. The motion of the wave packet can follow the classical motion for short times. However, there are some problems associated with using wave packets to recover classical motion. Because there is no equivalent to scaled energy experiments, the wave packets quickly disperse and the experiments typically reveal only a few recurrences of the electron. The experiments measure the return of the wave packet to the nucleus, but do not follow its motion while it is away from the nucleus. Wave packets were first created by localizing the electron in angular coordinates [YS88] and radially [WNLH88]. More recent experiments have observed recurrences at times corresponding to motion of wave packets localized to Kepler ellipses [GNS94] and along quasi-Landau orbits [YRM+93]. Although there is no known reason that these time-domain experiments should not be able to yield more information, it appears that new methods or ideas, similar to those of scaled energy spectroscopy, are necessary to achieve this.

1.3 Other Time-Dependent Systems

Among the very first systems used for experimental studies of the Correspondence Principle was a hydrogen atom exposed to a microwave field [BK74]. This work attempts to relate the ionization rate with the classical dynamics of the electrons. The basic idea is that chaotic motion explores large areas of phase space, and therefore a chaotic trajectory is more likely to ionize [BS87]. A review has been presented by Koch [KL95]. This is discussed further in Sec. 3.2.2.

The kicked rotor has been a paradigm in the study of chaos because it is a simple system that undergoes a transition to chaotic motion as the kicking strength becomes strong [Haa91]. This system has recently been realized experimentally using samples of ultra-cold atoms [MRB+94, RBM+95]. The momentum distributions of atoms exposed to modulated standing waves of light can be measured and compared with

classical and quantum descriptions.

1.4 Outline of the Thesis

The work here is an experimental and theoretical study of Rydberg atoms in static and oscillating electric fields. We will show that recurrences of closed classical orbits are weakened by an oscillating field, and that the extent of the weakening is related to the ac dipole moment of the orbit. Consequently, recurrence spectra recorded in oscillating fields enable the measurement of the ac dipole moment of the orbit. Such a measurement allows new information about the classical motion—in some instances the classical trajectory itself—to be experimentally determined.

Chapter 2 presents an overview of closed orbit theory for a time-independent system, and then discusses the recent extension of the ideas to the time-dependent system. Some details of the classical behavior of Rydberg atoms in electric fields are discussed to support the interpretation of experimental recurrence spectra.

Chapter 3 describes the structure of Rydberg atoms in oscillating fields from a quantum perspective. Knowledge of the quantum behavior enhances the understanding of the recurrence spectra. Computational methods based on Floquet analysis are presented, enabling the computation of recurrence spectra of hydrogen and lithium atoms in oscillating fields in some regimes. The results of these computations are described in Chapter 6.

Chapter 4 describes the experimental apparatus for measuring recurrence spectra of lithium Rydberg atoms in oscillating fields. Chapters 5 and 6 discuss the experimental results and compares them with theory. Chapter 7 demonstrates how the techniques described in the previous chapters can be used to measure with finite time-resolution the motion of two closed orbits.

Chapter 2

Semiclassical Mechanics of Rydberg Atoms in Oscillating Fields

In this chapter, we discuss a semiclassical description of a Rydberg atom in external static and oscillating electric fields. We present the Hamiltonian and show how to solve for the classical motion in this time-dependent system, continue with an overview of closed orbit theory for time-independent systems, and then describe its extension to time-dependent Hamiltonians. We conclude by examining some details of the classical dynamics of a Rydberg atom in an electric field, and discuss the effect of an oscillating field on the classical dynamics.

2.1 Hamiltonian and Classical Motion

A Rydberg atom in an external field corresponds classically to an electron moving in a Coulomb potential and external field. In this section, we consider only hydrogen. Alkali-metal atoms such as lithium can be described with the addition of a core potential due to the closed-shell electrons. However, such a description adds much complication and little insight for the purposes here. A classical, quantum, or semiclassical description of a Rydberg atom begins with the Hamiltonian. Here we

describe the Hamiltonian and discuss its classical scaling properties. To implement a semiclassical approximation to the spectrum, it is necessary to find the classical motion. Some details of this straightforward task are described at the end of this section.

We apply a static electric field F along the z axis and an oscillating electric field $F_1 \cos(\omega t + \alpha)$, also along the z axis. The Hamiltonian is

$$H = \frac{p^2}{2} - \frac{1}{r} + Fz + F_1 z \cos(\omega t + \alpha), \tag{2.1}$$

where atomic units are used, ω is the angular frequency of the oscillating field and α is its phase. For comparison with classical mechanics, it is convenient to scale[1] the Hamiltonian with the transformations

$$\tilde{r} = rF^{1/2} \tag{2.2}$$

$$\tilde{p} = pF^{-1/4}. \tag{2.3}$$

Because time obeys the scaling rule $\tilde{t} = tF^{3/4}$, we define a scaled frequency $\tilde{\omega} = \omega F^{-3/4}$. The oscillating field amplitude scales linearly with the static electric field F. We define $\tilde{f} = F_1/F$ as the scaled oscillating field amplitude. This procedure yields the scaled Hamiltonian,

$$\tilde{H} = \frac{\tilde{p}^2}{2} - \frac{1}{\tilde{r}} + \tilde{z}\left(1 + \tilde{f}\cos(\tilde{\omega}\tilde{t} + \alpha)\right) = E_0/F^{1/2}. \tag{2.4}$$

Energy is no longer conserved in this time-dependent system. We define the scaled energy as $\epsilon = E_0 F^{-1/2}$, where E_0 is the initial energy of the electron near the nucleus, where the applied fields have negligible effect.

Despite its innocuous appearance, Eq. (2.4) allows complex motion. Numerical integration of the motion is difficult because of the Coulomb singularity. This difficulty is alleviated by transforming to semi-parabolic coordinates. These were first intro-

[1]See Appendix A for a more detailed discussion of scaling.

duced in this field to study diamagnetic hydrogen [DG84]. In addition to providing a friendlier equation for integration, the semi-parabolic coordinates reveal an intimate link between this system and the system of two uncoupled anharmonic oscillators.

We define $\mu = (\tilde{r} + \tilde{z})^{1/2}$ and $\nu = (\tilde{r} - \tilde{z})^{1/2}$ and transform time in Eq. (2.4) as

$$\frac{d\tilde{t}}{d\tau} = \mu^2 + \nu^2. \tag{2.5}$$

The transformed Hamiltonian is

$$h = \frac{1}{2}\left(p_\mu^2 + p_\nu^2\right) + \frac{\mu^2 + \nu^2}{\nu^2\mu^2}p_\varphi + \frac{1}{2}\left(\mu^4 - \nu^4\right)\left[1 + \tilde{f}\cos(\tilde{\omega}\tilde{t} + \alpha)\right] - \left(\mu^2 + \nu^2\right)\epsilon - 2. \tag{2.6}$$

In this thesis we consider only $m = 0$ states, for which $p_\varphi = 0$.

The scaled action of an orbit is defined[2] as

$$\begin{aligned} \tilde{S} &= \frac{1}{2\pi}\oint \tilde{\mathbf{p}} \cdot d\tilde{\mathbf{q}} && (2.7)\\ &= \frac{1}{2\pi}\oint \left(p_\mu d\mu + p_\nu d\nu\right) && (2.8)\\ &= \left(\frac{F^{1/4}}{2\pi}\right) S, && (2.9) \end{aligned}$$

where $S = \oint \mathbf{p} \cdot d\mathbf{q}$ and the integrals are evaluated over the path of the orbit.

The Hamiltonian is integrated to find the classical motion using Hamilton's equations of motion [Gol80],

$$\begin{aligned} \frac{\partial q}{\partial \tau} &= \frac{\partial h}{\partial p} && (2.10)\\ \frac{\partial p}{\partial \tau} &= -\frac{\partial h}{\partial q}, && (2.11) \end{aligned}$$

where the coordinates (p, q) represent both (p_μ, μ) and (p_ν, ν). We have carried out the integration using a fifth-order Cash-Karp Runge-Kutta method [PTVF92]. The

[2]The factor $1/2\pi$ is special to the recurrence spectroscopy community (apparently first used in [MWHW86]). Despite the more complicated notation, we use it here because it reduces the action of the primary orbits conveniently close to 1. Note that some of our publications do not include this factor.

initial conditions for the closed orbits discussed in this thesis are $\mu = 0$, $\nu = 0$, $p_\mu = 2\cos(\theta_0/2)$, and $p_\nu = 2\sin(\theta_0/2)$, where θ_0 is the initial angle of the momentum vector measured relative to the z axis.

2.2 Closed Orbit Theory for a Time-Independent System

In this section we outline the derivation of closed orbit theory, a semiclassical approximation for the photoabsorption spectrum of a Rydberg atom in external fields. Our discussion follows that of [DD88b, DD88a]. This section addresses the time-independent system described by the Hamiltonian (2.1) with $F_1 = 0$. The following section will discuss a modified theory designed to describe the time-dependent case $F_1 \neq 0$. Periodic orbit theory cannot be directly applied to Rydberg atoms because the semiclassical approximation breaks down when the electron is near the Coulomb singularity. Closed orbit theory is a variation of periodic orbit theory that incorporates a quantum description in the region near the nucleus and connects it with a semiclassical treatment that is valid in regions far from the core. While periodic orbit theory computes a quantity (the density of states) that is difficult or impossible to measure experimentally, closed orbit theory incorporates the limited resolution of experiments by computing a finite-resolution oscillator strength.

The oscillator strength of a transition between an initial (ground) state i and an excited state f is [DD88b, BS57]

$$f_{fi} = \frac{2m_e}{\hbar^2}(E_f - E_i)|<\psi_f|D|\psi_i>|^2, \tag{2.12}$$

where E_i and E_f are the energies of the initial and final states, respectively. (In atomic units, m_e and $\hbar$ are both 1, but we include them here for clarity.) D is the dipole moment operator along the polarization direction of the excitation laser. $|\psi_i>$ and $|\psi_f>$ are the state vectors of the initial and final states, respectively.

Any experimental measurement of the spectrum has a limited resolution arising

from laser linewidth, excited state lifetime, Doppler broadening, or similar mechanisms. This limited resolution is incorporated by calculating a finite-resolution oscillator strength,

$$Df(E) = \int f_{fi}\rho(E_f)g(E - E_f)dE_f, \tag{2.13}$$

where $\rho(E)$ is the density of states (the number of states per unit energy) and $g(E - E_f)$ is a convolution function (typically a Gaussian) representing the resolution of the measurement.

Before making a semiclassical approximation to Df, we reintroduce the Green's function $G(E, \mathbf{q}, \mathbf{q}')$ described in Chapter 1. This is the wave function generated at $\mathbf{q}$ by a steady source of outgoing waves at $\mathbf{q}'$. A finite-resolution Green's function $\overline{G}(E, \mathbf{q}, \mathbf{q}')$ is related to $G(E, \mathbf{q}, \mathbf{q}')$ by the equation

$$\overline{G}(E, \mathbf{q}, \mathbf{q}') = \int G(E, \mathbf{q}, \mathbf{q}')g(E - E_f)dE_f. \tag{2.14}$$

$\overline{G}(E, \mathbf{q}, \mathbf{q}')$ is in turn related to the oscillator-strength density by [DD88b]

$$Df(E) = -\frac{2m_e}{\pi\hbar^2}(E - E_f)\mathrm{Im}<D\psi_i|\overline{G}|D\psi_i>. \tag{2.15}$$

Equation (2.15) motivates a physical picture of the excitation process. Laser light excites the electron into an outgoing wave $|D\psi_i>$. This wave propagates from the nucleus in a manner governed by the Green's function, and a fraction returns to the nucleus at later times. The oscillator strength density is proportional to the overlap of the returning wave with the continuously excited outgoing wave $|D\psi_i>$.

The development of closed orbit theory proceeds with a semiclassical approximation to the Green's function. It can be shown that this is

$$G(E, \mathbf{q}, \mathbf{q}') = \sum_n |\rho_n(E, \mathbf{q}, \mathbf{q}')|^{1/2} e^{iS_n(E,\mathbf{q},\mathbf{q}')/\hbar - i\mu_n\pi/2}, \tag{2.16}$$

where $S_n(E, \mathbf{q}, \mathbf{q}')$ is the action of a classical trajectory connecting points $\mathbf{q}$ and $\mathbf{q}'$, μ_n is the Maslov index [DD88a, Gut90], ρ_n is the classical density, which can be

found from the classical trajectories and their initial conditions [DD88b], and the index n runs over all classical trajectories with energy E that connect the two points. This approximation to $G(E, \mathbf{q}, \mathbf{q}')$ gives the value of the wave function at some final point $\mathbf{q}$ in terms of its value at an initial point $\mathbf{q}'$ and all of the trajectories with energy E that connect the two points. A similar approximation to $\overline{G}(E, \mathbf{q}, \mathbf{q}')$ can be made. However, because long-period orbits in Eq. (2.16) produce high-frequency oscillations that average to zero when $\overline{G}$ is calculated, the approximation includes only the shorter-period orbits. As the resolution of a measurement increases, longer-period orbits must be included to compute the spectrum.

The question of the conditions for which the above semiclassical approximation is valid is subtle. Near the nucleus, the potential is dominated by the Coulomb singularity, and a quantum-mechanical solution (the outgoing Coulomb wave) is necessary. At some distance (typically 50 a_0), the semiclassical approximation becomes valid. Note that this distance is somewhat arbitrary, as there is no rigorous definition of the conditions under which the semiclassical approximation holds. Reference [DD88a] has a detailed discussion showing that the semiclassical approximation does indeed hold at large distances from the nucleus. It uses the criterion that the rate of change of the de Broglie wavelength should be small relative to the length-scale of the potential. It shows that this is true everywhere away from the nucleus.

The calculation of the semiclassical approximation to the finite-resolution oscillator strength (2.13) proceeds by inserting the finite-resolution companion of Eq. (2.16) into Eq. (2.15) and simplifying. The details of the calculation are complicated and we present only the physical picture here. The outgoing wave propagates from the nucleus following classical trajectories. Two types of paths contribute to the sum. 'Direct' paths arise from trajectories that never leave the vicinity of the nucleus. 'Returning' paths arise from closed orbits that go far from the nucleus, turn back towards the nucleus under the influence of the external field, and close. The excitation probability is proportional to the overlap between the returning wave and the outgoing wave.

As Du and Delos show, the eventual result is

$$Df(E) = Df_0(E) + \sum_k C_k \sin(S_k(E)/\hbar + \gamma_k), \tag{2.17}$$

where γ_k includes the Maslov index and other details of the orbit [GD92], C_k is a measure of the overlap of the returning wave with the outgoing wave, and $Df_0(E)$ is the contribution from the direct paths. The index k in this sum is over all closed orbits, those orbits that begin and end at the nucleus. Note that there is no requirement that these orbits be periodic. In a static electric field, because of time-reversal symmetry any closed orbit with period T is also a periodic orbit with period $2T$. However, in some fields (such as crossed electric and magnetic), that symmetry does not exist and at least some of the closed orbits are not periodic [RFW91].

If the photoabsorption spectrum is measured by scanning the laser energy E, the action $S_k(E)$ changes during the scan. This means that a Fourier transform of the spectrum (2.17) will show a few peaks at low action, but the higher-action orbits will be washed out because their action varies across the scan. The solution, discovered by the Bielefield group [HMW+88], is to measure the spectrum by varying both the energy E and electric field F to maintain the scaling laws obeyed by the classical system constant, as shown by Eq. (2.4). In such a case, the scaled action $\tilde{S} = (F^{1/4}/2\pi)S$ is also constant. To describe such recurrence spectra, Eq. (2.17) must be recast in scaled variables. The result of a straightforward calculation is

$$Df(w) = Df_0(\epsilon) + \sum_k C_k \sin(2\pi\tilde{S}w + \gamma_k), \tag{2.18}$$

where $w = F^{-1/4}$. It is important to emphasize that this formula relates modulations in the oscillator strength to the actions of the closed orbits. Similarly to periodic orbit theory, it does not relate individual eigenstates to individual closed orbits.

The result (2.18) and variations that describe Rydberg atoms in other types of external fields have been extensively tested in the last decade. It provides a firm foundation for interpreting recurrence spectra in static fields.

2.3 Closed Orbit Theory for a Time-Dependent System

This section discusses the theory underlying the central goal of this thesis: an understanding of recurrence spectra in oscillating fields. Closed orbit theory, discussed in the last section, was developed for time-independent systems. The work presented in this thesis stimulated its extension to describe time-periodic Hamiltonians. The presentation in this section is based on a description given to us at MIT by Prof. John Delos in the summer of 1996 and by the subsequent papers [SKH+97, HD97].

We consider an electron moving in a Coulomb potential plus static field subject to a high-frequency laser field and a lower-frequency oscillating electric field. The electron is excited from a low-lying state ($3s$ for lithium) into a highly-excited state. The derivation of closed orbit theory begins as in the time-independent case by expressing the excitation rate or photoabsorption cross section using a purely quantum-mechanical description. A semiclassical approximation is then made that results in an expression for the photoabsorption spectrum in terms of the classical closed orbits, which now propagate in the oscillating field.

In contrast with the time-independent system, the Green's function cannot be used because energy is not conserved in a time-dependent system. Instead, this derivation uses the propagator [Sak85] to solve the time-dependent Schrödinger equation. While most of the formulas are rewritten in terms of the propagator, the underlying physical picture remains.

To find the excitation rate, we begin by expressing the excited state wave function ψ_f as

$$\psi_f(\mathbf{q},t) = \frac{1}{i\hbar}\int_{-\infty}^{t} dt' \int d\mathbf{q}' K(\mathbf{q},t;\mathbf{q}',t') H_L(t') \psi_i(\mathbf{q}',t') e^{-iE_i t'/\hbar} \tag{2.19}$$

$$\equiv \int_{-\infty}^{t} dt' F(\mathbf{q},t'), \tag{2.20}$$

where

$$F(\mathbf{q},t') = \frac{1}{i\hbar}\int d\mathbf{q}' K(\mathbf{q},t;\mathbf{q}',t') H_L(t') \psi_i(\mathbf{q}',t') e^{-iE_i t'/\hbar}. \tag{2.21}$$

The propagator $K(\mathbf{q},t;\mathbf{q}',t')$, which is related to the Fourier transform of the Green's function [DD88a], describes the evolution of the wave function of a particle that was localized at $\mathbf{q}'$ at time t' as it develops under the influence of a (time-dependent) potential. The term $H_L = De^{-i\omega_L t'}$ is the dipole moment operator associated with the laser field, and E_i is the energy of the initial state ψ_i.

The probability of finding the electron in an excited state is

$$P_f(t) = \int |\psi_f(\mathbf{q},t)|^2 d\mathbf{q} \tag{2.22}$$

$$= \int \psi_f(\mathbf{q},t)\psi_f^*(\mathbf{q},t)d\mathbf{q}. \tag{2.23}$$

The excitation rate $R_f(t)$ is the rate of increase of probability in the excited state. Consequently,

$$R_f(t) = \frac{dP_f}{dt} = \int \left(\frac{d\psi_f}{dt}\psi_f^* + \psi_f\frac{d\psi_f^*}{dt}\right) d\mathbf{q} \tag{2.24}$$

$$= 2\mathrm{Re}\int d\mathbf{q}\frac{d\psi_f^*}{dt}\psi_f \tag{2.25}$$

$$= 2\mathrm{Re}\left\{\int d\mathbf{q}F^*(\mathbf{q},t)\int_{-\infty}^{t} dt' F(\mathbf{q},t')\right\}. \tag{2.26}$$

Equation (2.26) results from the substitution of Eq. (2.20) and its derivative into Eq. (2.25).

We use Dirac notation to express the propagator as $K(\mathbf{q},t;\mathbf{q}',t') = <\mathbf{q}|K(t,t')|\mathbf{q}'>$. Then Eq. (2.21) becomes

$$F(\mathbf{q},t') = \frac{1}{i\hbar}\int d\mathbf{q}'<\mathbf{q}|K(t,t')|\mathbf{q}'>D\psi_i(\mathbf{q}',t')e^{-i(E_i+\hbar\omega_L)t'/\hbar} \tag{2.27}$$

$$= \frac{1}{i\hbar}\int d\mathbf{q}'<\mathbf{q}|K(t,t')|\mathbf{q}'><\mathbf{q}'|D\psi_i(t')> e^{-i(E_i+\hbar\omega_L)t'/\hbar}. \tag{2.28}$$

Because the states $|\mathbf{q}>$ form a complete basis, Eq. (2.28) reduces to

$$F(\mathbf{q},t') = \frac{1}{i\hbar}<\mathbf{q}|K(t,t')|D\psi_i(t')> e^{-i(E_i+\hbar\omega_L)t'/\hbar}. \tag{2.29}$$

Substitution of Eq. (2.29) into Eq. (2.26) and some algebra gives

$$\begin{aligned} R_f(t) &= 2\mathrm{Re}\int d\mathbf{q}\left[\frac{1}{i\hbar}<\mathbf{q}|K(t,t)|D\psi_i(t)>e^{-i(E_i+\hbar\omega_L)t/\hbar}\right]^* \times \\ &\quad \int_{-\infty}^{t} dt' \frac{1}{i\hbar}<\mathbf{q}|K(t,t')|D\psi_i(t')>e^{-i(E_i+\hbar\omega_L)t'/\hbar} \qquad (2.30) \\ &= \frac{2}{\hbar^2}\mathrm{Re}\int_{-\infty}^{t} dt' \int d\mathbf{q} < D\psi_i(t)|\mathbf{q}><\mathbf{q}|K(t,t')|D\psi_i(t') > \times \\ &\quad e^{i(E_i+\hbar\omega_L)(t-t')/\hbar} \qquad (2.31) \\ &= \frac{2}{\hbar^2}\mathrm{Re}\int_{-\infty}^{t} dt' <D\psi_i(t)|K(t,t')|D\psi_i(t')> e^{iE_0(t-t')/\hbar}. \qquad (2.32) \end{aligned}$$

We have used $K(t,t) = 1$ and have defined $E_0 = E_i + \hbar\omega_L$ to be the energy of the excited "outgoing" wave.

Equation (2.32) has a simple physical interpretation similar to that of Eq. (2.15). The laser light launches the electron in an outgoing wave that propagates along many paths, some of which return to interfere with the outgoing wave. Now, however, this propagation occurs in the presence of an oscillating field. As before, we make a semiclassical approximation, this time to the propagator rather than the Green's function. The approximation takes a form similar to Eq. (2.16), which approximated the Green's function with a sum over all closed orbits with energy E. Because the constraint of energy conservation is lifted, the sum for the propagator is over orbits with any energy arriving at time t that left the nucleus at some earlier time t'. Furthermore, the action is now defined in a generalized time-dependent phase space $(\mathbf{p}, \mathbf{q}, E, t)$ by

$$S_k(t) = \int_{\mathbf{q}_i,t_i}^{\mathbf{q},t} \{\mathbf{p}\cdot d\mathbf{q} - [H(\tau) - H(t_i)]\, d\tau\}\,. \qquad (2.33)$$

Note that this definition reduces to the previous definition of action in a time-independent system, $\int \mathbf{p}\cdot d\mathbf{q}$.

A long series of manipulations again leads to the semiclassical approximation to the now time-dependent excitation rate,

$$R_f(t) = R_0 + \sum_k C_k(t)\sin(S_k(t)/\hbar - \gamma_k). \qquad (2.34)$$

γ_k is a phase including the Maslov index and other details of the orbit [GD92]. An orbit k now modulates the spectrum with an action $S_k(t)$ that varies periodically in time. Equation (2.34) reduces, as it must, to the result of time-independent closed orbit theory, Eq. (2.17). Because $R_f(t)$ has a periodic component arising from $H(\tau)$ in Eq. (2.33), this excitation rate varies periodically with a frequency equal to that of the applied oscillating field. Because the experiment, which employs cw laser spectroscopy, measures a time-averaged excitation rate, the result (2.34) must be averaged over a cycle of the field to find the experimentally measured excitation rate. The result is

$$R_f = R_0 + \overline{\sum_k C_k(t) \sin(S_k(t)/\hbar - \gamma_k)}, \tag{2.35}$$

where the bar indicates a time average over a cycle of the field. This result provides a general description of the photoabsorption spectrum of a Rydberg atom in an external oscillating electric field. The physical picture is fundamentally the same as for the time-independent case. Closed orbits continue to produce sinusoidal modulations in the absorption spectrum. However, the oscillating field introduces a new variable on which the closed orbits depend. In the next section, we study some of these properties in the limit that the oscillating field is weak.

2.3.1 Behavior at Small Oscillating Field Amplitude

In this section we study Eq. (2.35) in the limit that the oscillating field amplitude is small. "Small" here means that the perturbation to the action of an orbit caused by the oscillating field is small relative to the unperturbed action and the action resolution of the experiment.

Before developing rigorous results, let us see what can be learned by simple considerations. All dynamical quantities (and in particular the action) must vary periodically with period $2\pi/\omega$. Furthermore, the amplitude of this variation must vanish as $F_1 \to 0$. Thus, it is reasonable to guess that $S_k(t) = S_k^0 + S_k^1 \sin(\omega t + \phi_k)$, where S_k^0 is the unperturbed action of an orbit k, $S_k^1 \propto F_1$, and ϕ_k is a phase. We will now show this is true, and find S_k^1 and ϕ_k.

The theory outlined in the previous section describes the absorption spectrum at a given time t, and then averages that result over a cycle of the oscillating field. At time t, orbits return to the nucleus that left at time $t - T_k$, where T_k is the period of each orbit. Here, we calculate the action of these returning orbits as a function of time, and then average over a cycle of the field.

To find $S_k(t)$, an identity which follows from classical perturbation theory is useful [DD88a]. If a Hamiltonian depends on a parameter α, then

$$\frac{dS_k}{d\alpha} = -\oint \frac{\partial H}{\partial \alpha} dt, \tag{2.36}$$

where S_k is the action of an orbit. In our case we have [HD97]

$$\frac{dS_k}{dF_1} = -\oint \frac{\partial H}{\partial F_1} dt. \tag{2.37}$$

This formula relates the perturbation to the action to an integral over the trajectory of the *unperturbed* orbit k. This is a great simplification because it makes it possible to calculate the action without taking the oscillating field into account. Consequently, the numerical calculations are simpler and faster. We write the Hamiltonian (2.1) as $H(t) = H_0 + F_1 z(t)\cos(\omega t + \alpha)$. Evaluating the derivative in Eq. (2.37) gives

$$\frac{dS_k}{dF_1} = -\int_{t-T_k}^{t} z(\tau')\cos(\omega\tau' + \alpha)d\tau'. \tag{2.38}$$

The function $z(\tau')$ is the distance along the z axis of an electron on the orbit k which left the nucleus at time $\tau' = t - T_k$ and returns at time $\tau' = t$. We make the substitution $\tau = \tau' - t + T_k$ and define the displaced function $z_k(\tau) = z(\tau + t - T_k)$ for $0 \leq \tau \leq T_k$ with $z_k(\tau = 0) = z_k(\tau = T_k) = 0$. After this substitution, integration of Eq. (2.38) with respect to F_1 yields

$$S_k(t) = S_k^0 - F_1 \int_0^{T_k} z_k(\tau)\cos[\omega(\tau - T_k + t) + \alpha]d\tau \tag{2.39}$$

$$= S_k^0 - F_1 \mathrm{Re} \int_0^{T_k} z_k(\tau) e^{i[\omega(\tau - T_k + t) + \alpha]} d\tau \tag{2.40}$$

$$= S_k^0 - F_1 \mathrm{Re}\left\{ e^{i[\omega(t-T_k)+\alpha]} \int_0^{T_k} z_k(\tau) e^{i\omega\tau} d\tau \right\} \tag{2.41}$$

$$= S_k^0 - F_1 \left| Z_k(\omega) \right| \cos(\omega t + \phi_k), \tag{2.42}$$

where $Z_k(\omega)$ is the time-integrated ac dipole moment[3] of the unperturbed orbit,

$$Z_k(\omega) = \int_0^{T_k} z_k(\tau) e^{-i\omega\tau} d\tau, \tag{2.43}$$

and the phase ϕ_k is defined by

$$\phi_k = -\omega T_k + \alpha - \arg Z_k(\omega) \; . \tag{2.44}$$

Substituting Eq. (2.42) into Eq. (2.35) gives

$$R_f = R_0 + \overline{\sum_k C_k(t) \sin\left[S_k^0/\hbar + (F_1 |Z_k(\omega)|/\hbar) \cos(\omega t + \phi_k) - \gamma_k \right]} \; , \tag{2.45}$$

where the sum is over all of the closed orbits of the unperturbed (time-independent) system. In scaled variables the excitation rate is

$$R_f = R_0 + \overline{\sum_k C_k(\tilde{t}) \sin\left[2\pi \tilde{S}_k^0 w + (\tilde{f} |\tilde{Z}_k(\tilde{\omega})| w) \cos(\tilde{\omega}\tilde{t} + \phi_k) - \gamma_k \right]} \; , \tag{2.46}$$

where[4]

$$\tilde{Z}_k(\omega) = \int_0^{\tilde{T}_k} \tilde{z}_k(\tau) e^{-i\tilde{\omega}\tau} d\tau. \tag{2.47}$$

Equation (2.46) is simplified by expanding the sine term, averaging, and using the identities [AS72]

$$J_0(z) = \frac{1}{2\pi} \int_0^{2\pi} \cos(z \sin\theta) d\theta = \frac{1}{2\pi} \int_0^{2\pi} \cos(z \cos\theta) d\theta \tag{2.48}$$

[3] A factor $1/T_k$ used in our publications is not included here. With the definition here, there is no need to know T_k to compute $Z_k(\omega)$. Furthermore, many of the formulas are simpler.

[4] The convention is to use the symbol Z_k to represent the ac dipole moment in unscaled coordinates and $\tilde{Z}_k$ in scaled coordinates.

and

$$\int_0^{2\pi} \sin(z\cos\theta)d\theta = 0, \tag{2.49}$$

yielding

$$R_f = R_0 + \sum_k C_k J_0(\tilde{f}|\tilde{Z}_k(\tilde{\omega})|w)\sin(2\pi\tilde{S}_k^0 w - \gamma_k). \tag{2.50}$$

In the spectra described in this thesis, the average value of $w = F^{-1/4}$ is much larger than the range of w over which a spectrum is measured. Consequently, w can be replaced by its average value. Because the recurrence spectrum is the absolute square of the Fourier transform of R_f, the effect of the oscillating field on the recurrence strength of an orbit k is to reduce it by a factor

$$J_0^2(\tilde{f}|\tilde{Z}_k(\tilde{\omega})|w) \equiv a_k = J_0^2(c_k\tilde{f}), \tag{2.51}$$

where

$$c_k = |\tilde{Z}_k(\tilde{\omega})|w. \tag{2.52}$$

This result plays the principal role in interpreting our experimental results. In unscaled coordinates, $a_k = J_0^2(F_1|Z_k(\omega)|/\hbar)$. Note that this makes sense dimensionally: $\hbar$ has units of action, or energy·time, while the product of F_1 and the ac dipole moment $Z_k(\omega)$ is also an energy·time.

In the next section, we will compare this prediction, which is based on perturbation theory, with exact classical calculations of the motion of an electron in an oscillating field. It will be shown that perturbation theory is valid at all field strengths studied experimentally. There will also be a brief discussion of behavior at stronger fields $F_1 \sim F$. Equation (2.51) will be tested experimentally and computationally in Chapter 6. It will be shown to give a good description of spectra in all of the regimes examined.

2.4 The Parallel Orbit

In this section we illustrate the ideas of Sec. 2.3.1 using the parallel orbits—the orbits confined to the z axis—of a Rydberg atom in an electric field. These are primitive

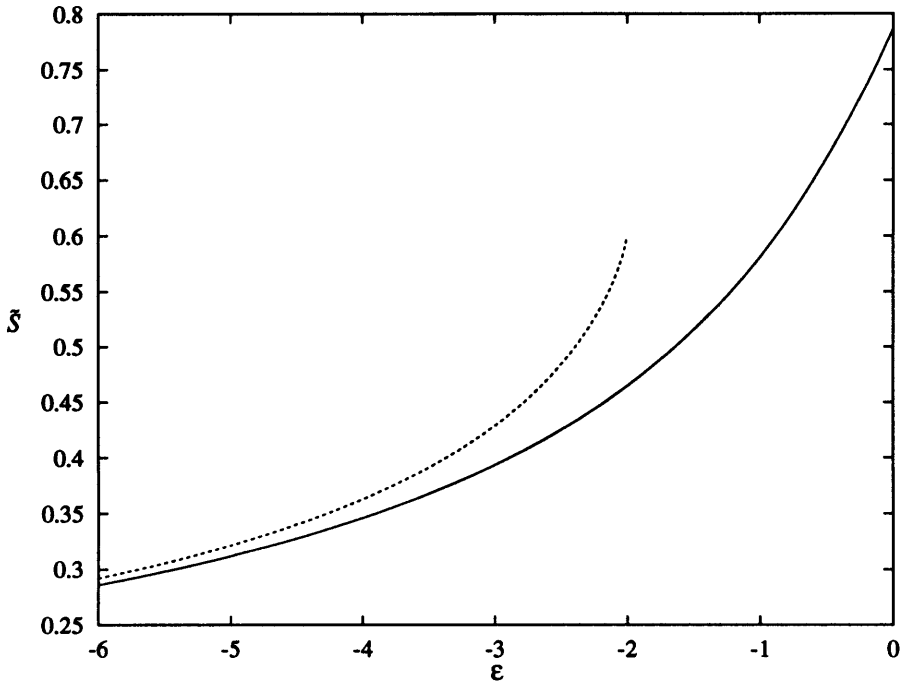

Figure 2-1: Scaled action $\tilde{S}$ of the parallel orbits U_1 (solid line) and D_1 (dashed line) vs. scaled energy ϵ. The downhill orbit ionizes for $\epsilon > 2$. The uphill orbit exists for $\epsilon > 0$, although it is unstable [GD94].

orbits of the system. Other orbits, including those we will study experimentally, bifurcate from them at particular values of the scaled energy. The family of parallel orbits is comprised of both the "downhill" orbit—the orbit that moves along the $-z$ axis—and the "uphill" orbit—the orbit that moves along the $+z$ axis. The first closure of these orbits is defined as the first repetition, denoted U_1 and D_1 for the uphill and downhill orbits, respectively. Multiple repetitions, denoted U_k and D_k, where k is the repetition number, are also closed orbits with action and period equal to an integer k times the values of the fundamental. We often use the term uphill and downhill orbit to refer to any unspecified repetition of the fundamental.

We begin with an overview of the parallel orbits in a static field. Figure 2-1 shows the scaled action of the fundamental uphill and downhill orbits, computed from Eq. (2.7), as a function of the scaled energy. The downhill orbit exists only below the saddle point energy, $\epsilon < -2$, while the uphill orbit exists for all energies, including $\epsilon > 0$. Figure 2-2 shows the period of the uphill and downhill orbits as

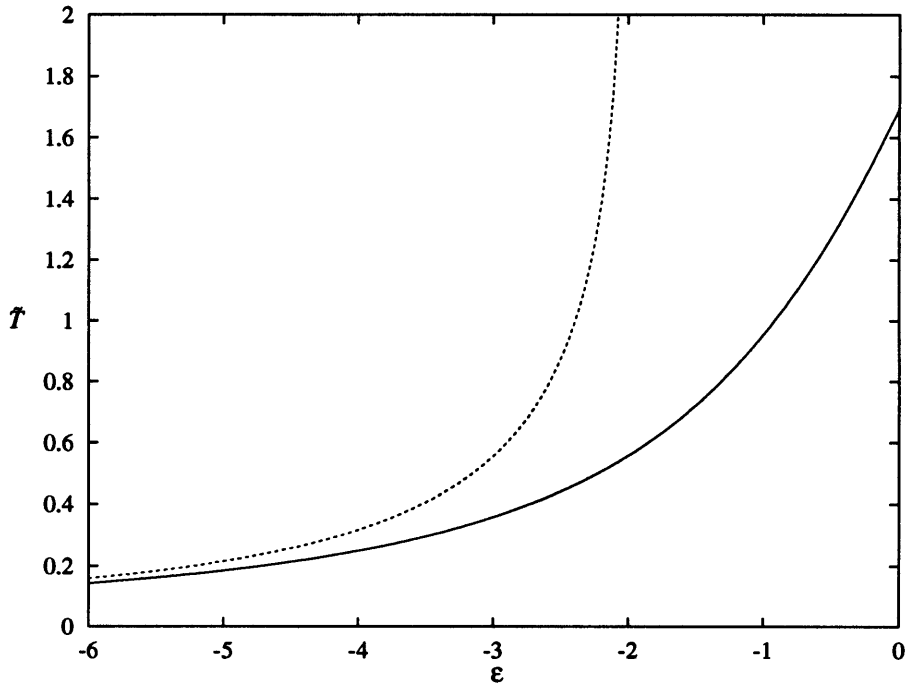

Figure 2-2: Period $\tilde{T}$ of the parallel orbits U_1 (solid line) and D_1 (dashed line) vs. scaled energy ϵ. The period of the downhill orbit becomes infinite as ϵ approaches -2. These data are related to those in Fig. 2-1 by $\tilde{T} = 2\pi\partial\tilde{S}/\partial\epsilon$.

a function of the scaled energy. The period and action were computed numerically. However, they are related by $\tilde{T} = 2\pi\partial\tilde{S}/\partial\epsilon$. The period of the downhill orbit becomes infinite as ϵ approaches -2, while the action approaches a finite value of 0.60.

Equation (2.42) predicts that the action of an orbit k in a weak oscillating field has the form $\tilde{S}_k = \tilde{S}_k^0 - \tilde{S}_k^1 \cos(\alpha + \phi_k)$, where α is the relative phase between the field and the orbit, and $\phi_k = -\arg \tilde{Z}_k$. Here we examine the robustness of this approximation, and briefly discuss the effect of non-perturbative field strengths. Our method is to compare the predictions of perturbation theory, obtained by examining the motion only in a static field, with the results of direct numerical integration of the motion that is accurate for all oscillating field strengths. The points in Fig. (2-3) show the action of the second repetition of the uphill orbit, U_2, in an oscillating field with strength $\tilde{f} = 0.001$ and frequency $\tilde{\omega} = 0.32$, computed by direct integration. One set of points shows the action defined by Eq. (2.7) in the time-independent phase

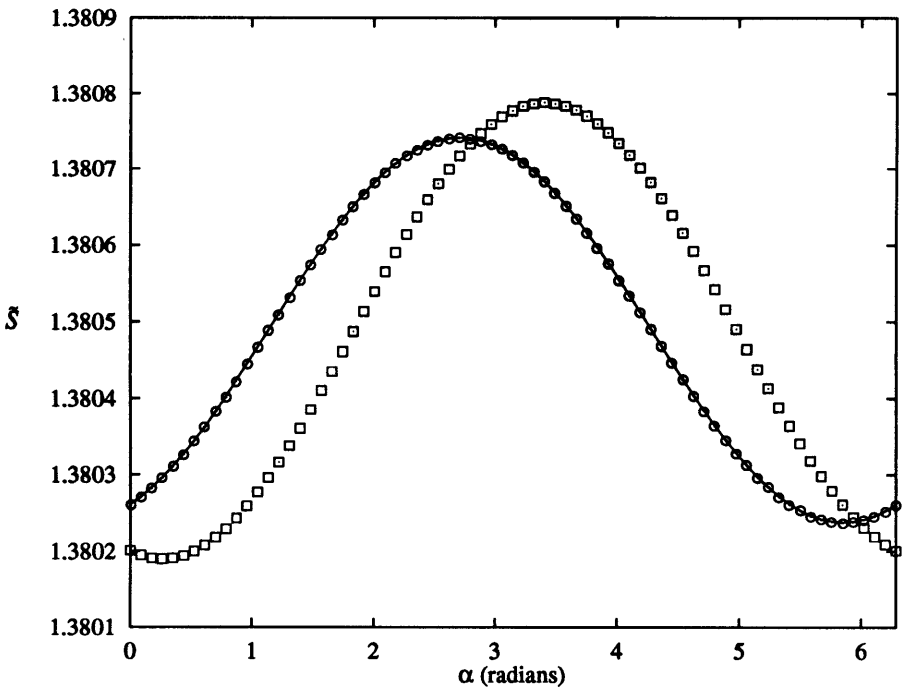

Figure 2-3: Action of the uphill orbit U_2. Circles show the action computed in the time-dependent phase space $(\mathbf{p}, \mathbf{q}, E, t)$. Squares show the action defined in the phase space $(\mathbf{p}, \mathbf{q})$. Data are calculated for $\epsilon = -0.4$, $\tilde{\omega} = 0.32$, and $\tilde{f} = 0.001$. Solid line is the prediction of classical perturbation theory, $\tilde{S} = 1.38049 - 2.52 \times 10^{-4} \cos(\alpha + 0.432)$.

space $(\mathbf{p}, \mathbf{q})$ while the other set is the generalized action defined by Eq. (2.33) in the time-dependent phase space $(\mathbf{p}, \mathbf{q}, E, t)$. Both curves show a periodic variation of the action with respect to the phase of the oscillating field. However, we will see that only the one generated from the generalized action agrees with the prediction generated from the ac dipole moment, and, as shown in Chapter 6, with the experiment.

The ac dipole moment of this orbit, computed by numerically integrating Eq. (2.43), is $\tilde{Z} = 1.436 - i0.663$, and its magnitude is $|\tilde{Z}| = 1.581$. Consequently, the action should vary sinusoidally with an amplitude $S^1 = |\tilde{Z}|\tilde{f}/2\pi = 2.52 \times 10^{-4}$, and its phase should be $\phi = -\arg \tilde{Z} = 0.432$. This prediction from perturbation theory, plotted in Fig. 2-3, shows good agreement with the numerical integration. Table 2.1 shows the action, $\tilde{S}_k^0$, and variation of action, $\tilde{S}_k^1$, of several repetitions of the uphill parallel orbit found by fitting the results of numerical integration to a sine function, and com-

Repetition, k	$\tilde{S}_k^0$	$\tilde{S}_k^1$	$2\pi\tilde{S}_k^1/\tilde{f}$	$\lvert\tilde{Z}_k\rvert$
1	0.6902	1.29×10^{-4}	0.810	0.810
2	1.3805	2.52×10^{-4}	1.583	1.581
3	2.0707	3.63×10^{-4}	2.281	2.278
4	2.7610	4.57×10^{-4}	2.871	2.872
5	3.4512	5.30×10^{-4}	3.330	3.330
13	8.9732	1.95×10^{-4}	1.225	1.223

Table 2.1: Action of several repetitions of the uphill orbit U_k for $\epsilon = -0.4$, $\tilde{\omega} = 0.32$, and $\tilde{f} = 0.001$. The right column is computed by evaluating Eq. (2.43). Perturbation theory predicts $|\tilde{Z}_k| = 2\pi\tilde{S}_k^1/\tilde{f}$.

pares the results with the computed ac dipole moment. Agreement within numerical error is found. Calculations at higher field strengths indicate that the perturbation approximation remains valid to fields of strength $\tilde{f} \sim 0.1$ at $\tilde{\omega} = 0.32$.

As the oscillating field strength increases, perturbation theory breaks down and $\tilde{S}(\alpha)$ no longer varies sinusoidally. Figure 2-4 shows the generalized action of the 5th repetition (chosen because $|\tilde{Z}|$ is particularly large for this repetition) of the parallel orbit as $\tilde{f}$ increases. For $\tilde{f}$ small, $\tilde{S}(\alpha)$ varies sinusoidally, as previously shown. The smallest amplitude curve for $\tilde{\omega} = 0.32$, which corresponds to $\tilde{f} = 0.4$, reveals sinusoidal-like behavior under close examination. As $\tilde{f}$ increases, the sinusoidal behavior breaks down, and $\tilde{S}(\alpha)$ evolves initially into a distorted sine wave before showing complex behavior at even stronger fields. The trajectories ionize for some phases and frequencies of the field. In the limit that the action-resolution of a measurement of a recurrence spectrum is less than the amplitude of variation in action, the strength of a recurrence would be calculated by performing the average over phase in Eq. (2.46). This regime has not been studied experimentally.

2.5 Bifurcations

Understanding the structure of classical bifurcations is key to interpreting recurrence spectra in the Stark system because the creation of new orbits through bifurcations

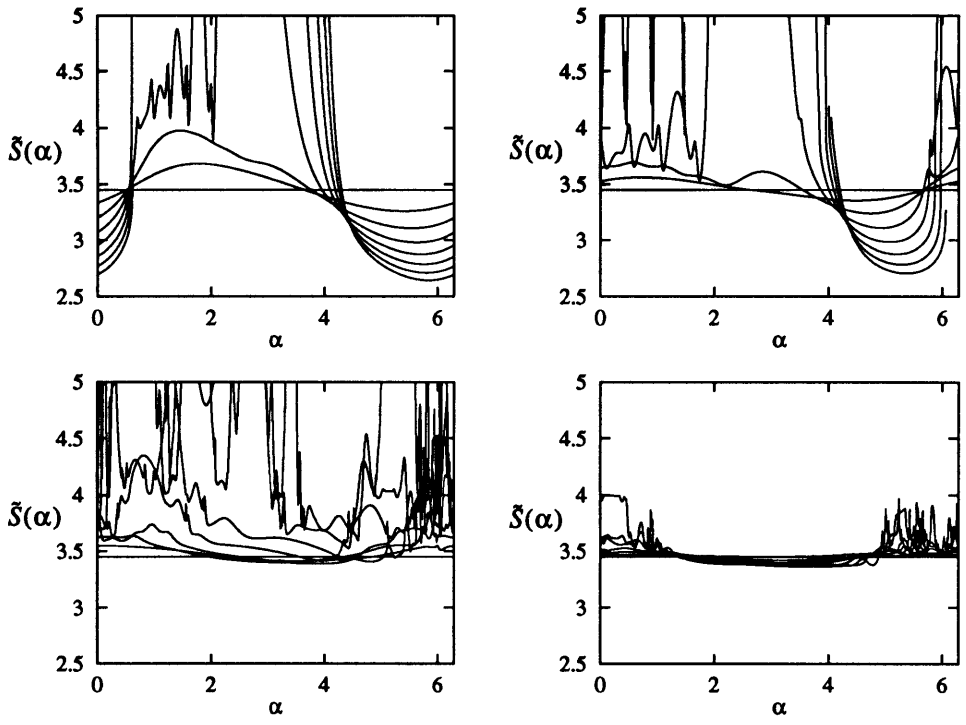

Figure 2-4: Generalized action $\tilde{S}$ of the parallel orbit U_5 vs. the relative phase α between the orbit and the oscillating field. Data are calculated for $\epsilon = -0.4$. In each plot $\tilde{f}$ increases from 0 to 2.8 in steps of 0.4. Top left: $\tilde{\omega} = 0.32$. Top right: $\tilde{\omega} = 0.64$. Bottom left: $\tilde{\omega} = 4.654$ (resonant frequency of the first repetition U_1). Bottom right: $\tilde{\omega} = 10.0$. There are no lines at some phases and field strengths where the electron has ionized.

generates strong recurrences in the spectra and determines the evolution of the spectra as the scaled energy changes. Bifurcations, described in detail in [GD94], are easiest to understand in the oscillator representation discussed in Sec. 2.1, in which the Hamiltonian separates in semi-parabolic coordinates into two anharmonic uncoupled oscillators. Motion along the μ axis corresponds to motion along $+z$—the uphill orbit, while motion along ν corresponds to motion along $-z$—the downhill orbit.

The general motion of a trajectory corresponds to simultaneous motion along μ and ν. Over certain ranges of scaled energies, orbits launched at an appropriate angle make exactly m cycles of motion along ν for every n cycles of motion along μ. These orbits are labeled by the ratio of their periods, m/n. As the energy is decreased, each particular closed orbit springs into existence at a specific value of energy in a process known as a bifurcation. Just after the bifurcation, the orbit is nearly identical to the uphill orbit. As the energy is further decreased (made more negative), the orbit fattens out in the radial direction, and then stretches out along the $-z$ axis, until it disappears in a bifurcation into the downhill orbit.

Figure 2-5 illustrates the generation of new orbits by bifurcations, and gives a simple overview of the evolution of orbits in the spectrum. It shows the action of several closed orbits in an electric field, found by numerical integration of the classical equations of motion. A trajectory is launched from the nucleus at some angle θ, and then again at $\theta + d\theta$. As the electron propagates, it passes near the nucleus, and its distance along the μ or ν axis is recorded. If this distance changes sign, it means the orbit closes when launched at some angle between θ and $\theta + d\theta$. This angle is subsequently converged on. The success of this method is determined by the step size in θ. For these calculations, a fairly coarse step size was taken, so not all the orbits (for instance, the 1/3) are found at all energies.

As ϵ decreases, the m/n orbit approaches the downhill orbit and eventually collides with the mth repetition D_m, where it disappears in a bifurcation. The values of allowed period ratios as a function of ϵ are given in Fig. 2-6, which is reproduced from [GD94, CSJK95]. (Alternatively, as the energy is increased, the mth repetition of the downhill orbit fans out into the orbits with period ratio m/n with $n > m$.

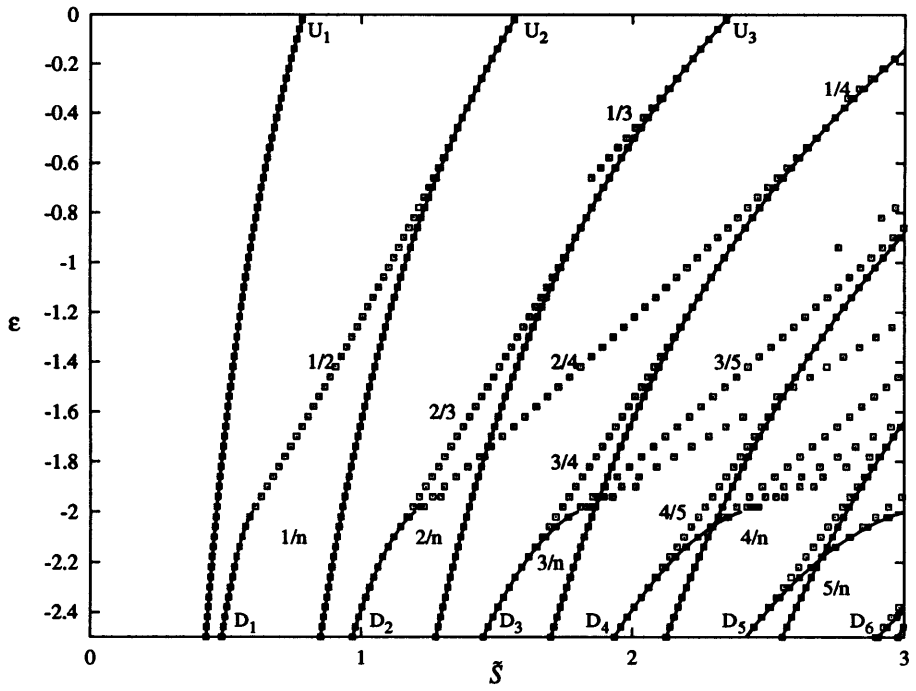

Figure 2-5: Scaled actions $\tilde{S}$ of orbits vs. scaled energy ϵ. The squares are the actions found by numerically searching for orbits. The solid lines extending from top to bottom are the actions of the uphill orbits U_k, which are labeled along the top. The lines extending from the bottom to $\epsilon = -2$ are the actions of the downhill orbits D_k, which are labeled along the bottom. As ϵ decreases, orbits with period ratio m/n bifurcate from the uphill orbits U_n. Near $\epsilon = -2$, these orbits m/n bifurcate into the downhill orbits D_m. The fractions identify some of the bifurcated orbits, and the labels $1/n, 2/n, \cdots$ indicate individual families of bifurcated orbits.

Each of these orbits eventually collides with a repetition of the uphill orbit. From this perspective, D_m generates all the orbits with period ratio m/n where $n > m$.)

An enhancement of recurrence strength is associated with a bifurcation. Indeed, closed orbit theory diverges at a bifurcation, and quantum-mechanical diffraction-like effects must be incorporated. This is examined in detail in [CJS+95, GD97]. There is a simple physical way to understand this enhancement in recurrence strength. The strength is related to the stability of an orbit. If the initial angle of an orbit changes slightly, the orbit still returns close to the nucleus if the orbit is stable. Measuring the stability of the nth repetition of the uphill orbit means launching it at a slight

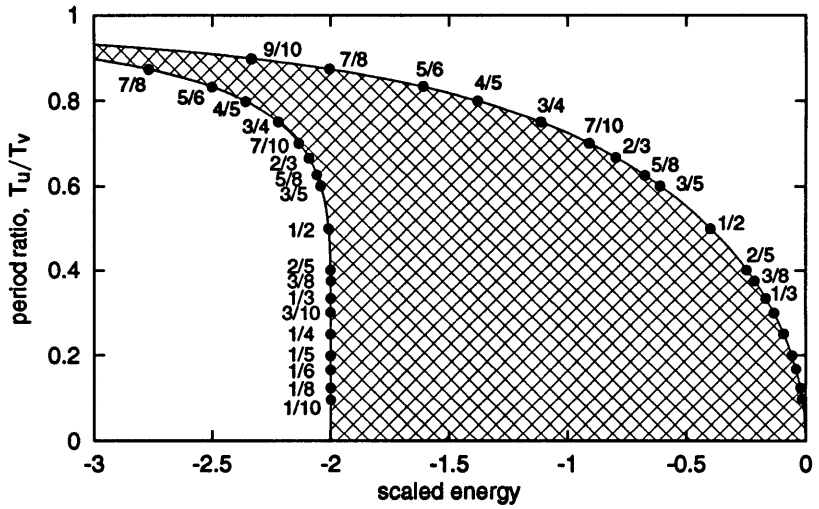

Figure 2-6: Winding numbers m/n of closed orbits. As ϵ decreases below -2, there is a sequence of bifurcations in which orbits m/n disappear in a bifurcation with the downhill orbits D_m. Orbits with period ratios m/n exist in the hatched region between the two curves. (Figure reproduced from [CSJK95].)

angle to the z axis, so there is a small component of motion along the ν direction. The orbit returns close to the nucleus after n cycles of motion along μ. If the energy is near a bifurcation point, then orbits with period ratios m/n close, so the m cycles of ν motion bring the perturbed uphill orbit back near the nucleus, and it has a large recurrence strength. The return of orbits at the bifurcation corresponds to the focusing of light in optics. The intensity of light in a focus in geometrical optics is infinite. This intensity is reduced to a finite value in any real system by diffraction effects. The recurrence strength at a bifurcation is similarly reduced to a finite level by quantum-mechanical diffraction effects of the waves returning to the nucleus.

2.6 Chaos

The classical dynamics of hydrogen in a static electric field is regular because the Hamiltonian is separable. However, the fundamental nature of the system is changed when the Hamiltonian is time-dependent. Energy is no longer a constant of motion, and in some circumstances the motion can be chaotic. Because the electron moves

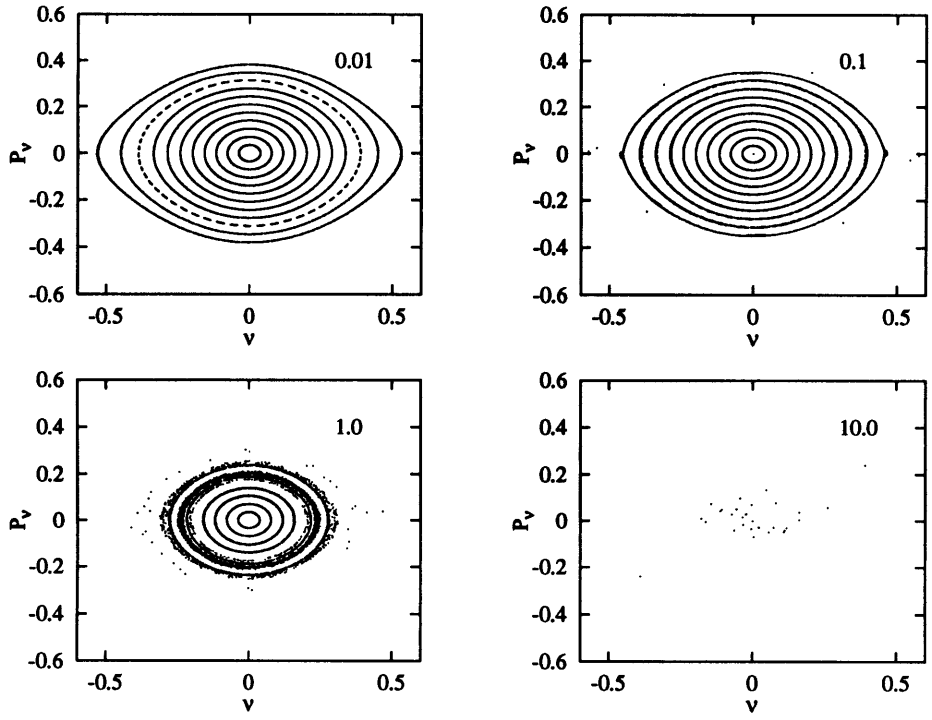

Figure 2-7: Surfaces of section in an oscillating field, $\epsilon = -0.4$, $\tilde{\omega} = 0.32$. $\tilde{f}$ is labeled on each plot.

in a 6-dimensional phase space $(\mathbf{p}, \mathbf{q}, E, t)$, it is challenging to achieve a simple understanding of its behavior. A standard technique for characterizing motion in a time-independent system is the Poincaré surface of section. A surface of section is generated by launching trajectories with many initial conditions and taking a slice through the phase space by recording say (ν, P_ν) when the electron crosses the (ν, P_ν) plane. Here we choose to extend this method to a time-dependent system by ignoring (projecting out) the coordinates (E, t) and recording (ν, P_ν) when the trajectory crosses the (ν, P_ν) plane with $P_\mu > 0$. (An alternate method is to stroboscopically record the position and momentum of the particle at one point in each cycle of the oscillating field [GK87]. Although this method works well in systems with only one spatial degree of freedom, its application here would require that one of the spatial degrees of freedom be projected out, and therefore does not provide a simplification for our system.)

Figure 2-7 shows surfaces of section generated for a particular energy and fre-

quency as $\tilde{f}$ is increased. Trajectories were launched from the nucleus at 45 different initial angles uniformly distributed between $[0, \pi]$. For $\tilde{f} < 0.1$, the tori on which the motion is bound for $\tilde{f} = 0$ are not noticeably affected by the oscillating field. As $\tilde{f}$ approaches 1, some tori break up, suggesting chaotic motion. For $\tilde{f} = 10$, all the tori have been destroyed. Note that at large $\tilde{f}$, most of the trajectories ionize.

The development of chaos in this problem is likely to be similar to that in hydrogen in an oscillating field with no static field, for the problems are the same for $\tilde{f} \gg 1$. The microwave ionization of hydrogen and the role of chaos has been extensively studied in [KL95]. Chaos arises in the following way. In a static field the motion of an electron is composed of a set of Fourier components. If a periodic perturbation is resonant with one of these components, the motion is affected. However, the system is a non-linear oscillator because the period of motion depends on the energy. As the electron is resonantly affected, its motion moves away from the frequency of the perturbation, and nonlinear stabilization occurs [CCSG87]. In these circumstances, the motion remains close to the original orbit. However, if the perturbation is strong enough, the motion can be driven into another resonance region (a harmonic of the perturbation). This process can repeat, generating both chaotic motion and ionization.

In lithium, a second process can cause chaos. The core electrons generate chaos through the process of core-scattering. An electron incident on a pure Coulomb potential perfectly back-scatters, whereas an electron incident on the non-hydrogenic lithium core can scatter into another orbit with some other initial angle. Such a process generates new sets of orbits at all combinations of hydrogenic orbits. This results in a proliferation of orbits as the action increases. Such a proliferation is a signature of chaotic motion. This effect was first seen experimentally and computationally in diamagnetic helium [DMDT95, HMW95] and in the lithium Stark system [CJSK94]. This effect is of little importance in the experiments; it is most apparent at high action and low energy, whereas the experiments here concentrate on high energy or low action. Section 6.4 examines computed recurrence spectra for lithium in a region of core-scattering.

Chapter 3

Quantum Mechanics of Rydberg Atoms in Oscillating Fields

We have discussed the classical and semiclassical behavior of a Rydberg atom in static and oscillating fields, but it is essential to understand the quantum-mechanical behavior in order to perform the experiment and interpret the results. The discussion here begins with the thoroughly investigated Stark structure of a Rydberg state, continues with Stark structure in an oscillating field, and concludes with a description of the Floquet method for computing the structure of hydrogen and alkali-metal Rydberg atoms in parallel or perpendicular oscillating fields.

3.1 Stark Effect

An isolated Rydberg atom has energy levels given by $E_n = -1/[2(n-\delta_l)^2]$, where n is the principal quantum number and δ_l is the angular-momentum-dependent quantum defect. In hydrogen, for which $\delta_l = 0$, each of these levels is n^2 degenerate (ignoring spin). In an alkali-metal atom, for which the value of δ_l is often significant only for the lowest few l values, this complete l-degeneracy is lifted. An electric field shifts the energy levels and lifts the degeneracy (or remaining degeneracy for an alkali-metal atom) for states with a given value of $|m|$, where m is the component of angular momentum along the z axis. For a state in hydrogen with principal quantum number

n, the energy to first order in the electric field F is [BS57]

$$E_n(n_1, n_2) = -\frac{1}{2n^2} + \frac{3}{2}n(n_1 - n_2)F, \tag{3.1}$$

and n_1 and n_2 are the parabolic quantum numbers, which satisfy the relation

$$n = n_1 + n_2 + |m| + 1, \tag{3.2}$$

where $n_1, n_2 \geq 0$. Higher-order terms become important at higher field strengths. The energy to second order in F is [BS57]

$$E(F) = E_n(n_1, n_2) - \frac{1}{16}F^2n^4[17n^2 - 3(n_1 - n_2)^2 - 9m^2 + 19]. \tag{3.3}$$

This formula and higher-order formulas (up to 10th order) have been tested extensively and show good agreement with experiments [Koc78], although the perturbation analysis is complicated by the need for sophisticated summation techniques to incorporate the divergence of high-order terms.

The Stark structure of alkali-metal atoms is similar to hydrogen, but there are some important differences. At low field strengths, the low l states, depressed to lower energy by the quantum defects, exhibit a second-order Stark shift for weak fields. The shift becomes linear only after F has become large enough that the state mixes with the higher l states. Figure 4-12 illustrates this mixing for the $n = 31$ state of lithium.

3.2 Ionization

In an electric field a Rydberg atom always ionizes on some time scale because there are no stationary solutions of the Hamiltonian. In many cases, however, the time scale is so long that ionization can be neglected. An oscillating electric field can drastically change the ionization behavior. There have been many detailed studies of the behavior of Rydberg atoms in strong microwave fields, a subject known as microwave ionization. We will see that such effects are largely unimportant for the

regimes studied in this thesis. The discussion here is based on that in [Gal92, Gal94]. We begin, however, by discussing ionization in a static electric field.

3.2.1 Static Field Ionization

The potential produced by an electric field along the z axis is unbound for $z \to -\infty$. Hydrogen ionizes classically when its energy is high enough that the electron can travel out along the $-z$ axis over the saddle point, a local maximum in the potential created by the combination of the electric and Coulomb potentials. For $m = 0$ states, which lack a centrifugal barrier, classical ionization occurs when $F > E^2/4$.[1] If the energy shift produced by the electric field is ignored, this simple model implies a critical field $F_{\rm sp} = 1/16n^4$. Actual ionization processes are more complicated than this classical analysis suggests. The ionization rate depends on the spatial distribution of the wave function of a state. For example, high-energy 'blue' states, localized away from the saddle point, are harder to ionize than low-energy 'red' states localized near the saddle point. Ionization can occur at fields below the classical saddle point by tunneling through the potential barrier.

The ionization properties of alkali-metal atoms in electric fields differ markedly from those for hydrogen atoms. In addition to the presence of hydrogenic ionization processes, there is a second type of ionization process created by the ionic core. Because the core destroys the separability of the Schrödinger equation, n_1 and n_2 are no longer good quantum numbers. The high-energy blue state of one n-manifold interacts with the low-energy states of the higher-lying manifolds. Consequently, a blue state that may be stable in hydrogen may ionize in an alkali-metal atom.

3.2.2 Microwave Ionization

A large body of literature exists describing Rydberg atoms exposed to oscillating fields for which the frequency and field amplitude are scaled by the principal quantum number n [LP78, KL95]. The characteristic frequency is the frequency of an electron

[1] This corresponds to a scaled energy $\epsilon = -2$.

moving in a Bohr orbit, $\omega = 1/n^3$, and the characteristic field is the atomic field seen by the electron, $F = 1/n^4$. This gives a scaled frequency $\omega_0 = n_0^3\omega$ and a scaled field strength $F_0 = n_0^4 F$ [BD95]. The scaled frequency and field amplitude used in this thesis are related to these scalings by $\tilde{\omega} = \omega_0(2\epsilon)^{3/2}$ and $\tilde{f} = 4\epsilon^2 F_0$. Such scaling laws are convenient for the ionization experiments because they typically focus on behavior near a single n state, whereas recurrence spectroscopy involves scans over many n states.

The ionization properties of alkali-metal atoms differ significantly from those of hydrogen because of additional couplings introduced by the core. We first examine the ionization properties of Rydberg atoms in a microwave field, and then consider the effect of the presence of a static field.

When the frequency is smaller than the inter-manifold spacing ($\omega < 1/n^3$), hydrogen ionizes if the oscillating field is large enough to ionize the red state of a Stark manifold. This occurs for an oscillating field amplitude equal to the static field strength required for ionization, $F = 1/9n^4$. The other states in the manifold, which would not ionize in a static field of this strength, ionize by coupling to the red state through the second-order Stark effect. As the field oscillates, the population of a given state is redistributed within the manifold. A fraction of the population is transferred into the ionizing red state with each cycle of the field. After many cycles, the atom will have ionized.

As ω approaches $1/n^3$, electric dipole transitions connect adjacent n-manifolds. Consequently, a state with low n makes transitions to higher n states. The atom ionizes when n becomes large enough that the amplitude of the oscillating field equals the static ionizing field strength.

States of alkali-metal atoms with non-negligible quantum defects ionize at much smaller fields with amplitudes $F = 1/3n^5$. This can be understood in the following way. The quantum defect introduces anti-crossings between extreme red and blue states of adjacent Stark manifolds at field strengths $F = 1/3n^5$. The oscillating field induces Landau-Zener transitions from the lower to higher state. Transitions can be driven to yet higher states because the critical anti-crossing field grows smaller as n

increases. Eventually, n becomes large enough that the oscillating field amplitude is large enough to directly ionize the state over the electric field saddle.

The presence of a static electric field can significantly change the ionization properties. The static field creates a first-order intra-manifold spacing $\frac{3}{2}nF$. If the frequency is close to this spacing, a weak field can drive electric dipole transitions between these states, connecting a non-ionizing state to another ionizing state. This sets a condition $\hbar\omega < \frac{3}{2}nF$ for ionization rates to be small. We emphasize, however, that the present work is at a low oscillating field strength regime, where microwave ionization is not an important effect.

3.3 Stark Structure in an Oscillating Field

We need to understand Stark structure in an oscillating field because we use this structure to calibrate our oscillating field strength. We begin by finding the energy level structure of a Rydberg atom in a weak oscillating field parallel to the static field. In such a field, the Stark Hamiltonian is diagonal in the parabolic basis. This regime allows analytic solutions to be found that encapsulate the fundamental behavior of Rydberg atoms in an oscillating field.

The description given here follows Gallagher [HKTG84, Gal94]. Consider a Rydberg state of hydrogen in an external electric field F and an oscillating electric field F_1, both along the z axis. The Hamiltonian is

$$H = \frac{p^2}{2} - \frac{1}{r} + Fz + F_1 z\cos(\omega t), \tag{3.4}$$

where we have chosen the phase of the field to be zero without loss of generality. For $F_1 = 0$, the eigenstates of H are

$$|\psi(\mathbf{r},t)> = |\psi(\mathbf{r})> e^{-i(E+kF)t}, \tag{3.5}$$

where E is the energy of the state when $F = 0$ and $k = \partial E/\partial F$ is the slope of the Stark state. For hydrogen, $k = \frac{3}{2}n(n_1 - n_2)$. For alkali-metal atoms, the slope can be

found through quantum computations similar to those described in the next section, but done in a static electric field.

We make the approximation that the oscillating field does not couple states from the same or other n-manifolds. Within this approximation, the time dependence of a state in the oscillating field can be expressed as

$$|\psi(\mathbf{r},t)> = |\psi(\mathbf{r})>T(t). \tag{3.6}$$

The time evolution of $|\psi(\mathbf{r},t)>$ is given by the time-dependent Schrödinger equation,

$$H|\psi> = i\hbar\frac{\partial}{\partial t}|\psi>. \tag{3.7}$$

Substitution of Eq. (3.6) into Eq. (3.7) yields

$$[E + kF + kF_1\cos(\omega t)]\,T(t)|\psi(\mathbf{r})> = i\hbar\dot{T}(t)|\psi(\mathbf{r})>. \tag{3.8}$$

This differential equation has a solution

$$T(t) = e^{-i\int[E+kF+kF_1\cos(\omega t')]dt'/\hbar} = e^{-i[(E+kF)t/\hbar+\frac{kF_1}{\hbar\omega}\sin(\omega t)]}, \tag{3.9}$$

from which it follows that

$$|\psi(\mathbf{r},t)> = |\psi(\mathbf{r})>e^{-i[(E+kF)t/\hbar+\frac{kF_1}{\hbar\omega}\sin(\omega t)]}. \tag{3.10}$$

The oscillating field modulates the energy of the state about its unperturbed value with a frequency ω. Just as FM modulation in radio adds side bands to the spectrum, the oscillating field here adds side bands to the states. Using the relation [AS72]

$$e^{ix\sin\omega t} = \sum_{q=-\infty}^{+\infty} J_q(x)e^{-iq\omega t}, \tag{3.11}$$

we can express the wave function as

$$|\psi(\mathbf{r},t)> = |\psi(\mathbf{r})>e^{-i(E+kF)t} \sum_{q=-\infty}^{+\infty} J_n\left(\frac{kF_1}{\hbar\omega}\right) e^{iq\omega t}. \tag{3.12}$$

Several observations are appropriate. Each state is split into an infinite manifold of states having the same spatial behavior, which is unaffected by the oscillating field. The states have energies $E + kF - q\hbar\omega$ with amplitudes given by a Bessel function. Because $J_q(x) \approx 0$ for $|q| > x$, sidebands are significant only for $|q|\hbar\omega < kF_1$.

3.4 The Floquet Method

The preceding section provides a useful framework for describing Rydberg atom behavior in an oscillating field, but is not adequate for describing alkali-metal Rydberg atoms in realistic experimental circumstances. It does not treat situations in which there is n-mixing, does not incorporate an ac Stark shift of the levels [STG88], and is not easily adapted to more complex geometries such as an oscillating field perpendicular to the static field. We now present a more general approach, known as Floquet analysis [Shi65, Sam73, STG88, BGD94], that overcomes these limitations. The basic idea, as in the previous section, is that the solution of the Schrödinger equation for a time-periodic Hamiltonian is itself time periodic. This means that the wave function can be Fourier decomposed into components oscillating at the frequency of the oscillating field and its harmonics. (The method can also be extended to the diamagnetic system, although we do not discuss this here.)

We consider a time-periodic Hamiltonian $H(t)$. Its solution $|\Psi(\mathbf{r},t)>$ obeys the time-dependent Schrödinger equation, (3.7). We assume a solution $|\Psi(\mathbf{r},t)> = e^{-i\epsilon t/\hbar}|\psi(\mathbf{r},t)>$. Upon substitution into Eq. (3.7), one finds an eigenvalue equation:

$$\left[H(t) - i\hbar\frac{\partial}{\partial t}\right] |\psi(\mathbf{r},t)> = \epsilon|\psi(\mathbf{r},t)>. \tag{3.13}$$

The eigenvalue ϵ is often known as the quasi-energy. Some properties of the quasi-energy and its relationship to the mean energy of a system are discussed in [FMR78].

Now, let us specialize to a Rydberg atom, for which the Hamiltonian is

$$H(t) = H_0 + Fz + F_1 z\cos(\omega t). \tag{3.14}$$

We separate the Hamiltonian in this form because the eigenstates of the field-free Hamiltonian, H_0, are known for both hydrogen and alkali-metal atoms [ZLKK79]. We label the eigenstates of H_0 as $|k>$, i.e., $H_0|k> = E_k|k>$, where k represents the atomic quantum numbers n, l, and m. (Note that the k used here is different from the k used in the previous sections to represent the slope of a Stark state.)

Floquet's theorem [Shi65] asserts that any solution to Eq. (3.13) can be expressed as

$$|\psi(\mathbf{r},t)> = \sum_{r,k} C_{r,k} e^{-ir\omega t}|k>. \tag{3.15}$$

This is merely saying that a system with a periodic Hamiltonian must have a periodic solution and that this solution can be expressed as a discrete Fourier series. We substitute Eq. (3.15) into Eq. (3.13) and multiply on the left by $<j|$ to find

$$\begin{aligned}\sum_r \Bigg(C_{r,j}E_j e^{-ir\omega t} \;&+\; \sum_k F z_{j,k} C_{r,k} e^{-ir\omega t} \\ + \sum_k F_1 z_{j,k} C_{r,k} \cos\omega t e^{-ir\omega t} \;&-\; r\hbar\omega C_{r,j} e^{-ir\omega t}\Bigg) = \epsilon \sum_r C_{r,j} e^{-ir\omega t},\end{aligned} \tag{3.16}$$

where $z_{j,k} =< j|z|k >$.

We now remove the time-dependence from this equation. This is done by evaluating another inner product formed by multiplying by $e^{iq\omega t}$ and integrating with respect to ωt. The inner product is simplified with the orthogonality condition

$$\int_0^{2\pi} d(\omega t) e^{iq\omega t} e^{-ir\omega t} = 2\pi\delta_{q,r}, \tag{3.17}$$

where $\delta_{q,r}$ is the Kronecker delta function. A little algebra finally gives

$$(E_j - q\hbar\omega)\, C_{q,j} + \sum_k \left[F z_{j,k} C_{q,k} + \frac{F_1 z_{j,k}}{2} \left(C_{q-1,k} + C_{q+1,k}\right)\right] = \epsilon C_{q,j}. \tag{3.18}$$

The $q+1$ and $q-1$ terms result from the cosine term expressed as $\cos\omega t = (e^{i\omega t} + e^{-i\omega t})/2$. This equation defines a time-*independent* matrix that can be diagonalized to yield eigenvalues ϵ and eigenvectors $\{C_{q,k}\}$. In the spherical basis, the terms along the diagonal are the energy of each state $|n,l,m>$ minus the energy of q Floquet sidebands, $q\hbar\omega$. The basis needs to include only a single m value because the symmetry under rotation about the z axis means that different m values are not mixed. Here, we consider only $m=0$ states. There are two types of off-diagonal terms. The first type results from a coupling due to the Stark effect. The matrix elements $z_{j,k}$ vanish unless the states differ by one unit of orbital angular momentum, $\Delta l = \pm 1$. The second type results from the oscillating field coupling states with $\Delta l = \pm 1$ and $\Delta q = \pm 1$.

Diagonalizing a set of $m=0$ states in a static electric field requires a basis size of $\sum_{n=1}^{N} n \approx N^2/2$, where N is the largest principal quantum number in the basis. The total basis size required to solve Eq. (3.18) is thus $(2q_{\max}+1)N^2/2$, where $q_{\max}$ is the number of Floquet sidebands included for each state. To estimate the number of states needed for a well converged computation, we use the approximation in Sec. 3.3 that the number of sidebands with significant strength is kF_1/ω where k is the slope of the steepest Stark state. Then $k \leq 3N^2/2$, so $q_{\max} \approx 3N^2F_1/2\omega$ and the required basis size is approximately $(1+3N^2F_1/\omega)N^2/2$. For $N=30$ with $F_1 = 1$ V/cm and $\nu = 300$ MHz, about $q_{\max} = 10$ sidebands are needed, implying a basis of about 5000 states. Matrices of this size can be diagonalized on a desktop computer.

Once the Floquet eigenstates are found, the transition strength from a ground state, say $|3s>$, to an excited state is easily calculated as follows. The inner product used in Eq. (3.17) is more generally defined as [Sam73]

$$<\psi_1|\psi_2> = \frac{1}{T}\int_0^T dt \int d\mathbf{r}\psi_2^*(\mathbf{r},t)\psi_1(\mathbf{r},t), \tag{3.19}$$

where T is the period of the oscillating field. The ground state is unperturbed by the relatively weak oscillating fields considered here, and therefore does not develop sidebands, implying a temporal dependence of $e^{i0\omega t}$. For lithium excited from $|3s>$,

the transition rate is proportional to

$$|<3s|z|\psi>|^2 = \left|\sum_{q,k} C_{q,k}\frac{1}{T}\int_0^T dt e^{i0\omega t}e^{iq\omega t}<3s|z|k>\right|^2 \quad (3.20)$$

$$= \left|\sum_k C_{q=0,k}z_{3s,k}\right|^2 . \quad (3.21)$$

We have two different methods for diagonalizing the matrix (3.18). The Givens-Householder method [Ort67, Coo61] diagonalizes the entire matrix, and can be used to find the eigenvectors needed to compute oscillator strengths. This method is seldom used because one rarely needs all the eigenvalues and eigenvectors, and it is time consuming to calculate them. The other method is the Lanczos method [Lan50, ER80] as implemented by Dominique Delande [DBG91]. This algorithm computes a band of eigenvalues and eigenvectors near some selected energy. See [Cou95] for more discussion about our implementation of these methods.

3.4.1 Numerical Results

To test this method we have applied it to the $n = 31$ Stark manifold in lithium. Because this manifold is used to calibrate the amplitude of the oscillating field (described in Sec. 4.8), it is important to thoroughly understand its behavior. Figure 3-1 shows the results of the diagonalization as a function of the amplitude of the oscillating field. The frequency is 580 MHz and the static field strength is 23.14 V/cm. (These are typical experimental values.) The state near the left of the figure is the $31s$ state, which is depressed to lower energy by the quantum defect. The simple method given in Sec. 3.3 can be used to compute the strength of the sidebands. To do this, the slope of the states in lithium, which can be computed by diagonalizing the Hamiltonian for lithium in a static field, are required. We do not do this in detail here, but simply note that the strengths of the sidebands are consistent with the slopes of the states. Because the middle states in the manifold have the smallest slopes, they are the least perturbed by the oscillating field. The extreme states exhibit sidebands with significant amplitude because they are the most highly sloped. Figure

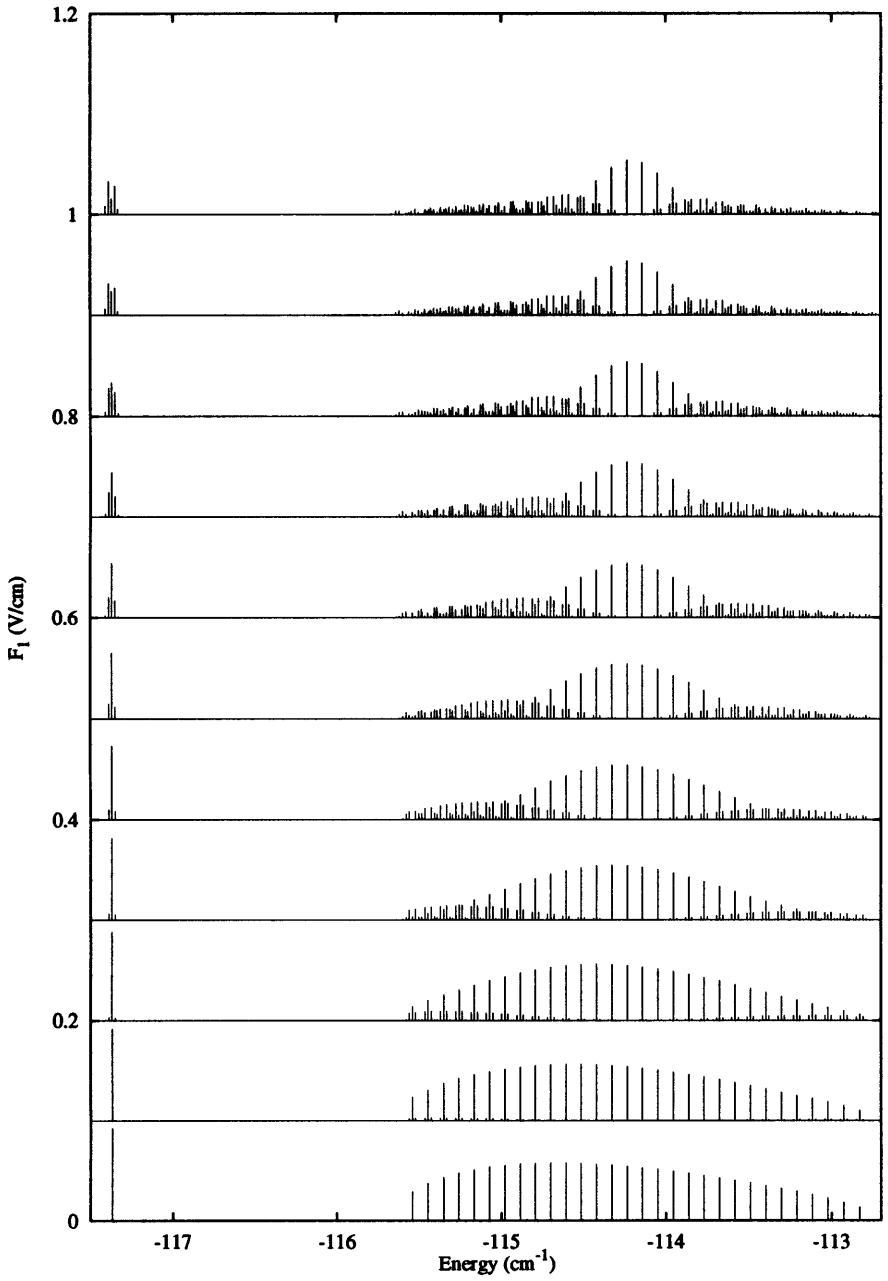

Figure 3-1: Computed spectra, lithium $n = 31$ Stark manifold. Ten sidebands on both sides of every state are used. The static field strength is $F = 23.14$ V/cm. The frequency of the applied field is 580 MHz.

4-14 compares a computation done for a frequency of 300 MHz, a static field strength of 23.6 V/cm, and an oscillating field amplitude of 0.44 V/cm with experimental spectra. The agreement with experiment indicates that the Floquet description and the numerical methods are consistent.

3.4.2 Stark Structure in a Perpendicular Oscillating Field

The method described in Sec. (3.4) is easily modified to calculate the effect of a perpendicular oscillating electric field with amplitude F_2 and angular frequency ω. For a field along the x axis, the term $F_1 z\cos(\omega t)$ in the Hamiltonian (3.14) is replaced with $F_1 x\cos(\omega t)$. In addition to the matrix elements $z_{j,k}$ that are generated by the static field F, there are additional matrix elements $x_{j,k} =< j|x|k >$ that are generated by the oscillating field. A derivation similar to that in Sec. (3.4) leads to a matrix equation reminiscent of Eq. (3.18):

$$\left(E_j - q\hbar\omega\right) C_{q,j} + \sum_k \left[F z_{j,k} C_{q,k} + \frac{F_1 x_{j,k}}{2}\left(C_{q-1,k} + C_{q+1,k}\right)\right] = \epsilon C_{q,j}. \qquad (3.22)$$

Equation (3.22) is harder to solve computationally than Eq. (3.18) because the perpendicular field breaks the cylindrical symmetry of the system. A much larger basis including all m states must be used. For each n included in the basis, n^2 states are required, rather than n. Results presented here will be for a static field strength small enough that there is no n mixing, so that a single n-manifold can be used and computations are feasible.

The simple and intuitive picture given in Sec. 3.3 changes because the Stark eigenstates of the time-independent system do not diagonalize a perturbing field $F_1\hat{\mathbf{x}}$ as they do a perturbing field $F_1\hat{\mathbf{z}}$. A field along the z axis produces a first-order shift in the energy because the Stark states have dipole moments along the z axis. A field along the x axis produces at most a second-order shift to the energy of a single Stark state. To compute the shift using perturbation theory is challenging. Instead, let us simply assume that we know the size of the second-order shift and examine its effect on Stark structure within the framework of Sec. 3.3.

With the supposition that the perpendicular oscillating field produces a second-order perturbation to an $m = 0$ state, $\Delta E = \frac{1}{2}kF_1^2\cos^2(\omega t)$, where k now represents the polarizability of the state, Eq. (3.8) becomes

$$\left[E + \frac{1}{2}kF_1^2\cos^2(\omega t)\right] T(t)|\psi(\mathbf{r})> = i\hbar\dot{T}(t)|\psi(\mathbf{r})> \tag{3.23}$$

This has a solution

$$T(t) = e^{-i\int[E+\frac{1}{2}kF_1^2\cos^2(\omega t')]dt'/\hbar} = e^{-i[(E+\frac{1}{4}kF_1^2)t/\hbar + \frac{kF_1^2}{8\hbar\omega}\sin(2\omega t)]}, \tag{3.24}$$

yielding a wave function

$$|\psi(\mathbf{r},t)> = |\psi(\mathbf{r})>e^{-i(E+\frac{1}{4}kF_1^2)t/\hbar}\sum_{n=-\infty}^{+\infty} J_n\left(\frac{kF_1^2}{8\hbar\omega}\right)e^{i2n\omega t}. \tag{3.25}$$

We arrive at the prediction that a second-order perturbation to the energy produces only even sidebands with amplitudes given by Bessel functions.

We now use the brute force approach of diagonalizing Eq. (3.22) to examine the $n = 10$ Stark manifold in hydrogen. A low n value allows a manageable calculation. We compare and contrast the effects of parallel and perpendicular fields with a frequency of 15 GHz in Fig. 3-2. It can be seen that a perpendicular field with amplitude 1000 V/cm produces sidebands of smaller amplitude than a parallel field with a much smaller amplitude of 100 V/cm. This is expected because the parallel field produces a first-order perturbation to each Stark state. A closer examination shows that the positions of the large states and their sidebands for the perpendicular case do not correspond to those for the parallel field. From comparison with the bottom spectra, it appears that some of the sidebands are spaced by twice the frequency of the oscillating field. For a deeper understanding, Figure 3-3 shows the spectral evolution as the oscillating field strength changes. The states display a nonlinear shift in energy as F_1 increases. The strength of the sidebands increases as F_1 increases. The nonlinear shift in the energy of the states is predicted using group-theoretical methods in [FY91]. Among the cases they consider is the adiabatic or low-frequency limit, in

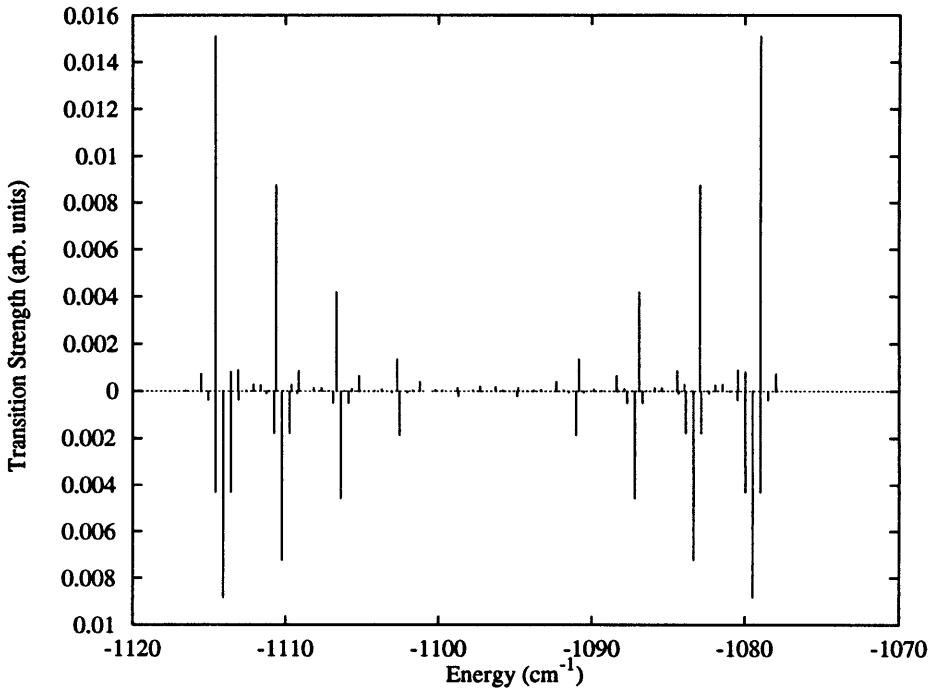

Figure 3-2: Computed spectrum, $n = 10$ Stark manifold, hydrogen. $\nu = 15$ GHz. Static field strength is 3000 V/cm, $q_{\max} = 6$. Top: perpendicular oscillating field, 1000 V/cm amplitude. Bottom: parallel oscillating field, 100 V/cm amplitude. The apparent discrepancies between the positions of the peaks in the top and bottom are explained in the text.

which ω is much less than the splitting between adjacent Stark states. They show that the energy of a state is given by the familiar formula for the linear Stark effect, $E = -\frac{1}{2n^2} + \frac{3}{2}nkF_0$. However, the electric field is replaced by the average *magnitude* of the electric field, which we call F_0. For our problem,

$$F_0 = \frac{1}{T}\int_0^T (F^2 + F_1^2)^{1/2} dt. \tag{3.26}$$

For F_1 along the z axis, $F_0 = F$. For F_1 perpendicular to F , Fursa *et al.* show that

$$F_0 = \frac{2}{\pi}\left(F^2 + F_1^2\right)^{1/2} I\left(\frac{F_1}{(F^2 + F_1^2)^{1/2}}\right), \tag{3.27}$$

where $I(x)$ is the whole elliptic integral of the second type. In the limit of a weak

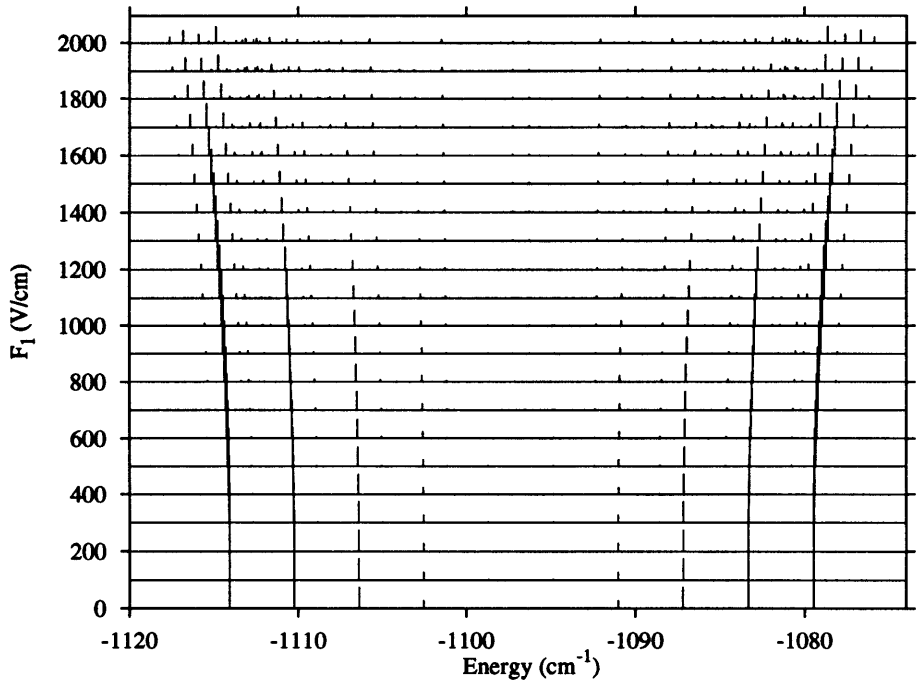

Figure 3-3: Computed spectra, $n = 10$ Stark manifold, hydrogen. $q_{\max} = 6$, $\nu = 15$ GHz. Static field strength is 3000 V/cm, oscillating field amplitude is between 0 and 2000 V/cm.

field, $F_1 \ll F$,

$$F_0 \approx \left(F^2 + F_1^2\right)^{1/2} \left(1 - \frac{F_1^2}{4(F^2 + F_1^2)}\right). \tag{3.28}$$

In the limit of a strong field, $F_1 \gg F$,

$$F_0 \approx \frac{2}{\pi} F_1. \tag{3.29}$$

The lines in Fig. 3-4 show Eq. (3.27) plotted for $m = 0$ and $m = 1$ energy levels. A close examination shows some discrepancy between the above result and the computations at large F_1. This may be the result of the breakdown of the adiabatic approximation. The $m = 0$ states exhibit sidebands with equal amplitudes separated by 30 GHz from the $m = 0$ states. This corresponds to a frequency 2ω. These positions agree with the prediction of Eq. (3.25). The $m = 1$ states develop sidebands at ω. These arise because the perpendicular field produces a *first*-order shift to an $m = 1$ state. Note that the amplitudes of the sidebands are unequal.

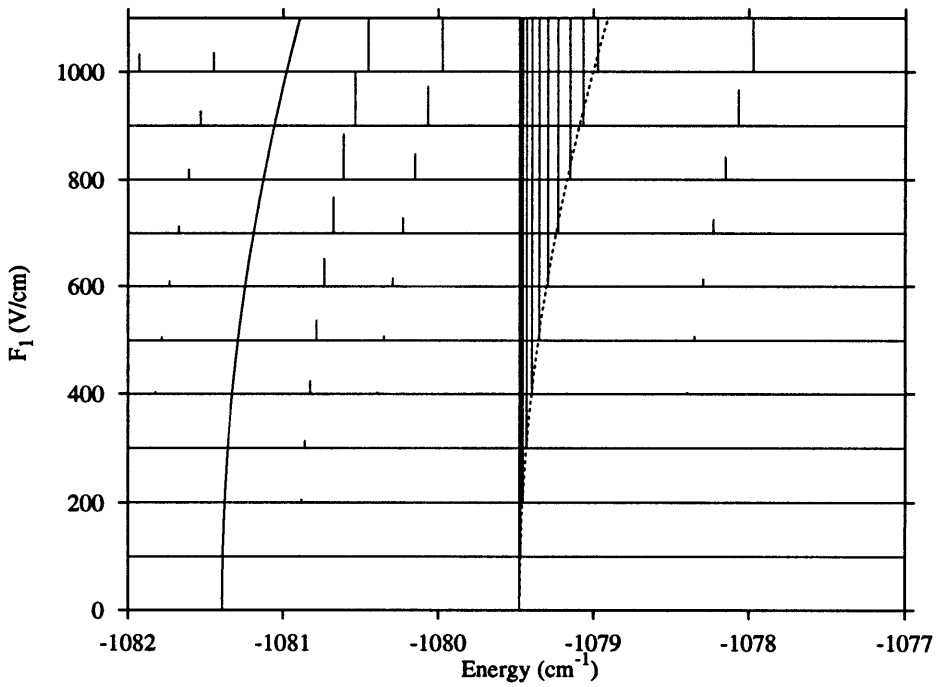

Figure 3-4: Enlargement of Fig. 3-3. The solid and dashed curved lines are generated from Eq. (3.27) for $m = 1$ and $m = 0$ states, respectively. The states to the left and right of the $m = 1$ state are spaced by $\hbar\omega$, while the states to the left and right of the $m = 0$ state are spaced by $2\hbar\omega$.

3.4.3 Recurrence Spectra in Oscillating Fields

To compare experiments or closed orbit theory with quantum theory, quantum spectra must be computed along a line of constant scaled energy. Recall, from Sec. 2.1, that along this line $E = \epsilon w^{-2}$, $\omega = \tilde{\omega} w^{-3}$, and $F_1 = \tilde{f} w^{-4}$, where $w = F^{-1/4}$. The Lanczos method is used to diagonalize the matrix (3.18) at many equally spaced steps in w. At each point, an energy offset given by the above scaling laws is sent to the routine, which returns several eigenvalues and transition strengths near the offset energy. The result is a set of transition strengths to each state at several energies near a line of constant scaled energy. These are interpolated with a cubic spline to give the transition strength for the desired scaled energy. The recurrence spectrum is the Fourier transform of the spectrum with respect to w. This method, applied to computing recurrence spectra in static electric and magnetic fields, is described in

[Cou95], where it is shown to produce accurate results for both hydrogen and lithium. This method is applied to hydrogen and lithium in oscillating fields at $\epsilon = -6$ and $\epsilon = -4$ in Sections 6.3 and 6.4, respectively.

Chapter 4

Experimental Method

This chapter describes the apparatus (see Fig. 4-1) used to perform high-resolution laser spectroscopy on Rydberg states of lithium in external static and oscillating electric fields. Lithium atoms traveling in an atomic beam are excited in a three-step laser-excitation scheme (Fig. 4-2). This excitation scheme, which differs from those used in previous experiments in this laboratory, is described in some detail. The laser radiation is produced with two argon-pumped dye lasers and an external-cavity diode laser. A static electric field parallel to the direction of the atomic beam is provided by a pair of field plates in the interaction region. An oscillating electric field parallel to the static field is applied by capacitively coupling rf radiation onto one of the field plates. A frequency synthesizer generates rf radiation with frequency between 200 MHz and 1260 MHz. The experiment detects ionizing and non-ionizing Rydberg states. Long-lived Rydberg states drift out of the interaction region into a detection region where they are field ionized and counted. Ions produced by rapidly ionizing states are accelerated from the interaction region by the static field and counted.

The wavelengths of two lasers are locked to the $2s \rightarrow 2p$ and $2p \rightarrow 3s$ transitions by monitoring resonance fluorescence from the atomic beam. The wavelength of the third laser, which is scanned to measure a spectrum, is determined absolutely with iodine absorption lines and a calibrated Fabry-Perot etalon. The static and oscillating field strengths are calibrated using the Rydberg atoms themselves. We perform recurrence spectroscopy by simultaneously varying the laser energy, the static and oscillating field

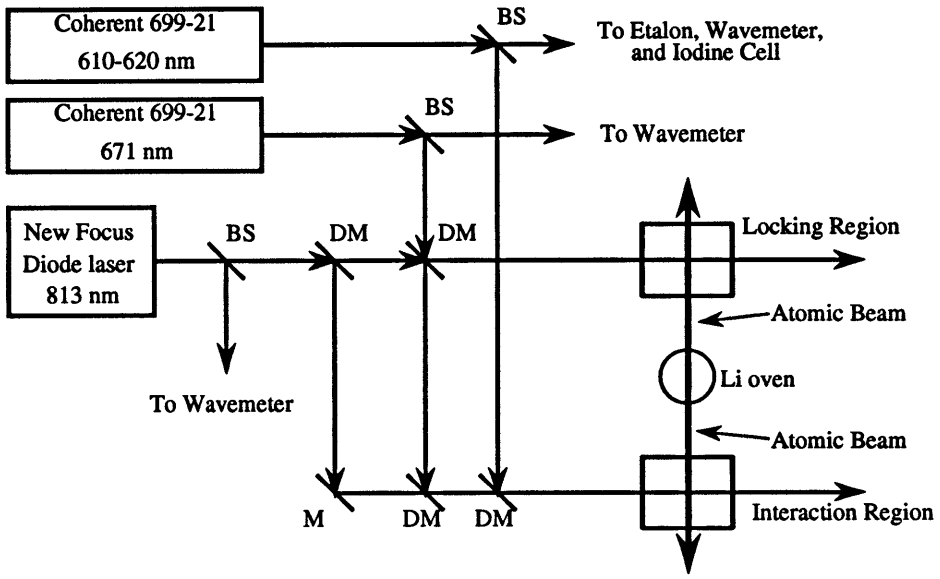

Figure 4-1: Overview of the experiment. The principal optical elements are beam splitters (BS), mirrors (M), and dichroic mirrors (DM). Three laser beams are generated with two dye lasers and a diode laser. Samples of each beam are sent to a Burleigh model WA-20 wavemeter. The wavelengths of the 671 nm and 813 nm beams are stabilized from fluorescence signals from the locking region. The wavelength of the yellow laser, which operates from 610-620 nm, is scanned to measure a spectrum. A sample of the beam is directed into a temperature-stabilized Fabry-Perot etalon and an iodine absorption cell for absolute wavelength calibration. The main portions of the beams are overlapped using dichroic mirrors. The combined beam is focused through a lens into the interaction region.

strengths, and the frequency of the oscillating field in a manner that maintains the classical scaling laws constant. The Fourier transform of such a spectrum reveals peaks at the actions of the closed classical orbits.

The experimental apparatus is the result of many years of work by many people. Various aspects of the experiment are described in depth in previous theses from this group [Kas88, Wel89, Iu91, Cou95, Jia96]. This chapter describes in detail the recent additions to the experiment and emphasizes a few other points of interest to the author.

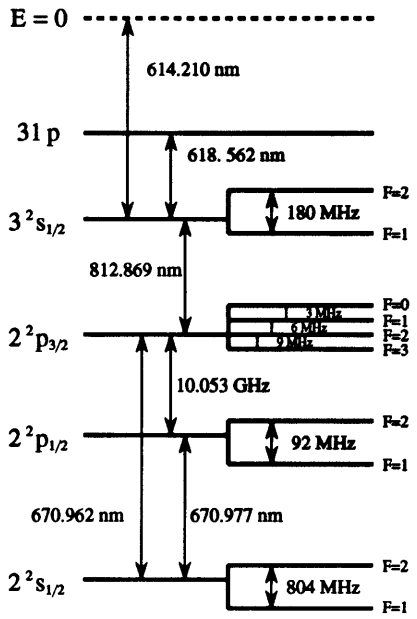

Figure 4-2: ^{7}Li level structure (not to scale). All wavelengths are in vacuum. The values are taken from [Kas88, Jia96]. Laser excitation proceeds from $2^2s_{1/2} \rightarrow 2^2p_{3/2} \rightarrow 3^2s_{1/2} \rightarrow np$. The $n = 31$ state is typically used for electric field calibration. The $2p$ and $3s$ state lifetimes are $\tau_{3s} = 26.3$ ns and $\tau_{3s} = 29.2$ ns, respectively.

4.1 Lasers

Lithium is excited from the ground state to Rydberg states with a newly-developed three-step laser excitation scheme. The previous method used two-photon excitation $2s \rightarrow 3s$ before the final excitation to the Rydberg state. The two photon excitation demands intense laser beams (≈ 100 kW/cm^2), whereas similar excitation rates can be achieved with single-photon resonant transitions driven with much weaker laser beams (≈ 1 mW/cm^2). In contrast with previous experiments in a magnetic field, the intermediate $2p$ state is unperturbed by the electric fields applied in these experiments. Consequently, it is straightforward to lock lasers to the intermediate $2s \rightarrow 2p$ and $2p \rightarrow 3s$ transitions. Development of this excitation scheme was begun by Hong Jiao, and some aspects of it are described in his thesis [Jia96]. This thesis presents the first experimental results obtained using this excitation process.

4.1.1 Red Laser

The $2s \rightarrow 2p$ transition (see Fig. 4-2) is excited using 671 nm light produced by a Coherent 699-21 ring dye laser. We drive the transition from the $2s_{1/2}$ $F = 2$ state to the unresolved hyperfine states of $2p_{3/2}$. DCM laser dye is pumped by about 6 Watts split from a Coherent Innova 100-10 argon ion laser. The laser is run in multi-line mode (488 nm and 514 nm) because this allows a lower current for the same power as in the single-line mode. The lower current reduces the demand for cooling water. The laser reliably produces 300 mW of power when the dye is new. Because this is much more power than is needed to drive the principal transition (typically a few miliwatts), the time between dye changes can be infrequent. The laser requires little maintenance and locks for many hours.

A sample of a few miliwatts is split from the main beam and directed into a Burleigh model WA-20 wavemeter and to a spectrum analyzer while the main beam is collimated, split, and directed into the interaction region and the locking region, described in Sec. 4.2.

4.1.2 Diode Laser

The $2p \rightarrow 3s$ transition is driven by 813 nm light from a New Focus model 6224 external-cavity diode laser. This laser delivers 18 mW of power single-mode and tunes over 70 GHz without mode hopping. The beam path is similar to that of the red laser beam. Samples are directed to the wavemeter and a spectrum analyzer while the main beam is collimated and directed into the locking and interaction regions. The laser excites the atoms into the $3s$ $F = 2$ hyperfine state.

Diode lasers have several advantages over dye lasers. They do not require an expensive pump laser, cooling water, or laser dyes, and they use readily available 120 VAC. There are some disadvantages, however. In contrast to the Coherent dye lasers which are actively locked to a temperature stabilized reference cavity, the diode laser cavity is passive. Stabilization is necessary for the dye laser because of the instability created by the dye jet. As a result, the dye laser is also stable against perturbations of

the environment—vibrations, changes in temperature, etc. The diode laser includes no active stabilization. Rather than stabilize the diode laser against a cavity, we chose to lock it to the atomic transition. The technique is described in Sec. 4.2.

The New Focus laser was a new model when we purchased it in 1995. As with many new products, it experienced some rough days in the beginning. After a short time, the laser could not scan more than about 1 GHz without mode hopping. The problem was due to a weak epoxy used to attach the laser diode. Over a period of weeks, the diode slowly slipped under gravity, until the cavity became completely misaligned and could not be tuned. The laser was designed so that nothing could be adjusted by the user without opening the cavity and voiding the warranty. It therefore made a trip back to its birthplace in California, where a stronger epoxy was installed. It has since given 1000 hours of use with no problems.

4.1.3 Yellow Laser

The final excitation to a Rydberg state uses light from another Coherent 699-21 dye laser using Kiton-Red laser dye. Operation of this laser remains the same as described in [Kas88]. The laser reliably produces 200 to 300 mW of power and scans 30 GHz without mode hopping. For the work in this thesis, the polarization is adjusted to excite $m = 0$ states.

4.2 Locking

Before the work reported here, the $3s$ state in lithium was populated by two-photon excitation on the $2s \rightarrow 3s$ transition using 735 nm light produced with a krypton-pumped dye laser. This laser was locked to the transition by monitoring fluorescence from either the $2p$ or $3s$ states at 671 nm or 813 nm, respectively. Because these wavelengths were far from the laser wavelength, filters could be used to remove scattered laser light, and low excitation rates could be measured. With the new excitation scheme, the fluorescence must be resolved above any background of scattered laser light because the scattered light has the same wavelength as the fluorescence. For

experiments in a magnetic field, where the excitation frequencies are magnetic field dependent, it was necessary to lock the lasers at the point of Rydberg excitation. Fortunately, for the electric field experiments, the $2s \rightarrow 2p \rightarrow 3s$ transition frequencies are field independent, and the lasers can be locked to the atomic beam at any point. This enabled the use of a separate locking region that could be designed to minimize the scattered light without compromising other design constraints of the interaction region.

The initial alignment of the three laser beams and the atomic beam in the interaction region would be extremely challenging if we could not monitor the fluorescence from the intermediate states. For this reason, provision is made to monitor that fluorescence in the interaction region. Once the initial alignment is successful, the final alignment is adjusted by maximizing the production of Rydberg atoms.

Figure 4-3 shows a diagram of the locking region. The mechanical design is simple. A six-way $2\frac{3}{4}$ inch ConFlat cross is used. The atomic beam enters along one axis, laser beams pass through a window on the second, and fluorescence is detected through windows on the third, the vertical axis. The fluorescence is imaged onto the detectors with lenses. The signal levels are large enough to employ a photodiode rather than photomultiplier detectors, although the ability to use photomultipliers is maintained with a light pipe emerging from the bottom of the locking region.

The locking region was originally placed between the oven and the interaction region. Unfortunately, the $2s \rightarrow 2p$ laser optically pumped the atoms into their upper hyperfine state, effectively suppressing the Rydberg signal. It was thus necessary to create the double atomic beam system described below.

The fluorescence was monitored with an EG&G model HUV-4000B photodiode. The output of a built-in low-noise amplifier was used to lock the lasers with the electronic methods described in [Kas88]. The 671 nm and 813 nm laser energies were modulated at different frequencies and the fluorescence from *both* transitions was monitored with the single photodiode. The resulting electronic signal contained components at both frequencies. The signals from the two transitions were individually extracted with lock-in amplifiers tuned to the appropriate modulation frequency.

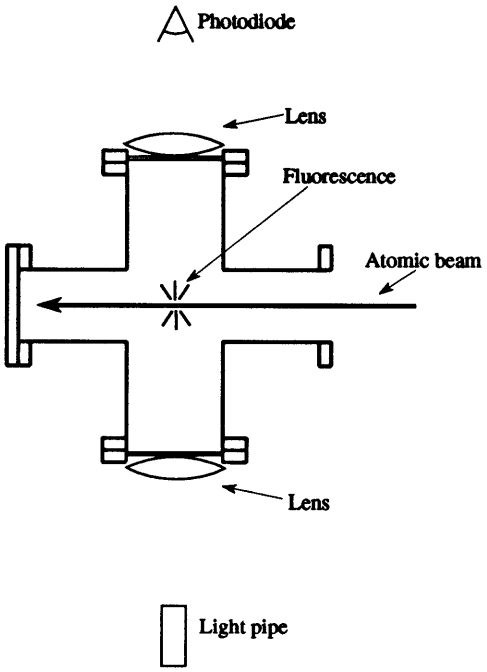

Figure 4-3: Schematic of locking region. The region is constructed from a 6-way, $2\frac{3}{4}$ inch ConFlat cross. 671 nm and 813 nm laser beams pass through windows in the plane of the page and intersect the atomic beam perpendicularly. Fluorescence is imaged onto detectors with lenses through vacuum windows at the top and bottom. The signal from the photodiode is sent to two lock-in amplifiers. The light pipe connects to a split fiber bundle from which the light is detected with two photomultiplier tubes.

4.3 Atomic Beam Source

The atomic beam source is described in the thesis of Michael Courtney [Cou95]. Lithium is stored in a reservoir in a stainless steel sleeve that holds several tube heaters. To provide the second beam for laser locking, this design was modified by machining a new stainless steel oven with apertures on both sides. The oven works as well as the single aperture model, but with half the life. The oven produces a strong flux, and runs reliably for many hours (we recharged it twice in the last year, a year that has seen much activity in the lab).

The oven has one peculiarity. As the lithium level drops, it is necessary to use higher and higher currents through the tube heaters to maintain the same lithium flux, up to 20% higher. However, a thermocouple on the oven reveals that the upper stainless steel part of the oven maintains the same temperature as the current is increased. A possible explanation for this behavior is that when the oven is full, the lithium acts as a conductive inner core which distributes heat to the upper part of the oven. As the lithium level drops, the upper stainless part becomes cooler, and hence it is necessary to heat the bottom more. This is plausible because the thermal conductivity of lithium is about five times greater than stainless steel. The explanation above supposes that the temperature of the lithium vapor is determined by the temperature of the walls of the oven, rather than the temperature of the liquid lithium. At a temperature of 700 °C, the density of lithium is 4.4×10^{15} cm^{-3} [Kas88], and the mean free path is $\lambda \approx 3$ mm. This means that a lithium atom undergoes many collisions as it travels within the oven, and therefore should be in equilibrium with the walls.

4.4 Stepwise Excitation Efficiency

Because the stepwise resonant excitation was new, we studied its behavior in some detail in order to be confident that we understood it. This section presents an experimental study of the excitation as a function of the power of the 671 nm and 813

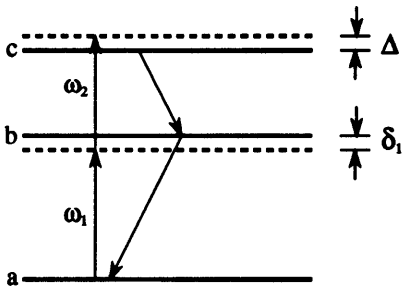

Figure 4-4: Three-level system. Laser beam with frequencies ω_1 and ω_2 drive transitions between levels a, b, and c.

nm lasers. This process can be understood using a density matrix. However, excitation to a Rydberg state involves four levels of the atom, each of which has hyperfine structure, so that the system is complex to model, even if the hyperfine structure is ignored.

Here, we take a simpler approach, treating the three-level $2s$-$2p$-$3s$ system to find the population of $3s$. This population can be probed experimentally by measuring the excitation rate into a Rydberg state. This is because the radiative lifetimes of Rydberg states are so long that they move from the laser excitation point and are detected before they can decay to the $2s$ or $3s$ levels.

We consider a three-level system with levels a, b, and c, as shown in Fig. 4-4. A laser beam with frequency ω_1 and electric field amplitude E_1 excites the atom from the ground state a to the intermediate state b. The second laser beam with frequency ω_2 and field amplitude E_2 completes the excitation to the upper state c. We define three detunings: $\delta_1 = \omega_b - \omega_a - \omega_1$, $\delta_2 = \omega_c - \omega_b - \omega_2$, and $\Delta = \omega_c - \omega_a - (\omega_1 + \omega_2) = \delta_1 + \delta_2$. Levels b and c decay radiatively with rates γ_b and γ_c, respectively. The Hamiltonian for the system is $H = H_0 - \mathbf{d}_{ab} \cdot \mathbf{E}_1(t) - \mathbf{d}_{bc} \cdot \mathbf{E}_2(t)$, where $\mathbf{d}_{ij}$ is the dipole moment between two levels i and j. The populations obey the density matrix equation of motion,

$$\dot{\rho} = \frac{1}{i\hbar}[H, \rho] - \begin{pmatrix} \gamma_c \rho_{cc} & (\frac{\gamma_b+\gamma_c}{2})\rho_{cb} & \frac{\gamma_c}{2}\rho_{ca} \\ (\frac{\gamma_b+\gamma_c}{2})\rho_{bc} & \gamma_b \rho_{bb} - \gamma_c \rho_{cc} & \frac{\gamma_b}{2}\rho_{ba} \\ \frac{\gamma_c}{2}\rho_{ac} & \frac{\gamma_b}{2}\rho_{ab} & -\gamma_b \rho_{bb} \end{pmatrix} . \tag{4.1}$$

The term on the right describes the decay of the excited states. The off-diagonal elements of this matrix are complex numbers. We express them as

$$\rho_{bc} = (x_{bc} + iy_{bc})e^{-i\omega_2 t} \tag{4.2}$$

$$\rho_{ac} = (x_{ac} + iy_{ac})e^{-i(\omega_1+\omega_2)t} \tag{4.3}$$

$$\rho_{ab} = (x_{ab} + iy_{ab})e^{-i\omega_1 t}, \tag{4.4}$$

where x and y are real. Substituting these into the equation of motion (4.1) leads to a set of nine equations. These are simplified by assuming a steady state solution, $\dot{\rho} = 0$. Introducing the notation $\overline{\gamma}_{bc} = \frac{1}{2}(\gamma_b + \gamma_c)$, we arrive at a 9×9 matrix equation:

$$\begin{pmatrix} -\gamma_c & 0 & 0 & 0 & 0 & 0 & 0 & 0 & 2d_2 \\ d_2 & -d_2 & 0 & 0 & 0 & d_1 & 0 & -\delta_2 & \overline{\gamma}_{bc} \\ 0 & 0 & 0 & 0 & 0 & 0 & d_1 & -\overline{\gamma}_{bc} & -\delta_2 \\ 0 & 0 & 0 & -d_2 & 0 & -\Delta & \frac{1}{2}\gamma_c & d_1 & 0 \\ 0 & 0 & 0 & 0 & -d_2 & -\frac{1}{2}\gamma_c & -\Delta & 0 & d_1 \\ 0 & d_1 & -d_1 & -\delta_1 & \frac{1}{2}\gamma_b & -d_2 & 0 & 0 & 0 \\ 0 & 0 & 0 & -\frac{1}{2}\gamma_b & -\delta_1 & 0 & -d_2 & 0 & 0 \\ -\gamma_c & \gamma_b & 0 & 0 & -2d_1 & 0 & 0 & 0 & d_2 \\ 1 & 1 & 1 & 0 & 0 & 0 & 0 & 0 & 0 \end{pmatrix} \begin{pmatrix} \rho_{cc} \\ \rho_{bb} \\ \rho_{aa} \\ x_{ab} \\ y_{ab} \\ x_{ac} \\ y_{ac} \\ x_{bc} \\ y_{bc} \end{pmatrix} = \begin{pmatrix} 0 \\ 0 \\ 0 \\ 0 \\ 0 \\ 0 \\ 0 \\ 0 \\ 1 \end{pmatrix} \tag{4.5}$$

This equation can be solved numerically using standard routines such as Gauss-Jordan elimination [PTVF92]. For lithium, $\gamma_c = \gamma_{3s} = 3.3 \times 10^7$ s^{-1} and $\gamma_b = \gamma_{2p} = 3.7 \times 10^7$ s^{-1}. Because the excitation here is assumed to be resonant, $\Delta = \delta_1 = \delta_2 = 0$. Figure 4-5 shows the result of solving the above matrix equation. The population saturates at laser intensities $I_{2p} \approx 6$ mW/cm^2 and $I_{3s} \approx 9$ mW/cm^2, in agreement with the saturation intensities found from the lifetimes of the states. For low 671 nm laser intensity, as the 813 nm laser intensity is increased beyond the saturation intensity, the population decreases because of power broadening. For higher 671 nm laser intensity, the population increases monotonically versus 813 nm laser intensity.

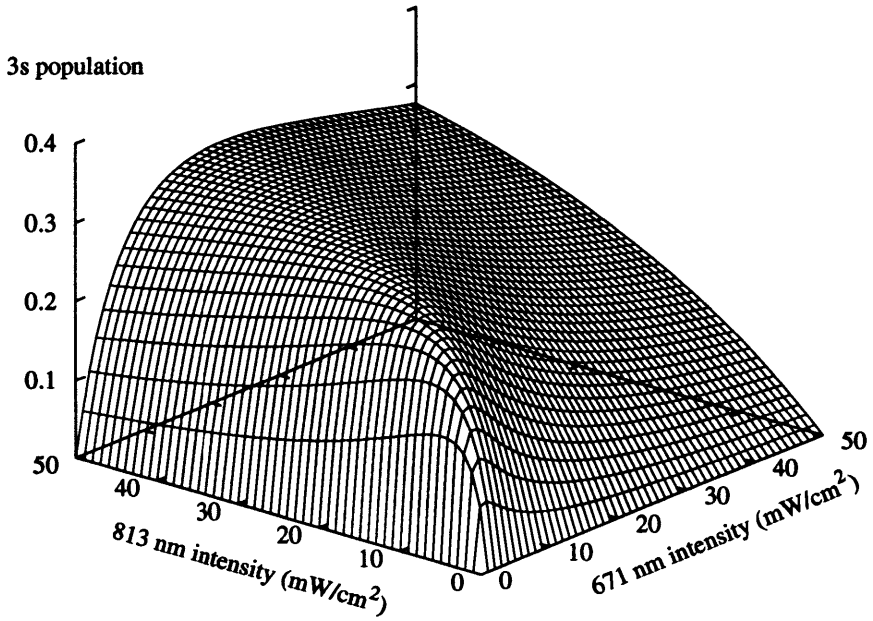

Figure 4-5: Computed 3s population, ρ_{cc}, found by diagonalizing Eq. (4.5). The 670 nm light drives the $2s \rightarrow 2p$ transition, and the 813 nm light drives the $2p \rightarrow 3s$ transition.

This occurs because a high 671 nm intensity means that any atom that decays from $3s$ is quickly driven to the ground state, so two photons are required to return it to the $3s$ level. Thus the excitation saturates at higher 813 nm intensity. When both lasers are intense, the population nears 1/3. In this case, transitions are driven between all levels, and they become equally populated.

To test this result and confirm that we understand the excitation process, we probed the $3s$ population by tuning the yellow laser to excite atoms into the continuum and measured the excitation rate. Variable attenuators were placed in the 671 nm and 813 nm beam paths to adjust the beam powers, which were measured using a UDT-Sensors model 10DP photodiode. The diode has a known linear relationship between incident light power and current. The photoionization signal was measured simultaneously with the current as the incident laser beams were attenuated.

Figure 4-6 shows the measured population and a fit to Eq. (4.5). Each point in the figure is a measurement of the population. The scatter of points arises from counting statistics. There are more points for some powers because the beam powers were not

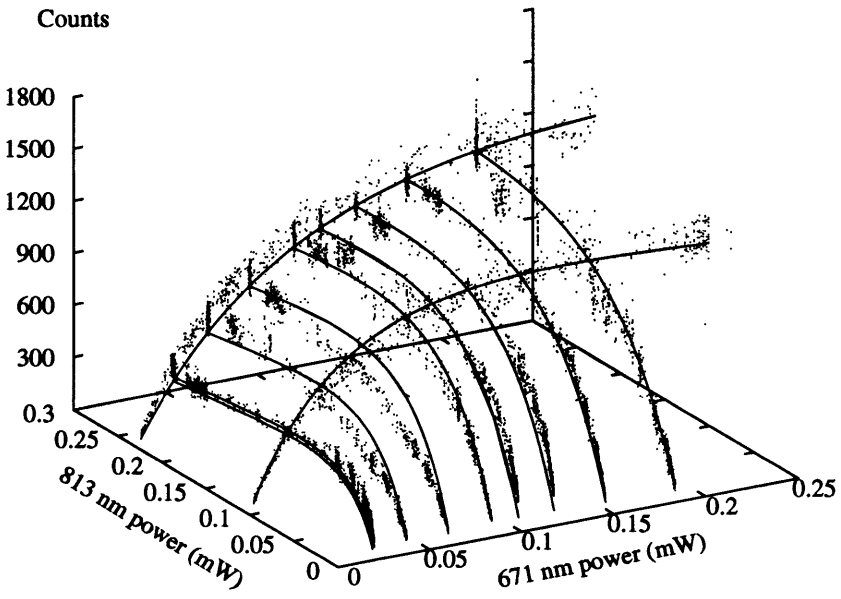

Figure 4-6: Experimental measurement of relative $3s$ population. The dots are Rydberg atom counts and the lines are a fit to Eq. (4.5).

adjusted linearly in some regions. The fit has three free parameters: an overall scaling that relates the Rydberg signal to the $3s$ population, and two factors that relate the measured laser powers to the beam intensities. These last two numbers give effective beam radii. The data give $R_{\text{eff}}(671\text{ nm}) = 0.90$ mm and $R_{\text{eff}}(813\text{ nm}) = 0.65$ mm. These agree with a rough measurement of the beam sizes and are consistent with the optical design, which uses a 671 nm beam radius that is about two times larger than the 813 nm beam.

We have learned from this study that we can accurately model the excitation process, and therefore we probably understand it and can control it. Note in particular that we have sufficient power to saturate the transitions, which lets us maximize the excitation efficiency.

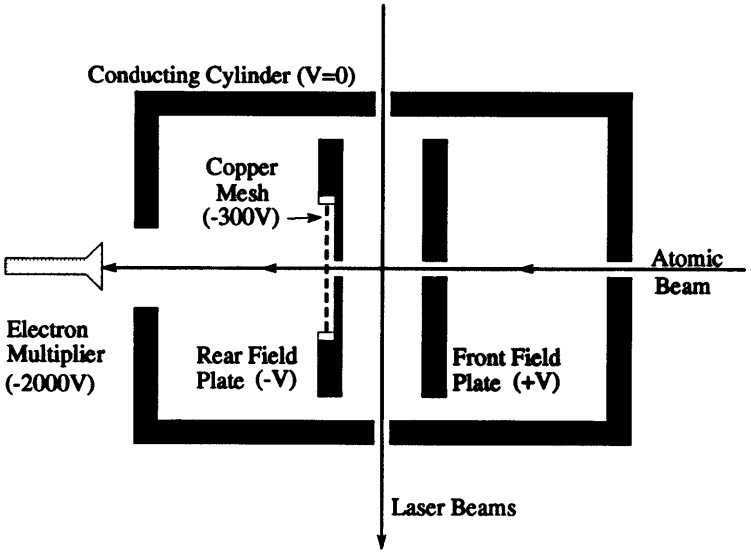

Figure 4-7: Schematic of the interaction region. Laser beams cross the lithium atomic beam perpendicularly. Symmetrically biased aluminum field plates spaced by 3/4 inch apply a static electric field parallel to the atomic beam direction. The plates are coated with Acheson Aerodag G graphite spray to reduce stray electric fields. The rf field with 200 MHz $\leq \nu \leq$ 1260 MHz is capacitively coupled onto the negative field plate (see Fig. 4-11). A copper mesh biased at -300 V provides a field to ionize Rydberg atoms that emerge from the interaction region.

4.5 Interaction Region

The interaction region (Fig. 4-7) is similar to that described in [Cou95]. Field-ionization signal is measured with a Detector Technology model 210-8 electron multiplier, which is biased negatively to detect positive ions. This provides a zero noise background, in contrast to electron detection. The electron multiplier is located on the atomic beam axis. The detector was originally placed off axis to avoid the atomic beam, but there was little high-n and continuum signal. It was discovered that the signal was much larger with the detector on axis. Surprisingly, the atomic beam creates no noise on the detector, and has not damaged it in two years of use. A Modern Instrumentation Technology model F-100T preamplifier-discriminator converts the signal to TTL pulses, which are counted by a data-acquisition board in a computer.

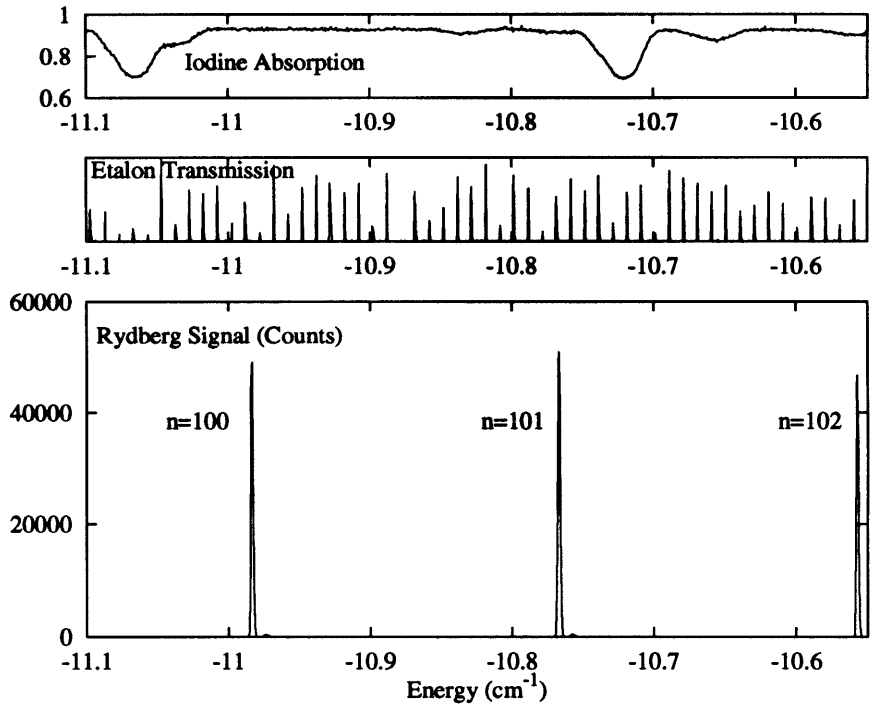

Figure 4-8: Experimental spectrum near $n = 100$. The top window is the iodine absorption spectrum, the middle window is the 300 MHz etalon transmission, and the bottom window is the Rydberg signal. The scan speed is 23 ms/point. A field of about 45 mV/cm has been applied to cancel a stray electric field parallel to the atomic beam axis.

4.6 Excitation of Rydberg States

Figure 4-8 shows an experimental spectrum recorded near $n = 100$. The transmission of the 300 MHz etalon used to linearize the scan is shown in the middle window of the figure. The top window shows the absorption of a sample of the yellow laser beam directed into an iodine absorption cell. The energies of catalogued iodine lines [GL78] provide an absolute calibration of the laser wavelength and Rydberg state energy.

The scan rate in Fig. 4-8 was 23 ms/point, implying a resonant excitation rate into $n = 100$ of 2.5×10^6 Rydberg atoms per second. Attenuation of the yellow laser beam shows that the signal remains linear even at these high count rates. Stronger signal levels are found at lower n states, consistent with the expected $1/n^3$ dependence of oscillator strength [BS57]. Indeed, levels near $n = 20$ strongly saturate the detector.

As we move to higher n (Figs. 4-9 and 4-10), several effects become important.

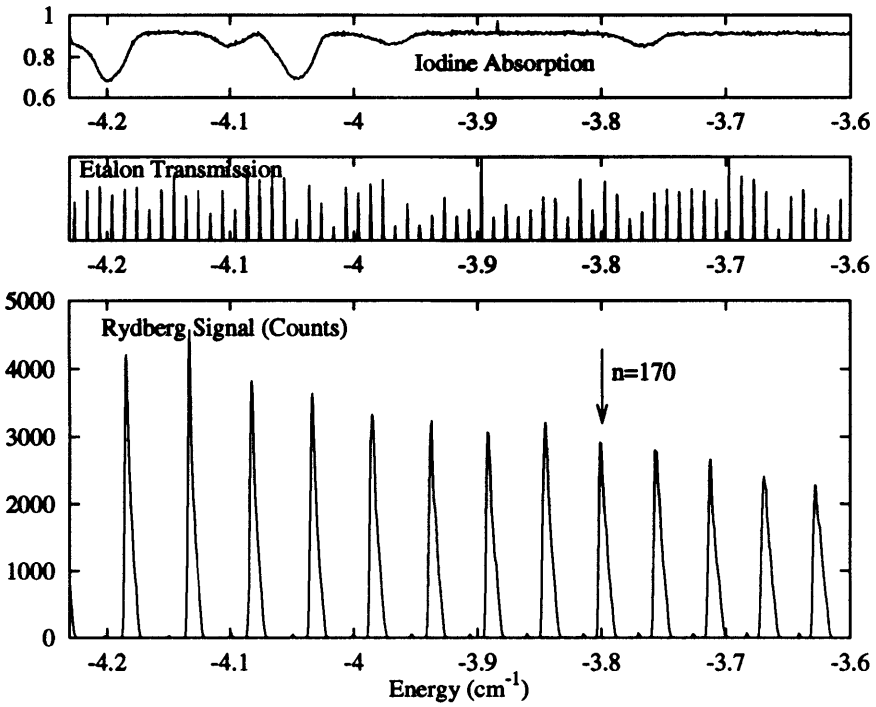

Figure 4-9: Same as Fig. 4-8, but at higher energy. The arrow labels the $n = 170$ Rydberg state.

The signal level drops as $1/n^3$. The density of states increases as n^3, so the states eventually merge into a continuum as the energy increases. High n states become visibly broadened into unresolved Stark manifolds due to residual stray electric fields. The size of this broadening is related to the electric field strength by [Kas88]

$$\Delta E \approx 3n^2F = (3.84\ \text{MHz/V/cm})\ n^2F, \tag{4.6}$$

where the last relation is in laboratory units. This broadening by a residual stray field is visible in Fig. 4-10.

With the field plates grounded, there is usually a stray electric field of 30 to 60 mV/cm. The field is nearly anti-parallel to the atomic beam, pointing toward the oven. The source of the field is believed to be lithium that has accumulated on the detector-side field plate. The strongest evidence for this is that the stray field slowly increases during a run. Furthermore, its size is related to the diameter of the atomic beam and to the quality of the beam collimation. Because the stray field is anti-

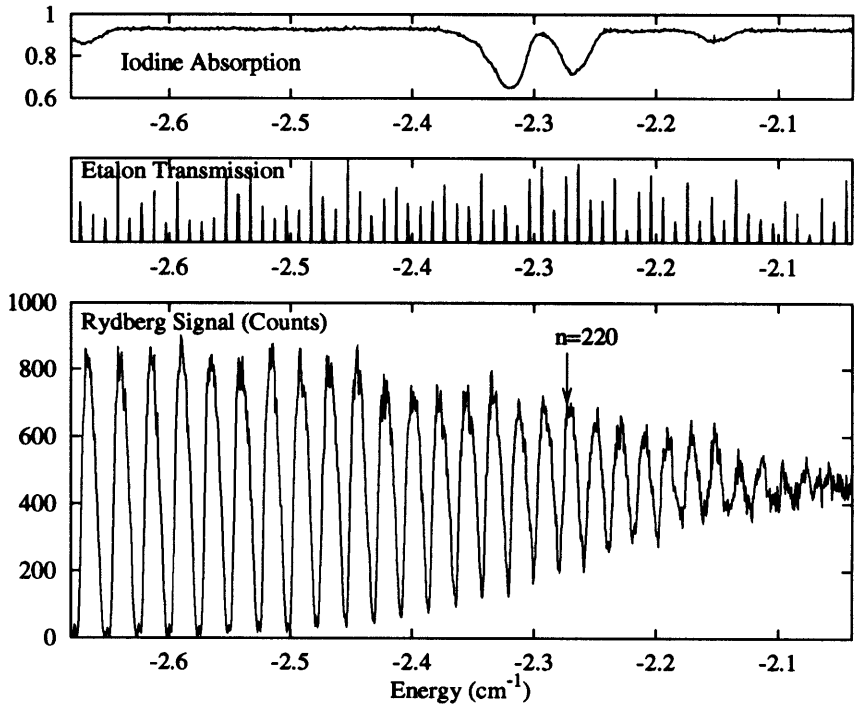

Figure 4-10: Same as Fig. 4-8, but at higher energy. The arrow labels the $n = 220$ Rydberg state.

parallel to the static field, it can be almost entirely cancelled with an offset in the static field strength. For example, the residual broadening of the states in Fig. 4-10 suggests a stray field of less than 4 mV/cm. During an experimental run, the stray field is monitored by examining the Stark broadening of states near $n = 100$ and the offset of the static field is adjusted. Consequently, the electric field uncertainty is maintained to less than 10 mV/cm in a typical run. This is adequate for our recurrence spectroscopy.

4.7 RF System

Recurrence spectroscopy in an oscillating electric field demands an rf system that provides a level output over a large bandwidth. (The field we refer to as "rf" lies near the microwave region.) This is challenging to achieve for several reasons. The need for static field plates constrains the geometry of the interaction region and creates cavity-like resonances in the system. These resonances will be present in any similar

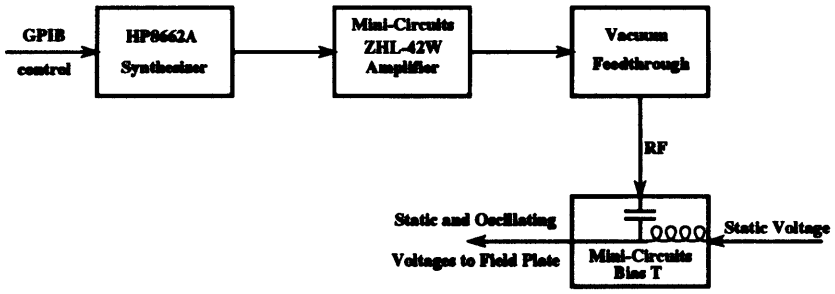

Figure 4-11: Schematic of rf system. RF with $\nu < 1260$ MHz is generated by a computer-controlled HP8662A synthesizer. The signal is fed to an amplifier for +30 dB of gain and then through a BNC vacuum feedthrough. The signal is combined with a static voltage in a Mini-Circuits model ZFBT-4R2G bias tee, from which the combined signal travel overs a short wire connected to the detector-side field plate.

broadband system, resulting in an unmatched load for many frequencies. The capacitive loading of the field plates rules out any simple scheme for impedance matching. Rather than attempt to impedance match, a different method was implemented in which rf was merely capacitively coupled onto a field plate. The transfer function for the rf field amplitude was measured using rf sidebands created on Stark states, as described in the next section. The transfer function was then used to remove fluctuations in amplitude by continuously adjusting the amplitude of the rf source as the frequency was swept.

Figure 4-11 is a schematic of the elements used to generate and apply the oscillating field. The rf source is a Hewlett Packard HP8662A frequency synthesizer. This is an extraordinary device: the resolution in frequency is 0.2 Hz, and the amplitude is controllable with a relative resolution of 0.1 dBm. Furthermore, the frequency and amplitude are scannable via a GPIB interface. The output is fed into a Mini-Circuits model ZHL-42W amplifier for +30 dB of gain. This amplifier works between 10 MHz and 4200 MHz and provides up to 30 dBm output power. The signal is directed through a double-ended BNC feedthrough. To apply a field that is parallel to the static field, we capacitively couple the rf directly onto the detector-side field plate through a Mini-Circuits model ZFBT-4R2G bias tee. This device has a bandwidth that extends from 10 MHz to 4200 MHz.

While it is straightforward to examine the effect of a field parallel to the static field, it would be challenging to study the effect of a perpendicular field. The application of a uniform perpendicular field requires metal surfaces parallel to the static field, which would degrade its uniformity. A further problem is introduced by the physics of Rydberg atoms in oscillating fields. As described in Sec. 3.4.2, a perpendicular field produces a much smaller perturbation to the system than a parallel field because it is only a second-order effect. Therefore, any method for applying a perpendicular field must produce almost no component in the parallel direction. For these reasons, this study is limited to the parallel field direction.

4.8 RF Field Amplitude Calibration

Accurate recurrence spectroscopy demands accurate knowledge of the oscillating field amplitude. This amplitude is determined using the Rydberg states themselves to produce a calibration (transfer function) of rf amplitude versus frequency.

Section 3.3 described the effect of an rf field on a state in a Stark manifold. The oscillating field generates sidebands on each state in the manifold, spaced by the frequency of the rf. A measurement of the amplitude of these sidebands can be inverted to yield the amplitude of the rf field, according to Eq. (3.12). There is some flexibility in choosing the static field strength. The best value is one large enough that sidebands from neighboring Stark levels do not interfere but small enough that neighboring n-manifolds do not cross. Additionally, the calibration requires an accurate relative measurement of oscillator strength, and therefore it is desirable to work at low n, where signal levels are high. We generally use the high-lying and low-lying Stark states, which have the greatest slopes and therefore the largest side bands. A region of the $n = 31$ Stark manifold, shown in Fig. 4-12, proved to be a good place for satisfying these constraints.

The $q = \pm 1$ sideband is the only sideband that has significant strength over the range of field amplitudes and frequencies accessible with this apparatus. The ratio of the strength of the first side band $q = 1$ to the central Stark state $q = 0$ is, from

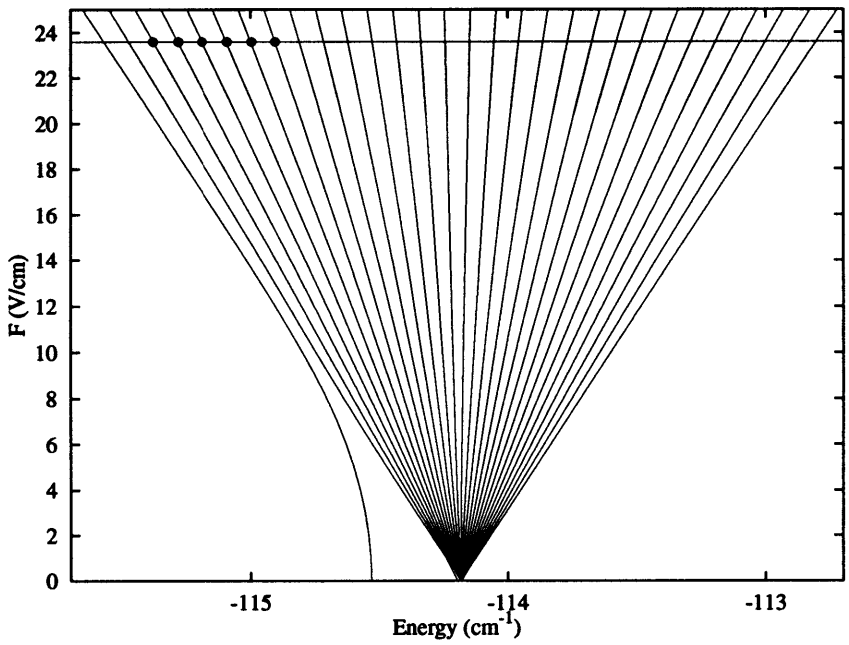

Figure 4-12: Computed energy levels, lithium $n = 31$, $m = 0$ Stark manifold. The solid horizontal line marks the value of F used for the measurement in Fig. 4-14. The solid dots mark the states with $(n_1 - n_2)$ between 24 and 14 labeled in Fig. 4-14. The energy of the left-most state is depressed by the p-state quantum defect. The energy of the s state is depressed even more by the larger s-state quantum defect, and is not visible in this figure.

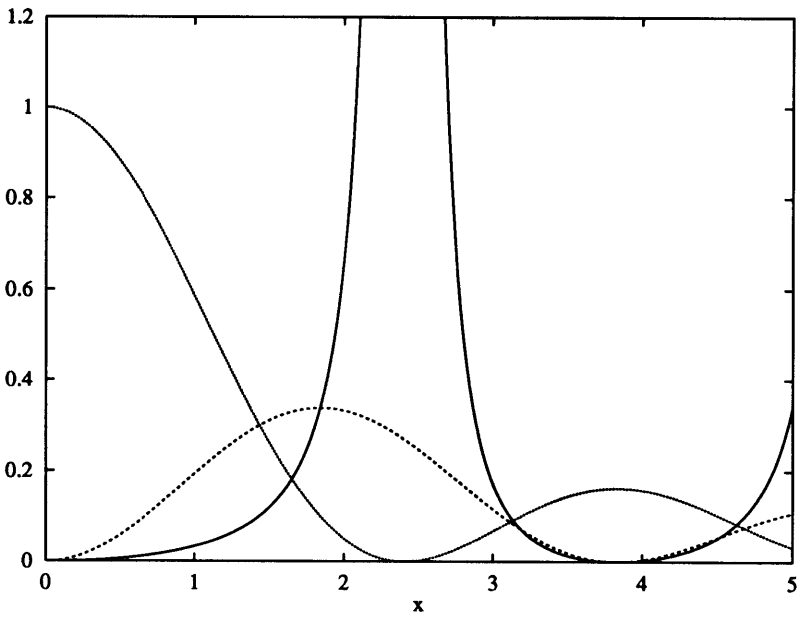

Figure 4-13: Dependence of rf sideband amplitude vs. $x = kF_1/\hbar\omega$. Solid line is $f/10$, defined by Eq. (4.7). Fine dashed line is $J_0^2(x)$, coarse dashed line is $J_1^2(x)$.

Eq. (3.12),

$$f = \frac{J_1^2(kF_1/\hbar\omega)}{J_0^2(kF_1/\hbar\omega)} \tag{4.7}$$

By measuring f and inverting Eq. (4.7), F_1 is found. The frequency ω is known, and the slope k, which equals $\frac{3}{2}n(n_1 - n_2)$ for hydrogen, is found for lithium with quantum computations done in a static electric field,

Figure 4-13 shows a plot of f, $J_0^2(x)$, and $J_1^2(x)$ as a function of $x = kF_1/\hbar\omega$. As F_1 increases, the $q = 0$ state loses strength, until it reaches zero at the first zero of $J_0(x)$. We generally work in the regime $x < 1.5$ because of limitations in the strength of the rf source and because at larger values the central state becomes so small that it is difficult to get good statistics in the measurement of the amplitude.

The field is calibrated at each rf frequency by scanning the laser over five or six Stark states, measuring f for each state, and inverting Eq. (4.7) to find F_1. The rf field amplitudes found for each state are combined to yield an average value and a standard deviation.

Figure 4-14 shows an experimental spectrum of the region of the $n = 31$ Stark

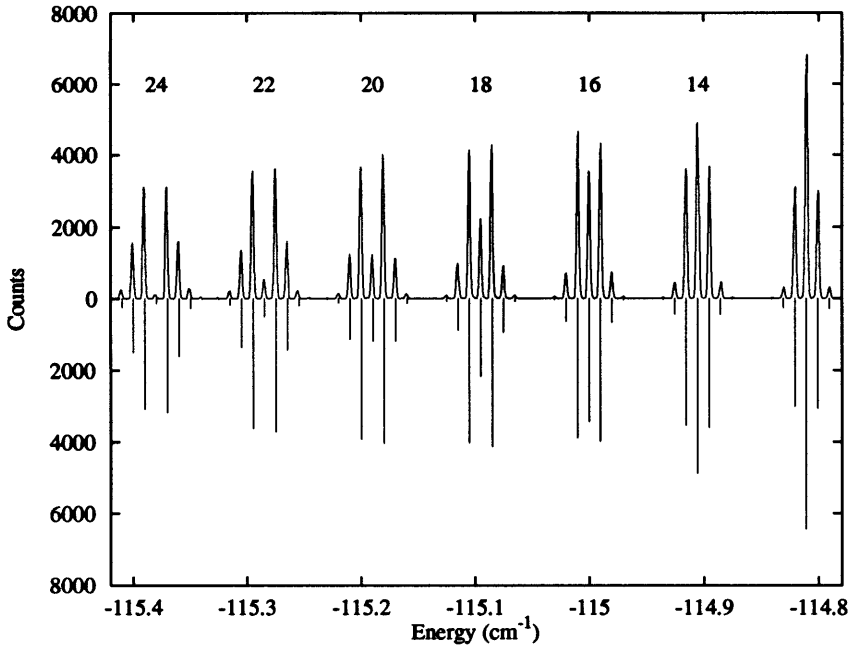

Figure 4-14: Comparison between quantum Floquet computation and experiment. The vertical axis is experimental counts. The upper plot is an experimental measurement of part of the $n = 31$ Stark manifold in a static plus rf field. The static field strength is $F = 23.6$ V/cm and the frequency of the applied field is 300 MHz. The lower plot is a diagonalization of Eq. (3.18) for an oscillating field amplitude of 0.44 V/cm. Its overall normalization is scaled for best agreement.

manifold marked in Fig. 4-12 with a 300 MHz applied rf field. The static field strength is 23.6 V/cm. The states at the left of the figure are the lower energy (red) Stark states. The field amplitude and frequency are such that several side bands are visible. Table 4.1 summarizes the extraction of the field amplitude from the spectrum. Each of the six states used to compute the amplitude gives a value consistent with the others. Averaging yields $F = 0.440 \pm 0.007$ V/cm. This 2% accuracy is typical.

The bottom spectrum in Fig. 4-14 is the result of diagonalizing Eq. (3.18) for a field amplitude equal to that found in the calibration, 0.44 V/cm. The agreement between the experiment and computed spectra demonstrates the validity of the Floquet computation.

Figure 4-15 shows the results of the calibration over a frequency range extending from 200 MHz to 1260 MHz. The amplitude varies significantly as a consequence of

state $(n_1 - n_2)$	k (MHz/V/cm)	f	$\sqrt{f}$	F_1 (V/cm)
24	1.494×10^3	24.05	4.9	0.441
22	1.372×10^3	6.876	2.622	0.439
20	1.251×10^3	3.486	1.867	0.443
18	1.133×10^3	1.965	1.402	0.444
16	1.013×10^3	1.171	1.082	0.443
14	8.935×10^2	0.665	0.815	0.428

Table 4.1: Summary of the measurement of the rf field amplitude at 300 MHz. The slopes k are found from quantum-mechanical diagonalization calculations for Li at $F = 23$ V/cm (Fig. 4-12). These differ slightly from the value found assuming a linear Stark effect in hydrogen, $k = 1.920n(n_1 - n_2)$ MHz/V/cm. The calibration yields $< F_1 >= 0.440 \pm 0.007$ V/cm.

the wild mismatch between the field-plate structure and the rf source. However, the calibration is reproducible and constant over time. An individual point is calibrated to a few percent, while between the calibration points the amplitude can be interpolated with a cubic spline, yielding an amplitude accurate to at least 10%. This is adequate for our recurrence spectroscopy.

Because F_1 must be adjusted as a spectrum is measured, it is necessary to know how F_1 changes as the power level of the HP8662A changes. The synthesizer has a resolution of 0.1 dBm and an absolute accuracy of 1 dBm. The absolute accuracy does not matter; the relative accuracy does. It is straightforward to compute the power level necessary to achieve a given amplitude if the entire rf system is linear. The primary source of nonlinearity is the amplifier, which provides a gain of +30 dB with a maximum output of +30 dBm. As the input power approaches this maximum, the gain saturates. Figure 4-16 displays the results of measurements of rf field amplitude at two frequencies as the power output is varied. The output power can be written as $P = \gamma F_1^2$, where γ is a constant proportional to the inverse of the effective impedance of the field plate structure. The power in dBm is

$$P_{\mathrm{dBm}} = 10 \log_{10} (P/1\mathrm{mW}) = \mathrm{constant} + 20 \log_{10} F_1. \tag{4.8}$$

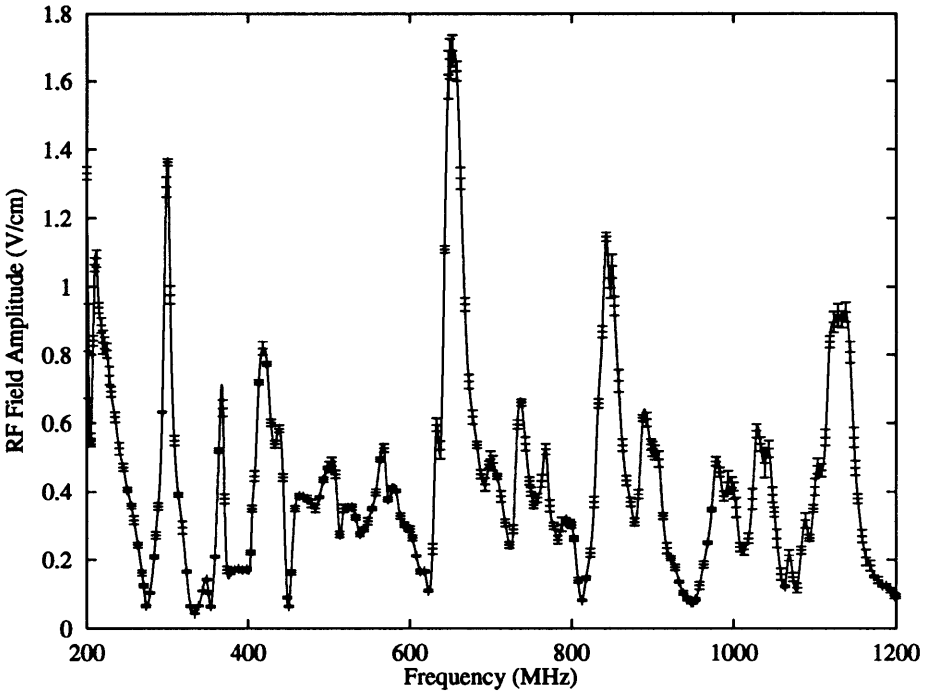

Figure 4-15: Results of calibration of rf field amplitude. The error bars show the standard deviation in the measurement of F_1. The solid line is a cubic-spline interpolation of the data. These values correspond to the field amplitude when the HP8662A is set at -10 dBm.

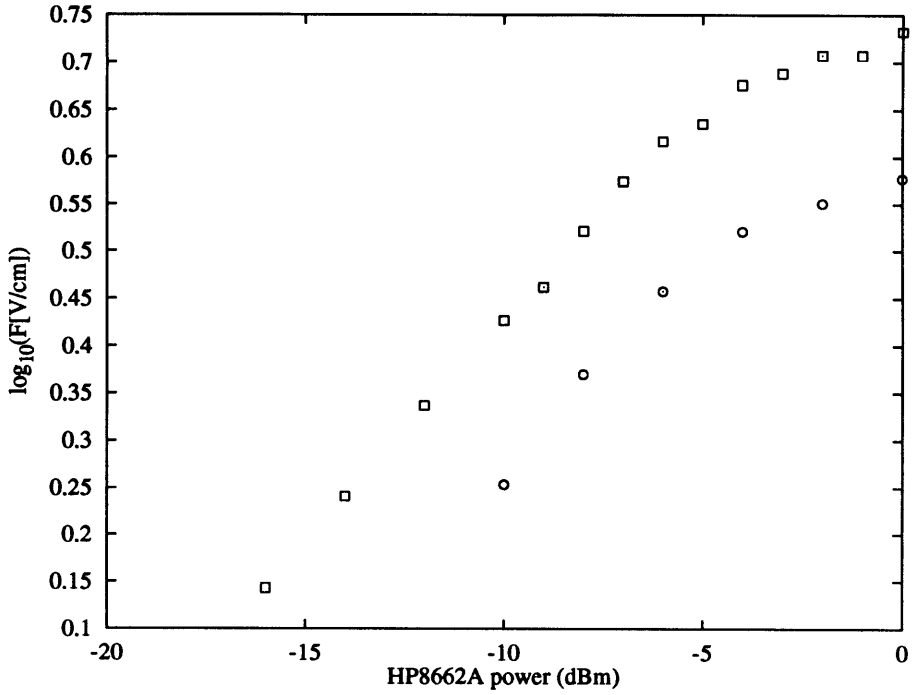

Figure 4-16: Calibrated rf field amplitude vs. input power level. Squares: 900 MHz; circles: 1200 MHz.

Therefore, we expect a linear relationship between the output power of the HP8662A measured in dBm and $\log_{10} F$. Holding a ruler to the linear part of Fig. 4-16 indeed reveals a slope of $1/20 = 0.05$. The gain becomes nonlinear near -6 dBm. While a correction for this nonlinearity could be included, we have chosen instead to work below this level. This regime provides field amplitudes that are adequate for the experiments.

4.8.1 Error Analysis

Here, we examine the accuracy and precision with which the synthesizer can set the rf field amplitude. Assume that the field amplitude is given by $F_1 = \alpha V$, where V is the voltage amplitude of the rf. The power in dBm is

$$P_{\mathrm{dBm}} = 10 \log_{10} \left(\frac{P}{1\mathrm{mW}} \right) = 20 \log_{10} \left(\frac{V}{V_0} \right) = 20 \log_{10} \left(\frac{F_1}{\alpha V_0} \right) \tag{4.9}$$

where $V_0^2 = 50\Omega \times 1\text{mW}$. The uncertainty in F_1 is

$$\frac{\delta F_1}{F_1} = \frac{\ln 10}{20}\delta P_{\text{dBm}} \tag{4.10}$$

The HP8662A has a relative uncertainty of $\delta P_{\text{dBm}} = 0.1$ dBm, so

$$\frac{\delta F_1}{F_1} = \frac{2.3}{20}0.1 = 0.011. \tag{4.11}$$

This 1% uncertainty is a little better than the accuracy of the calibration.

4.9 Static Field Calibration

Accurate recurrence spectroscopy also demands an accurate calibration of the static field strength. This is again best done using the Rydberg atoms themselves. Our method is to make a number of measurements of some of the states in the $n = 31$ Stark manifold, shown in Fig. 4-17, as the voltage applied to the field plates is changed. Comparison with computed energy levels for lithium gives the field strength at each voltage. A least squares fit yields the field to voltage ratio, F/V, and an offset due to the stray field along the beam direction. As expected, the relationship is linear, as demonstrated in Fig. 4-18.

The voltage is generated starting with two 12 bit D/A boards in the data acquisition computer. These are directed into a summing amplifier. One of the inputs serves as a DC offset, while the other channel is scanned by the computer as a recurrence spectrum is recorded. The data acquisition program automatically measures the offset voltage and adjusts it as needed. The scanned channel is typically reduced, not amplified, in the summing amplifier to give sufficient resolution. A 0 to 4095 control changes the output of the D/A from 0 to 5 V, giving a step size of about 1 mV. This is often too large a step, and so this channel is reduced in magnitude by up to a factor of 10. The output of the summing amplifier is sent to a dual-channel 100 V amplifier that outputs a symmetric positive and negative signal, amplified by a factor of ten. It is convenient that this is a 100 V amplifier because it allows the application of

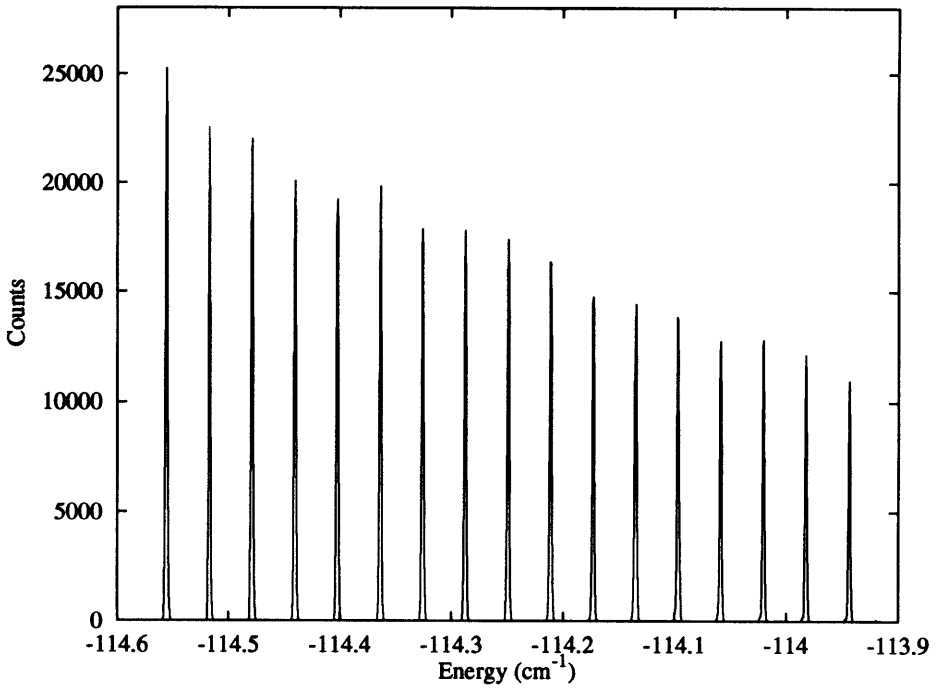

Figure 4-17: Experimental measurement of a region of the $n = 31$ Stark manifold for a field strength $F = 9.409$ V/cm.

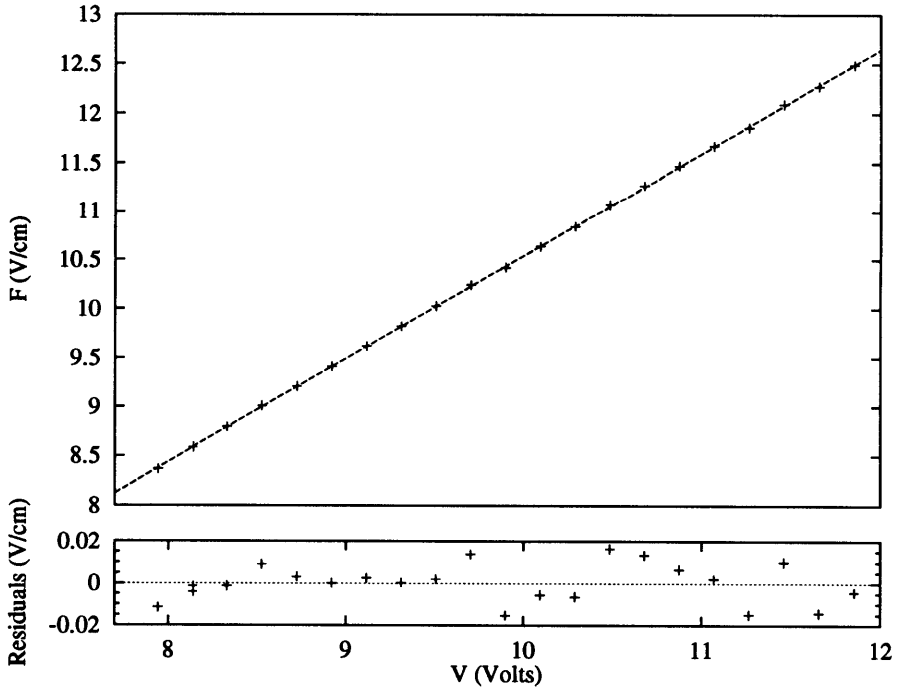

Figure 4-18: Least squares fit to F vs. V calibration data. The result is $F = (1.0525 \pm 0.0017)V + (0.020 \pm 0.016)$ V/cm.

larger voltages needed for field calibrations. Finally, the outputs are directed through low-pass filters that remove 60 Hz noise and also smooth the voltage as it is swept during the measurement of a recurrence spectrum.

A hardware calibration is done by measuring the output voltage as a function of D/A value and doing a least squares fit. Thus there are four parameters relating the electric field seen by the atoms to the setting of the data acquisition program: offset and slope of voltage vs. D/A setting and offset and slope of field vs. voltage setting. The advantage of this scheme is that the intermediate standard (Keithley model 2000 Digital Multimeter) does not need to be accurate. Its reading needs to be only linear and constant over time.

4.10 Recurrence Spectroscopy

All of the above elements must be combined to measure recurrence spectra. The laser energy, static electric field, rf field amplitude, and rf frequency must be simultaneously varied to hold the classical scaling laws given in Sec. 2.1 constant. The process begins with what we call a "prescan", in which the yellow laser is scanned over its range and iodine and etalon peaks are recorded. The laser energy at each point is determined from these data, and the static electric field, rf field amplitude, and rf frequency required at each point are calculated. The rf field amplitude to be used at each point is corrected according to the calibration. The spectrum is then recorded by scanning the laser again while setting the external fields to their predetermined values. For most of the experiments described in this thesis, the signal was measured for 200 ms at each point.

Data acquisition is similar to that described in [Cou95], but modified for the oscillating field. The HP8662A is controlled via a GPIB bus. The offset for the static voltage is set by changing the appropriate D/A channel and simultaneously measuring the voltage with the Keithley.

4.10.1 Error Analysis

The following analysis is for the spectra gathered at $\epsilon = -0.4$, which are described in Chapter 6. The other experiments, near $\epsilon = -2$, were done at smaller static field strengths, and have correspondingly larger errors. However, those experiments focus on low-action behavior, so they have a larger tolerance for error.

The uncertainty in setting the scaled energy is

$$\frac{\delta\epsilon}{\epsilon} = \sqrt{\left(\frac{\delta E}{E}\right)^2 + \left(\frac{1}{2}\frac{\delta F}{F}\right)^2} \tag{4.12}$$

$$= \sqrt{\left(10^{-3}\right)^2 + \left(\frac{1}{2}10^{-3}\right)^2} \approx 10^{-3}. \tag{4.13}$$

The uncertainty in setting the scaled rf field amplitude is

$$\frac{\delta\tilde{f}}{\tilde{f}} = \sqrt{\left(\frac{\delta F_1}{F}\right)^2 + \left(\frac{\delta F}{F}\right)^2} \tag{4.14}$$

$$= \sqrt{\left(10^{-1}\right)^2 + \left(\frac{1}{2}10^{-3}\right)^2} \approx 10^{-1}. \tag{4.15}$$

(The relative uncertainty in $\tilde{f}$ is about 10^{-2}). The uncertainty in setting the scaled rf frequency is

$$\frac{\delta\tilde{\omega}}{\tilde{\omega}} = \sqrt{\left(\frac{\delta\omega}{\omega}\right)^2 + \left(\frac{3}{4}\frac{\delta F}{F}\right)^2} \tag{4.16}$$

$$= \sqrt{\left(10^{-10}\right)^2 + \left(\frac{3}{4}10^{-3}\right)^2} \approx 10^{-3}. \tag{4.17}$$

The uncertainty in setting $\tilde{f}$ and $\tilde{\omega}$ is limited by knowledge of the static field, while ϵ is limited by knowledge of the laser energy.

The data in this thesis at $\epsilon = -0.4$ were obtained via single scans of the laser covering $145 < w = F^{-1/4} < 160$. The quality of the Fourier transform is characterized by two quantities: the width of a peak and the maximum action. The width of

a peak is determined by the range of w,

$$\delta\tilde{S} = \frac{1}{2\pi\Delta w} = \frac{1}{20} = 0.05. \tag{4.18}$$

The maximum action is determined by the step size in w,

$$\tilde{S}_{\max} = \frac{\pi}{2\pi w_{\text{step}}} = \frac{1}{2\frac{1}{4}w\frac{F_{\text{step}}}{F}} \approx 30. \tag{4.19}$$

(This equation arises from considering that an orbit produces oscillations in the spectrum if the phase $2\pi\tilde{S}w$ is uncertain to less than π [MWW+94].)

The scaling laws give flexibility in where to conduct the experiment. The spectrum can be measured from say $100 < w < 120$ or $200 < w < 220$ with the same results. (There are small difference associated with quantum-mechanical effects because these two measurements have different effective values of Planck's constant. The measurement with the larger w is more classical.) We use this flexibility in w advantageously when measuring spectra in the oscillating field, for which the frequencies are limited to below 1260 MHz, which are small compared to typical low-n electron orbital frequencies of many GHz. By using small static electric fields and high energies, where the orbital frequencies are lower, we are able to use the low frequencies and still approach the orbital period of the electron. The other constraint is the scaled energy ϵ. At small fields, the spectra become dense and the high resolution of the cw lasers becomes critical.

Figures 4-19 and 4-20 plot the relationships between laboratory values of energy and frequency and their scaled counterparts ϵ and $\tilde{\omega}$. Conducting recurrence spectroscopy at stronger electric fields, or in the diamagnetic system, is laborious with our system because the lasers need to be manually mode-hopped over many wave numbers. Pulsed experiments with low-resolution lasers such as the hydrogen experiment at Bielefeld, Germany, are appropriate to study these systems. However, the experiments described here require our high-resolution lasers and precise knowledge of field strengths.

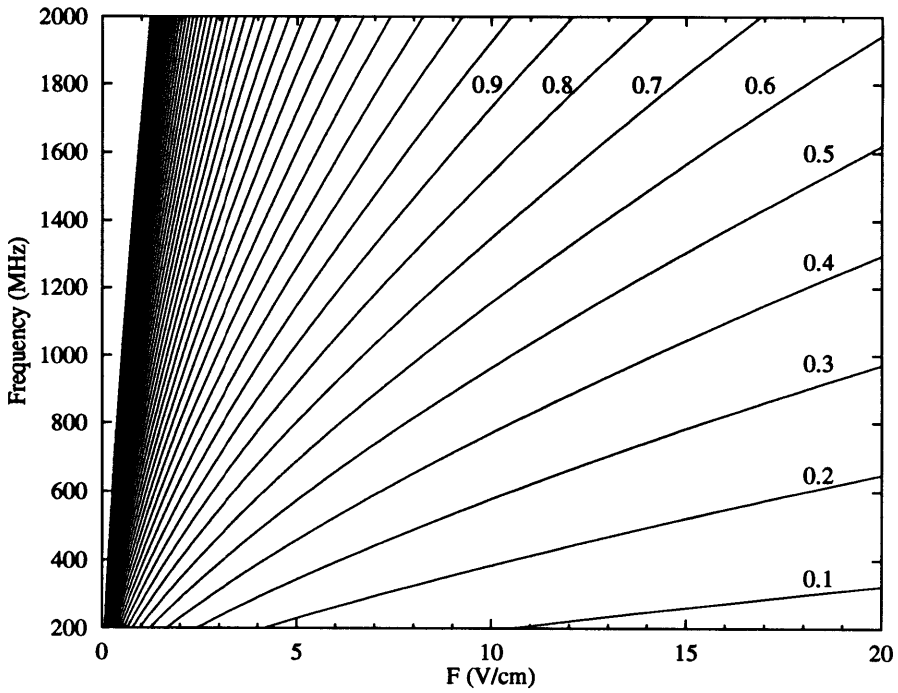

Figure 4-19: Frequency of oscillating field ω vs. static field strength F. Each line shows some scaled frequency $\tilde{\omega} = \omega F^{-3/4}$, given on the diagram for some of the lines. The highest frequency plotted is $\tilde{\omega} = 5.0$.

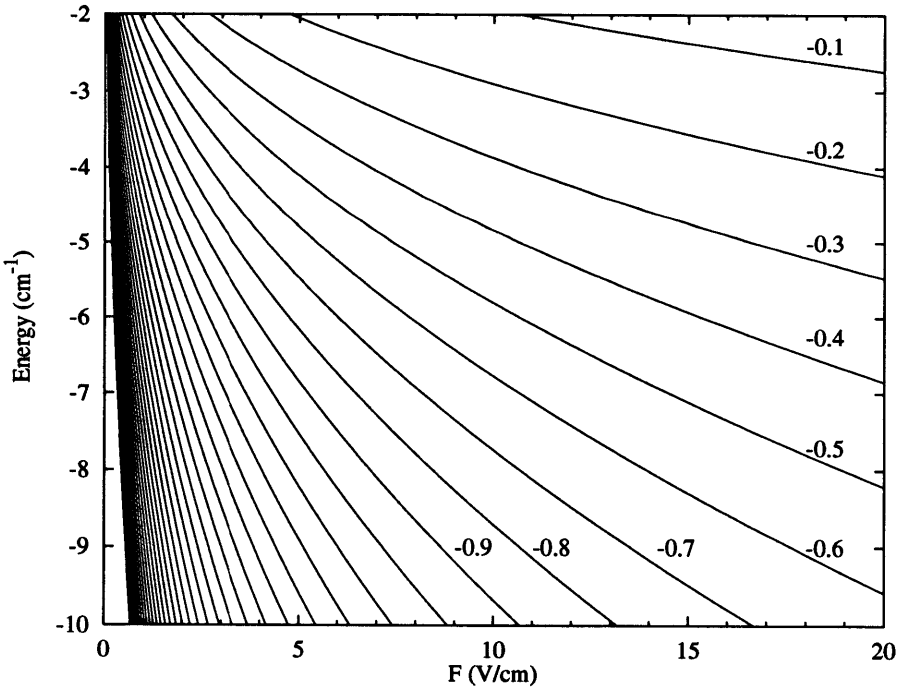

Figure 4-20: Laser energy E vs. static field strength F. Each line shows some constant scaled energy $\epsilon = EF^{-1/2}$, given on the diagram for some of the lines. The lowest energy plotted is $\epsilon = -4.0$.

Chapter 5

Recurrence Spectroscopy in a Static Electric Field

To provide a foundation for interpreting our experiment in a static and oscillating field, in this chapter we describe recurrence spectra in a static electric field. Because much has been written on this subject [ERWS88, CSJK95, Cou95, GD97], the principal goal here is to examine the quality and reproducibility of the experimental data by comparing them with the predictions of closed orbit theory and semiquantal computations. The discussion focuses on behavior at a scaled energy $\epsilon = -0.4$, which is the energy at which spectra in an oscillating field are examined in Chapter 6. Experimental and computed spectra near the saddle point ($\epsilon = -2$) are also examined. The bifurcation structure in this region, not previously studied in detail, is an interesting problem in itself. Furthermore, this investigation is necessary because the orbit reconstruction discussed in Chapter 7 demands a detailed understanding of behavior in this regime. A result of the analysis is a measurement of the periods of the 2/3 and 3/4 orbits at an energy $\epsilon = -2.05$. The values of these periods are used in Chapter 7.

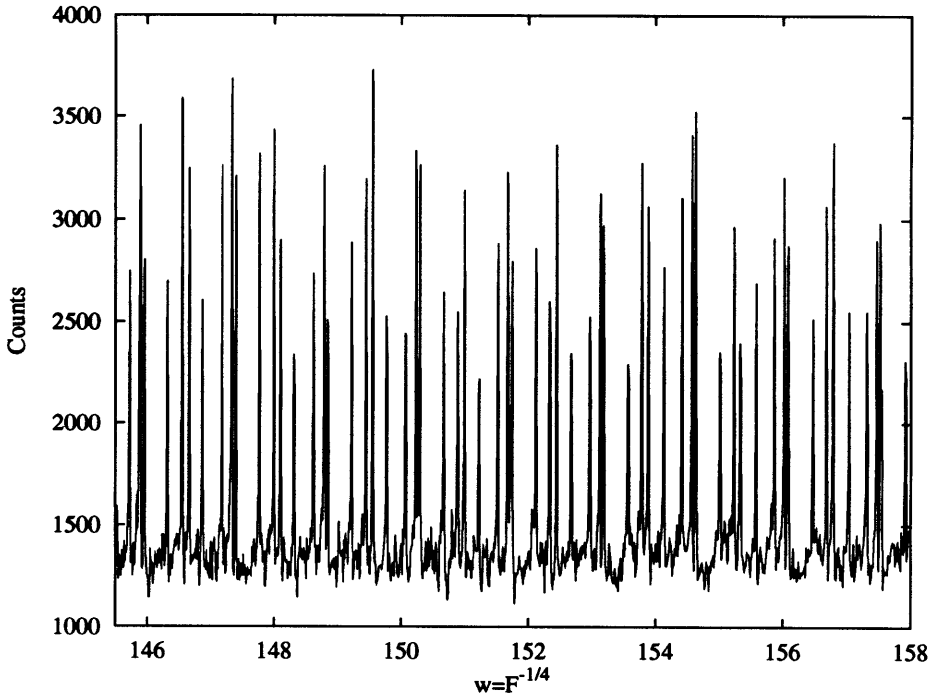

Figure 5-1: Untransformed experimental scaled spectrum of lithium $m = 0$ states at $\epsilon = -0.4$. The horizontal axis is $w = F^{-1/4}$, the vertical axis is counts. At each point, signal was recorded for 200 ms. The electric field was varied from $F = 11.46$ V/cm to $F = 8.22$ V/cm while the energy was varied from $E = -4.14$ cm^{-1} to $E = -3.51$ cm^{-1}.

5.1 Recurrence Spectra, $\epsilon = -0.4$

Figure 5-1 displays an untransformed experimental scaled spectrum of lithium $m = 0$ states collected in a electric field that varied along with the laser energy to maintain $\epsilon = -0.4$. Because the energy is well above the electric field saddle point, there is a large, slowly varying continuum background resulting from ionization of electrons over the saddle point. Above this background are many narrow, long-lived states.

A recurrence spectrum, generated by computing the Fourier transform[1] of Fig. 5-1, is shown in Fig. 5-2. The uphill parallel orbit and its repetitions create the primary structure of equally spaced peaks because other more complicated orbits that con-

[1]The Fourier transform is computed numerically by explicitly summing the Fourier series over all points in the spectrum and plotting the absolute-square. The measured spectrum is windowed with a sine function before transformation.

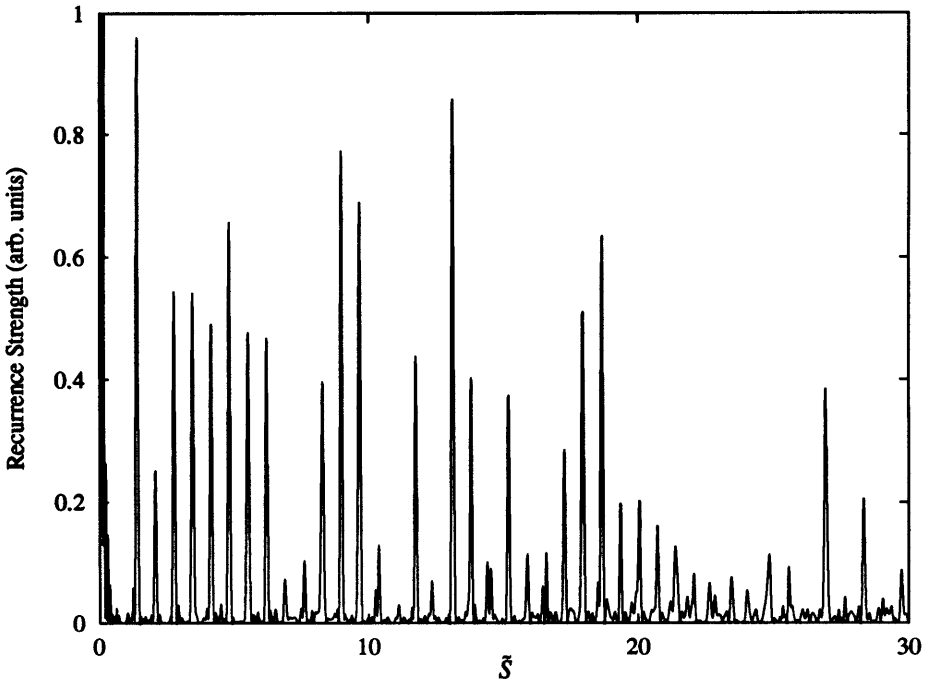

Figure 5-2: Experimental recurrence spectrum, $\epsilon = -0.4$. This is the Fourier transform of Fig. 5-1. The large low-frequency component ($\tilde{S} < 0.3$) is not plotted in the other figures in this thesis.

tribute to the spectrum have actions that are close to the actions of repetitions of the parallel orbit. The action of the parallel orbit at $\epsilon = -0.4$ is $\tilde{S} = 0.690$. The first repetition is not easily visible because its strength is close to the background noise level. The second repetition is enhanced by the proximity of the 1/2 bifurcation, which occurs at $\epsilon = -0.397$.

5.1.1 Experimental Reproducibility

Several factors produce variations between experimental spectra measured under identical conditions. There can be spurious noise peaks, but these are rare and need not be considered. Some fluctuations in the measured signal strength arise from statistical counting noise. The spectra typically have around 1000 counts per point, implying fluctuations of 3%. The largest effect results from the finite step size by which the laser energy and electric field strength are changed, and so the intensity of narrow peaks varies if the laser energy does not hit the maximum point in a peak. Fluctua-

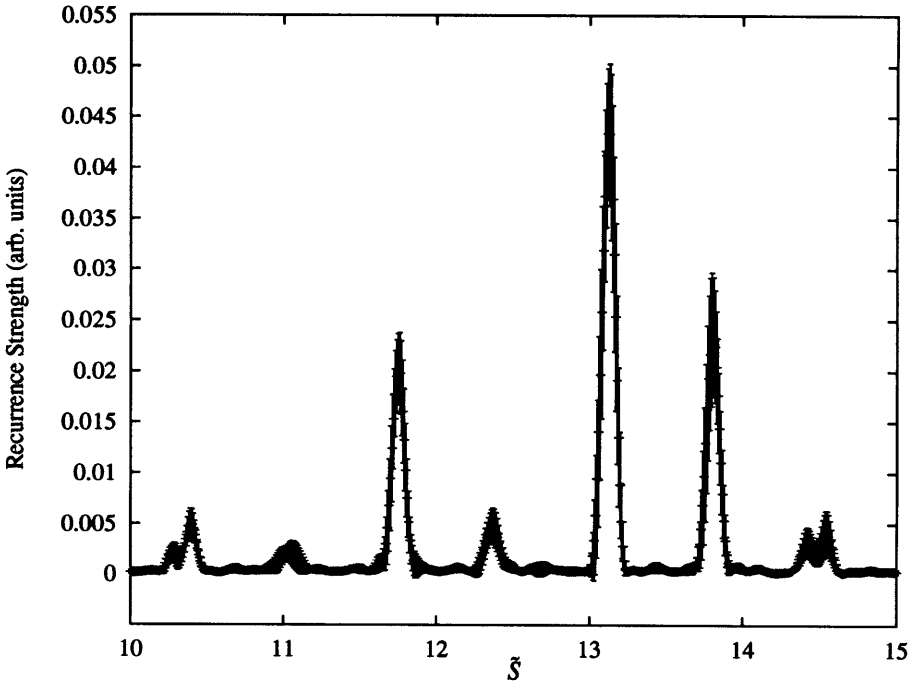

Figure 5-3: A section (compare with Fig. 5-2) of the average of nine experimental recurrence spectra, $\epsilon = -0.4$. The standard deviation to the average at each point is plotted as an error bar on each point. The resulting thick line is an indication of the size of error in a measurement of the spectrum.

tions in the laser energy also cause problems in two ways. The energy is calibrated from the position of iodine absorption lines measured in the prescan before the recurrence spectrum is measured. The laser must not move in energy after the prescan. If the laser does move, the result is an error in setting the scaled energy and following the scaling law. Finally, the laser can move *during* a scan. Fortunately, this is a rare event, and is usually noticeable in the spectrum.

To assess the reproducibility, Fig. 5-3 shows a section of a spectrum obtained by averaging nine different recurrence spectra measured on four different occasions over a one-month period. Standard deviations of the average are plotted as error bars on each point. The strength of the stronger peaks is reproducible with a precision of about 20%.

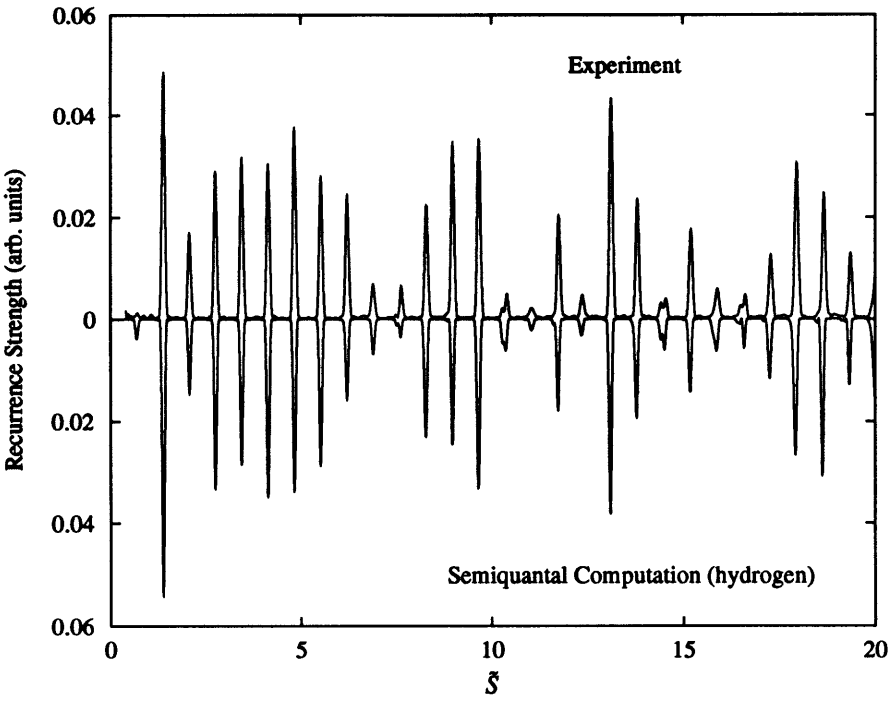

Figure 5-4: Comparison between the averaged spectrum from Fig. 5-3 and the semiquantal computation for $\epsilon = -0.4$. The scans are scaled for best overall agreement.

5.1.2 Comparison with Computation and Theory

Figure 5-4 compares the average experimental recurrence spectrum, Fig. 5-3, with a semiquantal computation for hydrogen developed by Vladimir Kondratovich [Kon]. The computational approach combines standard semiclassical methods that give quantized energy levels in a static electric field with a recently developed semiclassical formula [KD97b] that relates the oscillator strength to the square of the quantum angular distribution of outgoing waves evaluated at the angle at which the electron leaves the atom along a semiclassically quantized trajectory [KD97a]. Good agreement is seen with the experiment. The largest discrepancy is for the weak first repetition. A hydrogenic approximation to the spectra works well at this high energy where core-scattering is weak. We will see in the next chapter that this semiquantal computational method can be adapted to calculate spectra in the oscillating field.

Figure 5-5 compares the averaged spectrum with a closed-orbit-theory calculation by Jing Gao [Gao]. The calculation includes quantum effects that are important near

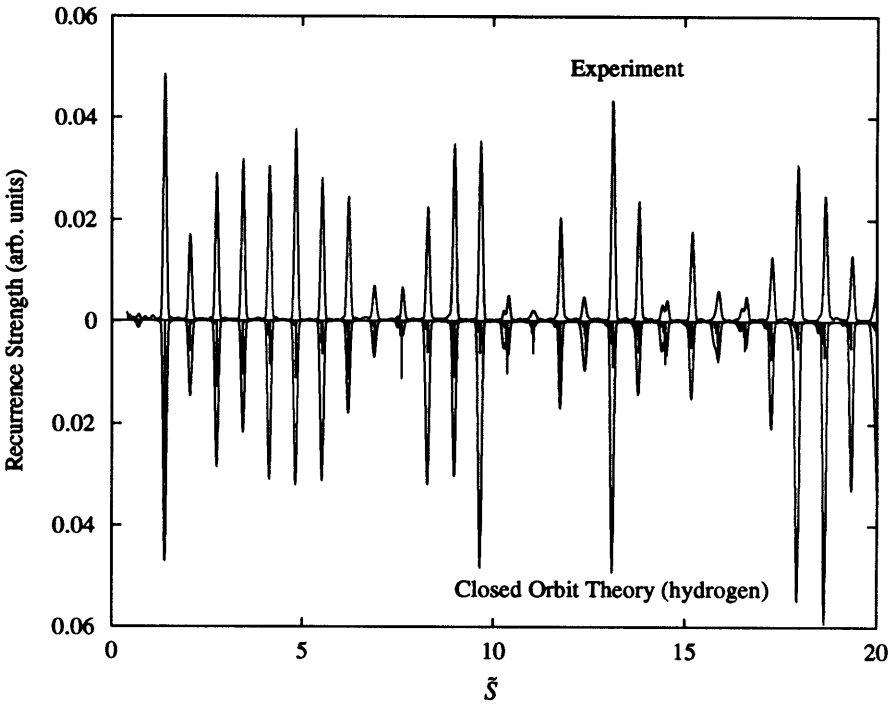

Figure 5-5: Comparison between the averaged spectrum and closed orbit theory for hydrogen at $\epsilon = -0.4$. The scans are scaled for best overall agreement. The needles show the contributions of individual orbits.

bifurcations [CJS+95, GD97]. Agreement is good, although the strengths of the recurrences at high action are a little larger than both the experiment and semiquantal computation. The agreement with the strength of the first repetition is better than it was for the semiquantal calculations. Both the semiquantal computation and closed orbit theory predict a smaller amplitude for the 13th repetition than is seen in the experiment. This may be the result of scattering from the lithium ionic core. Quantum computations for lithium which could reveal core-scattering are unfortunately unavailable to us in this continuum regime.

We have seen that the experiment produces recurrence spectra that agree with semiquantal computations. Although similar agreement has been seen with closed orbit theory [CJS+95], the spectra studied here were recorded at significantly higher principal quantum numbers and much smaller electric fields.

The significance of these results is that we have a reliable experimental technique by which a recurrence spectrum can be measured with a single laser scan. Because

the high-n states have lower characteristic frequencies, the experiments in Chapters 6 and 7 could be performed with relatively low-frequency applied fields. Furthermore, the speed and simplicity of a single laser scan enabled a deeper investigation of the three-parameter oscillating field system.

5.2 Bifurcation Structure and the Measurement of Orbital Periods

To analyze the measurements to be discussed in Chapter 7, we will need values for the periods of the 2/3 and 3/4 orbits at $\epsilon = -2.05$. These quantities are easily calculated classically, but are challenging to find quantum mechanically through recurrence spectra. Nevertheless, because a central goal of this thesis is to extract classical information from quantum spectra, we undertook such a measurement.

Classical mechanics relates the period of an orbit to its action by $\tilde{T} = (2\pi)\partial\tilde{S}/\partial\epsilon$.[2] This formula is easily applied to isolated peaks in recurrence spectra by measuring their action at several values of ϵ and finding the slope. However, the procedure is challenging to apply in regions where several orbits with similar action contribute to a recurrence. Indeed, the method fails if the experimental resolution is not sufficient to resolve individual orbits unless one can argue that only a single orbit contributes significantly to the recurrence strength. A special experimental difficulty in the measurements described here is that, because small electric fields were used, the actions of recurrences are more sensitive to stray electric fields than they were in the $\epsilon = -0.4$ measurements described in Sec. 5.1.

Figure 5-6 shows low-action experimental recurrence spectra measured at energies near the saddle point, $\epsilon = -2$. Two types of bifurcations occur in this region. One is the bifurcation of an orbit from a repetition of the uphill orbit. These bifurcations are described in [CJS+95], and are well understood. The 6/7 and 7/8 bifurcations of this type produce the strong recurrences at the action of U_7 and U_8 in Fig. 5-6.

[2]The factor 2π results from our definition of $\tilde{S}$.

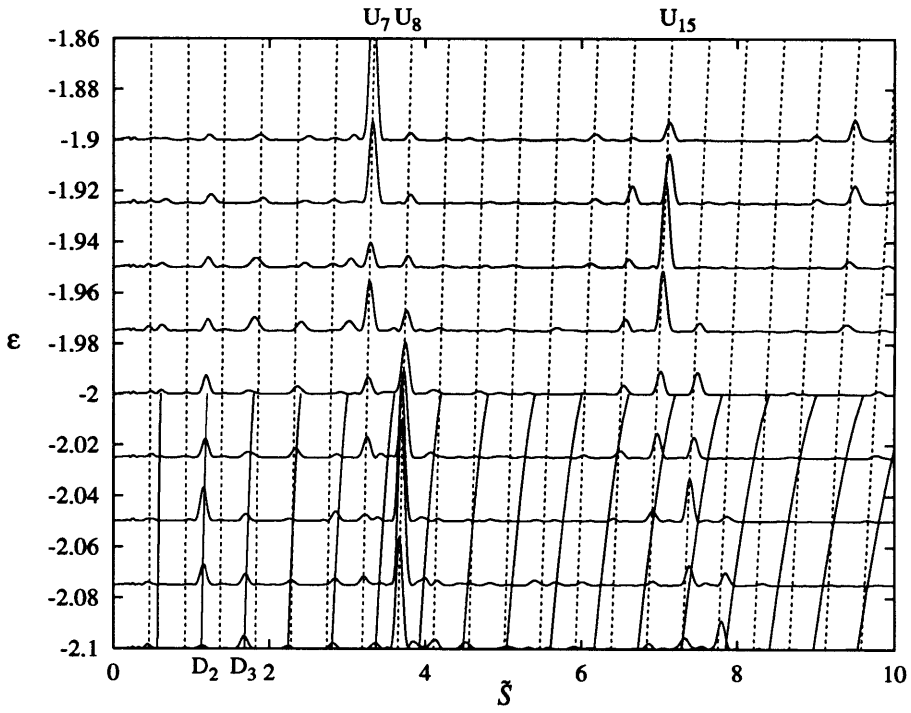

Figure 5-6: Experimental recurrence spectra near $\epsilon = -2$. Laser energy was scanned from $E = -7.25$ cm^{-1} to $E = -6.61$ cm^{-1} as the electric field was varied to maintain a constant scaled energy. The spectrum at $\epsilon = -1.9$ covers $240 < w < 251$ while the spectrum at $\epsilon = -2.1$, which needed a smaller electric field for the lower scaled energy, covers $252 < w < 264$. The intermediate spectra cover ranges of w intermediate between these extremes. The dashed lines mark the actions of the uphill parallel orbits U_k. The solid lines terminating at $\epsilon = -2$ mark the actions of the downhill parallel orbits D_k. The strong recurrences at the action of U_7 and U_8 are caused by the 6/7 and 7/8 bifurcations, respectively. The principal contribution to the recurrence at the action of D_2 is from the 2/3 orbit, while the principal contribution to the recurrence at the action of D_3 is from the 3/4 orbit.

The second type is the bifurcation of an orbit into the downhill orbit. As the energy increases across the saddle point, complex infinite sequences of these bifurcations occur (see Figs. 2-5 and 2-6). Spectra in this regime have been previously published [CJS+95], but without detailed analysis. The peaks in Fig. 5-6 at the action of D_2 and D_3 are generated in this second type of bifurcation. The strength of the peak at D_2 is primarily generated by the 2/3 orbit, while the peak at D_3 is generated by the 3/4 orbit, with some contribution from the 3/5 and 3/6 orbits.

The high-action peaks in Fig. 5-6 (e.g. U_{15}) are shifted with respect to the classical actions of repetitions of the uphill orbit. This may result from a residual stray electric field of larger than usual size. The electric field in these spectra is quite small, typically $F \approx 1.2$ V/cm. An error of 10 mV/cm corresponds to a shift in action of 0.02 at $\tilde{S} = 10$. Comparison with the observed shift in Fig. 5-6 indicates that the error in setting F must be 20 to 30 mV/cm. This is larger than expected, but not unthinkable. Nevertheless, much information, qualitative and quantitative, can be extracted from these spectra. The principal reason for this is that the effect of an error in field strength is a shift in action proportional to the size of the error. The measured period, which is found from the *slope* of the action, is sensitive to such an error only to second order.

In conjunction with this study, V. Kondratovich computed the recurrence spectrum using the method of Sec. 5.1.2. Figure 5-7 shows the results [Kon]. The measurements in Fig. 5-6 were augmented with a second data set collected on a different day. The computed spectra are compared with this second set in the expanded plot shown in Fig. 5-8. The absence of noise and the large range of w in the computed spectra allow a more accurate analysis of the behavior than can be achieved from the experimental results. In addition to the recurrences that are observed in the experimental data, a few peaks are clearly visible at some of the higher repetitions of the downhill orbit, such as D_6 and D_{11}. Note that because the strengths of these peaks are small (compare with the strong 6/7 and 7/8 orbits at U_7 and U_8), small errors in measurement cause relatively large fluctuations in the recurrence strength.

To analyze the data, the recurrences at D_2 and D_3 in the experimental and com-

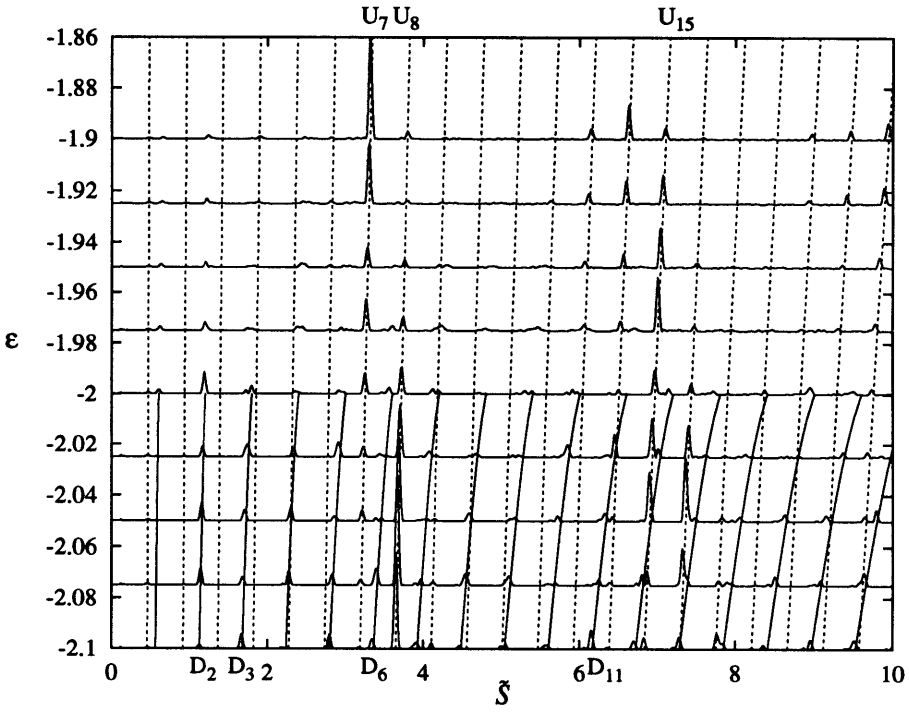

Figure 5-7: Computed recurrence spectra near $\epsilon = -2$. These spectra cover $240 < w < 265$. The dashed lines mark the actions of the uphill parallel orbits U_k. The solid lines extending to $\epsilon = -2$ mark the actions of the downhill parallel orbits D_k. The labels U_k and D_k identify recurrences discussed in the text. Compare with Fig. 5-6.

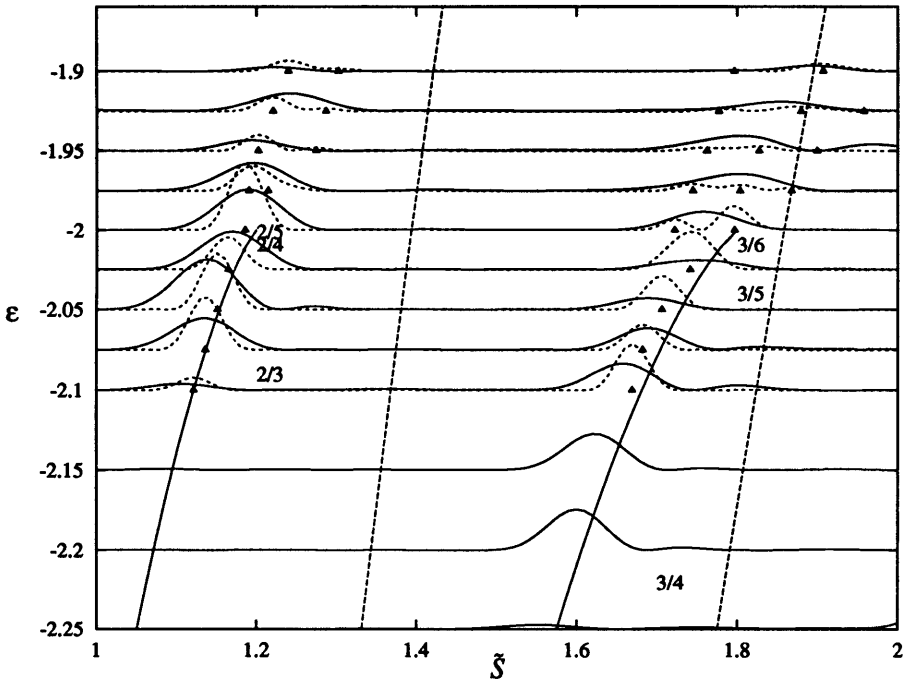

Figure 5-8: Experimental (solid line) and computed (dashed line) recurrence spectra near $\epsilon = -2$. The computed spectra are enlarged from Fig. 5-7. The experimental spectra are a second data set complementary to that in 5-6. Solid lines extending to $\epsilon = -2$ mark the action of the downhill orbits D_2 and D_3. Dashed lines mark the action of the uphill orbits U_3 and U_4. Triangles are actions of recurrences extracted by fitting the computed spectra to Gaussians. The fractions indicate the locations of bifurcations listed in Table 5.1.

Orbit	ϵ_{up}	ϵ_{down}
2/3	-0.795	-2.092
2/4	-0.397	-2.009
2/5	-0.244	-2.001
3/4	-1.113	-2.220
3/5	-0.608	-2.041
3/6	-0.397	-2.009

Table 5.1: Bifurcation energies for several orbits important in spectra near $\epsilon = -2$. The energy at which the orbit m/n bifurcates from the nth repetition of the uphill orbit is ϵ_{up}. The energy at which the orbit m/n bifurcates into the mth repetition of the downhill orbit is ϵ_{down}.

puted spectra have been fitted to Gaussians to extract the actions of the recurrences. The results for the computed spectra are shown in Fig. 5-8 and compared with the results for the experimental spectra and classical computations in Figs. 5-9 and 5-10. The peaks in the computed spectra are narrower because they are computed using a larger range of w than for the experimental spectra. Consequently, they reveal the presence of other orbits with greater clarity.

We begin by examining the recurrences near the action of the 2/3 orbit. As a reference, Table 5.1 gives the bifurcation energies of several of the important orbits in this region. The resolution of the experiment is so low that only a single recurrence is visible in Fig. 5-8, whereas the computed spectra reveal that a small recurrence develops near $\epsilon = -1.95$ and evolves to higher action as ϵ increases to -1.9. However, it is weak, and the primary contribution to the low-resolution measurement arises from the 2/3 orbit. The classical calculation shown in the lower half of Fig. 5-9 reveals that the 2/4 and 2/5 orbits bifurcate from the downhill orbit and evolve toward higher action as ϵ increases. Comparison between the top and bottom of the figure leads to the conclusion that the secondary recurrence in the computed data is generated by the 2/4 and 2/5 orbits. The computed spectra clearly reveal that the 2/3 orbit produces the primary contribution to the recurrence strength. Although there is some scatter in the positions, the experimental data are consistent with this conclusion.

The period is extracted by fitting the actions of the 2/3 orbit to a line and taking its

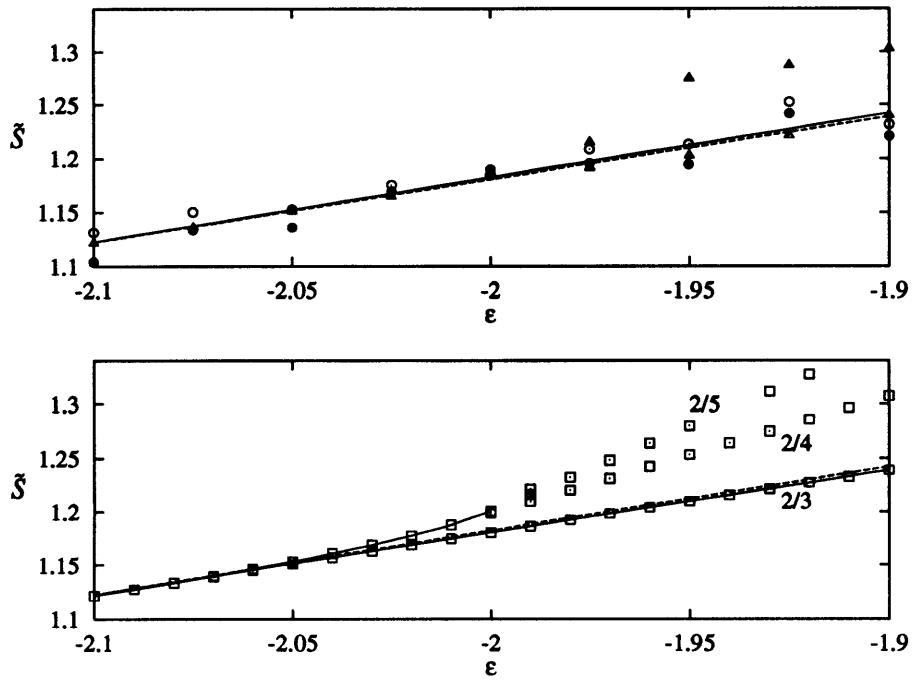

Figure 5-9: Action of the 2/3 orbit in a bifurcation region: measurement and theory. Top: Circles are experiment (solid and open represent two data sets). Triangles are semiquantal computation. The solid line is a fit to the experimental data. The dashed line is a fit to the semiquantal computation. Bottom: Boxes are computed classical actions of some orbits in this region. The curved line ending to $\epsilon = -2$ is the action of the downhill orbit D_2. The other orbits are the 2/3, 2/4, 2/5, and (at $\epsilon = -1.99$) the 2/6. The solid and dashed lines are the fit from the upper plot. The fit to the experiment yields $\tilde{S} = (0.60 \pm 0.05)\epsilon + 2.38$, implying $\tilde{T} = 3.75 \pm 0.31$. The fit to the semiquantal computation yields $\tilde{S} = (0.57 \pm 0.02)\epsilon + 2.33$, implying $\tilde{T} = 3.60 \pm 0.12$.

slope. The results plotted in Fig. 5-9 for the experimental data and for the computed spectra agree well with each other and with the classical action of the 2/3 orbit. The result of the least squares fit for the measured data is $\tilde{T} = 3.75 \pm 0.31$, in good agreement with the actual period, $\tilde{T} = 3.720$. The result for the computed spectra is $\tilde{T} = 3.60 \pm 0.12$. The uncertainties here are statistical, and do not include possible effects from neighboring orbits or errors in field calibration.

Now, we turn to the 3/4 orbit. Our interest in this orbit developed after the spectra were obtained, and unfortunately the measurements do not focus on its region

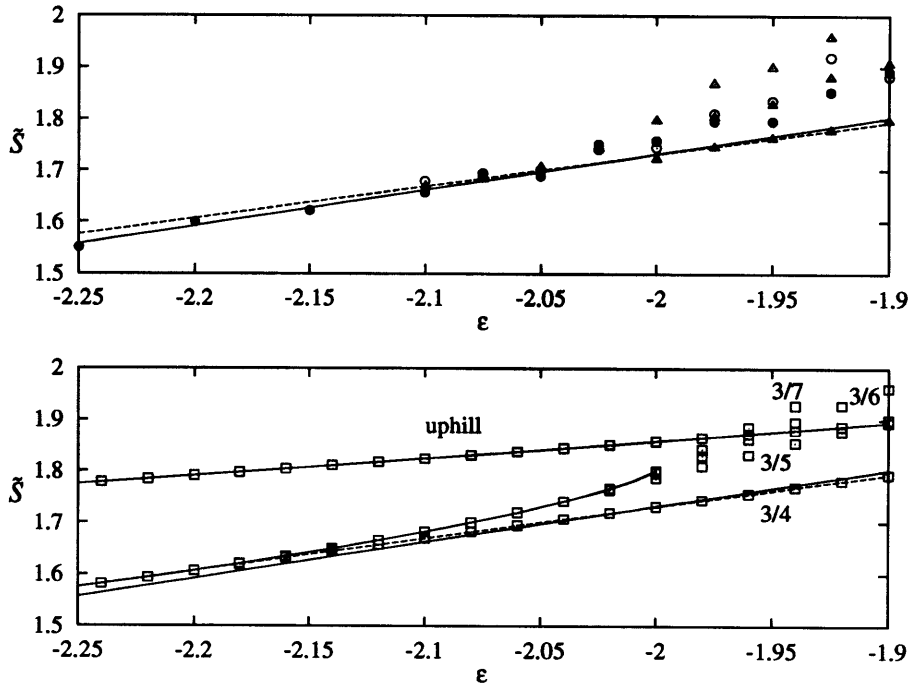

Figure 5-10: Action of the 3/4 orbit in a bifurcation region: measurement and theory. Top: Circles are experiment (solid and open represent two data sets). Triangles are semiquantal computation. The solid line is a fit to the experimental data. The dashed line is a fit to the semiquantal computation. Bottom: Boxes are computed classical actions. The curved line ending to $\epsilon = -2$ is the action of the downhill orbit D_3. The other orbits are the 3/4, 3/5, 3/6, and 3/7. The solid and dashed lines are the fit from the upper plot. The fit to the experiment for $\epsilon \leq -2.05$ yields $\tilde{S} = (0.70 \pm 0.05)\epsilon + 3.13$, implying $\tilde{T} = 4.40 \pm 0.31$. The fit to the semiquantal computation yields $\tilde{S} = (0.62 \pm 0.02)\epsilon + 2.97$, implying $\tilde{T} = 3.91 \pm 0.15$.

of greatest strength, $-2.25 \leq \epsilon \leq -2$. The computed spectra in Fig. 5-8 reveal that as ϵ increases the 3/4 orbit loses recurrence strength more rapidly than did the 2/3 orbit as ϵ increased above -2. As the 3/4 orbit loses recurrence strength, others gain until they have equal strength near $\epsilon = -2.025$, where a single recurrence with action equal to the average of its constituents is visible. At higher ϵ, the various orbits separate, and the 3/4 orbit is again visible in the computed spectra. However, it is too small to be seen in the experimental spectra. Figure 5-10 compares actions extracted from the experimental and computed spectra with the classical calculations. Because of

the superior resolution of the computations, we can use values of the action of the 3/4 orbit for $\epsilon \leq -1.9$ to extract the period, whereas we must limit the experimental data to $\epsilon \leq -2.05$. A fit gives $\tilde{T} = 4.40 \pm 0.31$ for the experimental data and $\tilde{T} = 3.91 \pm 0.15$ for the computation. The computed result is in much better agreement with classical value, $\tilde{T} = 3.915$, than is the experimental result.

Because of the problems of interpreting recurrence spectra, particularly in regions of bifurcations, the critical reader might remain unconvinced that we have actually observed the 2/3 and 3/4 orbits here. However, the measurement with an oscillating field described in Chapter 7 will clearly show that these recurrences are primarily generated by these orbits. The results of this section reveal that although one can in principle measure classical quantities from quantum spectra, actually doing it may not be easy.

Chapter 6

Recurrence Spectroscopy in an Oscillating Field

This chapter describes experimental recurrence spectra measured in parallel static and oscillating electric fields. The results are compared with the semiclassical theory described in Chapter 2 and with the results of approximate semiquantal Floquet computations. Recurrence spectra generated with the computational methods described in Chapter 3 are presented and compared with closed orbit theory. The results for hydrogen show good agreement with closed orbit theory. A core-scattered orbit in lithium is also examined, and an attempt to predict its interaction with the oscillating field is discussed. Many of the results here have been published in the paper reprinted in Appendix D.

6.1 Confrontation Between Experiment and Theory at $\epsilon = -0.4$

We chose to work at $\epsilon = -0.4$ for our first experimental studies of recurrence spectra in a time-dependent field because the regime is experimentally accessible, many repetitions of recurrences at the action of the parallel orbit are strong and easily studied, and because the proximity of the 1/2 bifurcation at $\epsilon = -0.397$ held the possibility

of interesting behavior.

Figures 6-1 and 6-2 show recurrence spectra recorded at two fixed values of $\tilde{f}$ as $\tilde{\omega}$ is varied. Among the prominent features in these spectra are the strong second repetition at $\tilde{S} = 1.4$ that is largely unaffected as $\tilde{\omega}$ changes, regions where all recurrences are eliminated, and other band-like regions where the recurrences maintain their strength. As will be explained, these bands exist close to where the period of a repetition of the parallel orbit is an integer multiple of the period of the oscillating field.

Because the frequency of the field is a variable in these plots, it is natural to compare the periods of the orbits to the frequency of the field, for it is reasonable to expect that the period of an orbit may determine how it interacts with a time-periodic perturbation. However, a recurrence spectrum is plotted with respect to action, and, because the period and action of an orbit are related by $T = \partial S/\partial E$, the action of an orbit does not indicate its period. We choose to relate the action of a recurrence to its period using the ratio of period to action for the uphill orbit U_1, and use this ratio to draw curves that mark the action accumulated by an orbit in the time that the oscillating field completes an integer number of cycles.

Most of the orbits contributing to the recurrences have periods and actions similar to some repetition of the uphill parallel orbit because they were created in bifurcations from it. The ratio of action to period for any of the strong recurrences is therefore close to the ratio for the uphill orbit because strong recurrences are typically close to their bifurcation energy. From a classical analysis at $\epsilon = -0.4$, the orbit U_1 has $\tilde{S}_1 = 0.690$ and $\tilde{T}_1 = 1.35$. The time for the field to oscillate through n cycles is $\tilde{t} = (2\pi/\tilde{\omega})n$, and in this time an electron moving along the z axis accumulates action $\tilde{S} = (\tilde{S}_1/\tilde{T}_1)\tilde{t}$. Therefore, lines of constant time along which an orbit with a period and an action equal to a repetition of the uphill orbit experiences a constant number of field-cycles are given by the expression

$$\tilde{\omega} = 2\pi \left(\frac{\tilde{S}_1}{\tilde{T}_1}\right) \frac{n}{\tilde{S}}. \tag{6.1}$$

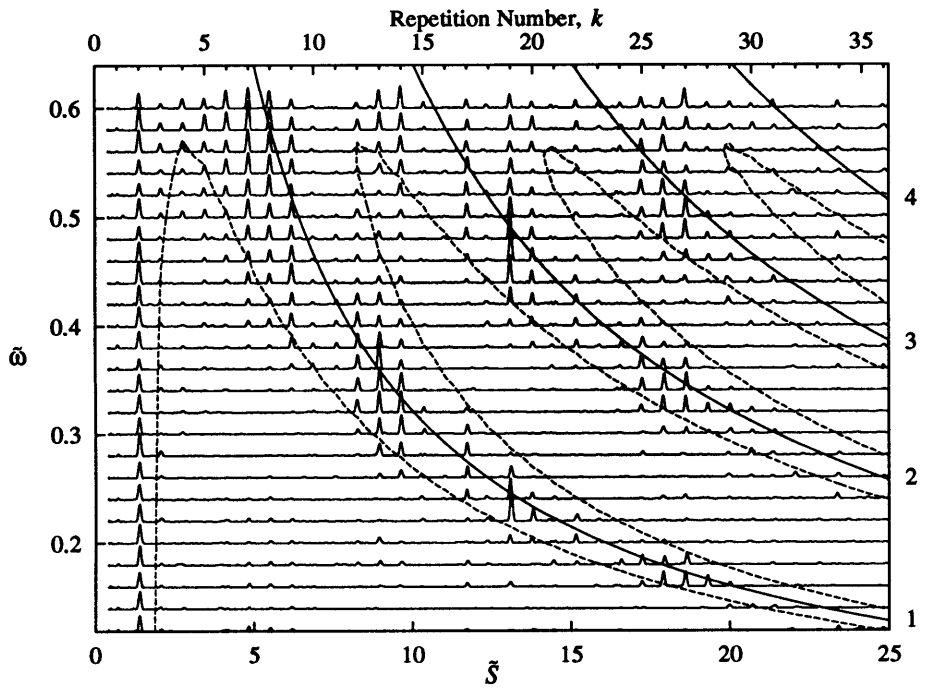

Figure 6-1: Experimental recurrence spectra, $\epsilon = -0.4$, $\tilde{f} = 0.005$, $0.12 \leq \tilde{\omega} \leq 0.6$. Data come from measurements in the range $146 \leq w \leq 158$. The dashed lines are contours generated from Eq. (6.3), marking where $a_k = 0.2$. The solid curved lines mark the action at which a repetition of the uphill orbit has a period that is an integer multiple n (listed on the right) of the period of the applied field. The axis on the top marks the number of repetitions k completed by the uphill orbit.

This relation is plotted with solid curved lines in Figs. 6-1 and 6-2. The surviving recurrences are clustered near these lines, meaning that trajectories with orbital periods that are an integer multiple of the period of the field are least perturbed. This result was surprising, for we had expected that these orbits, which are in some sense resonantly perturbed, would be the most affected.

For a deeper understanding of the behavior, Fig. 6-3 shows a slice through Fig. 6-1 at $\tilde{\omega} = 0.32$ for increasing $\tilde{f}$. All of the recurrences lose strength as $\tilde{f}$ is increased. Some fall off quickly while others persist to much stronger fields. The persistent recurrences belong to the bands in Figs. 6-1 and 6-2. Additionally, most of the recurrences show one or two small revivals as the field is made yet stronger. We will

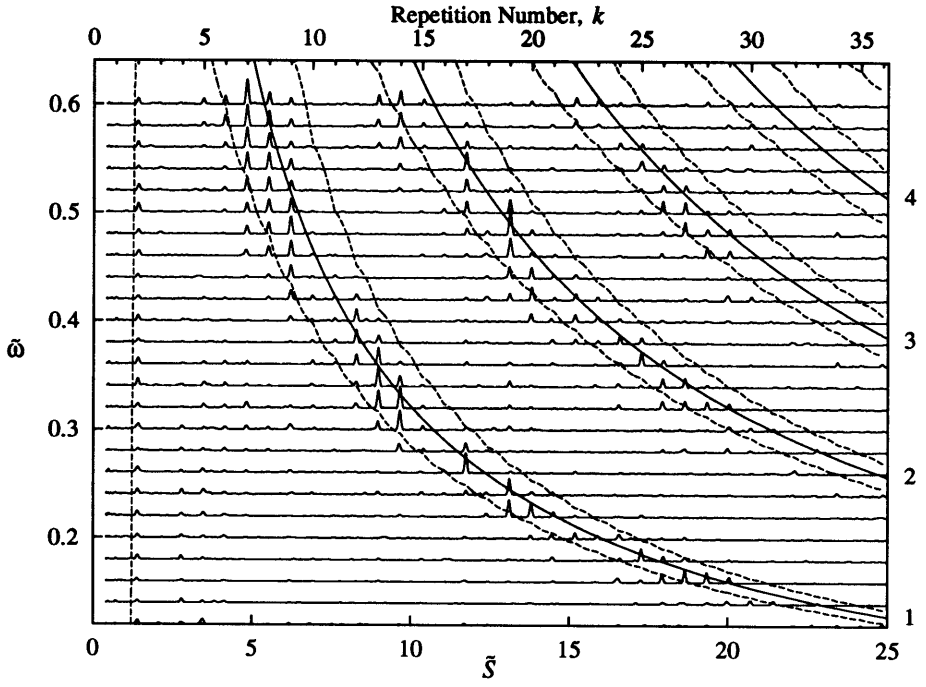

Figure 6-2: Experimental recurrence spectra, $\epsilon = -0.4$, $\tilde{f} = 0.008$, $0.12 \leq \tilde{\omega} \leq 0.6$. See the caption of Fig. 6-1 for a description of the quantities plotted here. The overall scaling is the same as for the $\tilde{f} = 0.005$ data.

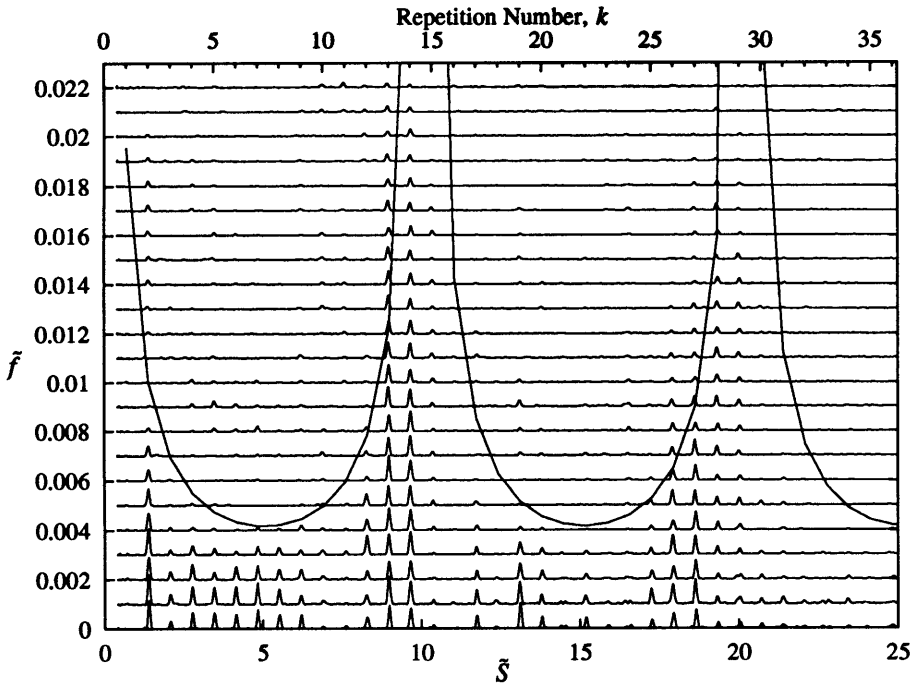

Figure 6-3: Experimental recurrence spectra, $\epsilon = -0.4$, $\tilde{\omega} = 0.32$, $0.0 \leq \tilde{f} \leq 0.022$. The solid lines mark the positions of the first zero in the recurrence strength as predicted by closed orbit theory restricted to the uphill parallel orbit.

examine these data in two ways. The first approach uses the approximation that all the orbits in the system have periods and actions equal to the uphill orbit. This allows the derivation of simple analytic formulas which describe the overall spectral structure. The second approach employs a detailed calculation using closed orbit theory with an exact treatment of the properties of all the orbits in the system. However, as a preliminary step to gain confidence in the accuracy of our data, we present the results of semiquantal Floquet computations of the spectra.

6.1.1 Semiquantal Floquet Computations

Approximate semiquantal Floquet computations of these spectra were developed by V. Kondratovich. These computations combine the ideas of Floquet analysis, discussed in Sec. 3.4, with the 'semiquantal' method outlined in Sec. 5.1.2. The development of this computational method was motivated by the experimental results, following the tradition in which experiments motivate computations, which in turn give confidence in the experiments and suggest new directions. Once the computations are trusted, they can be better than the experiment for making detailed studies because they do not suffer from limitations in resolution, calibration, and noise. The computational method is described in [KD97a]. In contrast with the methods presented in Chapter 3, these computations do not take into account the lithium core. However, we have seen in Chapter 5 that the hydrogenic calculations for a static field work well at $\epsilon = -0.4$, and therefore should be valid here in the oscillating field.

Figures 6-4 and 6-5 show the results of these calculations [Kon], done over the same range of w as the corresponding experimental spectra. The agreement with the experimental spectra inspires confidence in both theory and experiment. Figure 6-6 is a mirror plot of experiment and Floquet computation for $\tilde{\omega} = 0.32$ and $\tilde{f} = 0.005$. Although there are small discrepancies, the overall agreement is satisfying. In particular, both show weak recurrences near $\tilde{S} = 5$ and $\tilde{S} = 14$, and strong recurrences near $\tilde{S} = 9$ and $\tilde{S} = 18$. We will show later that the weak recurrences have lost their strength because of their proximity to the first minimum in the Bessel function, Eq. (2.51). Among other things, these results suggest that the calibration

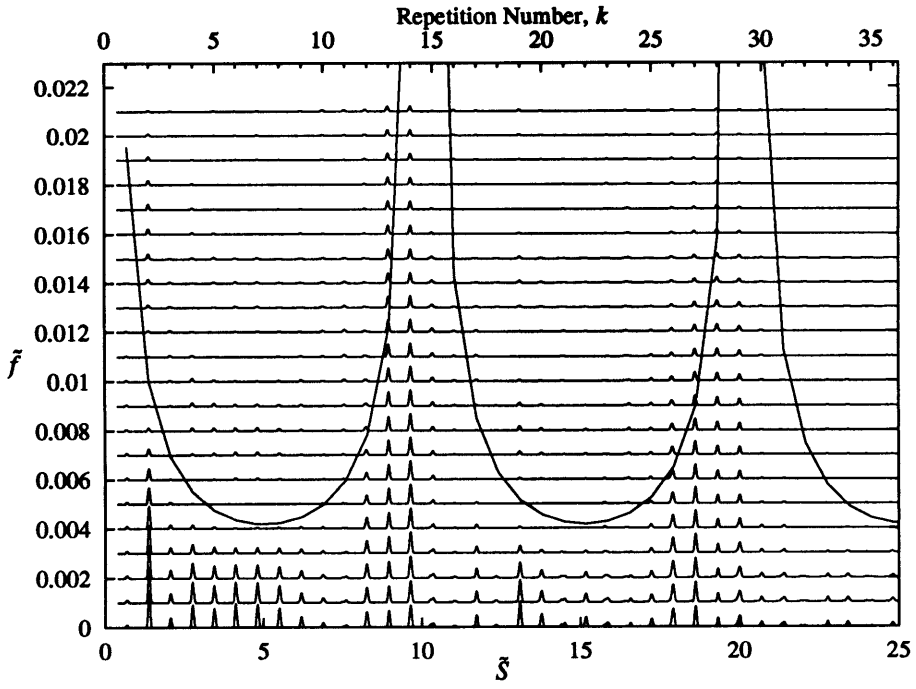

Figure 6-4: Semiquantal Floquet computation, $\epsilon = -0.4$, $\tilde{\omega} = 0.32$, $0.0 \leq \tilde{f} \leq 0.021$. Compare with Fig. 6-3.

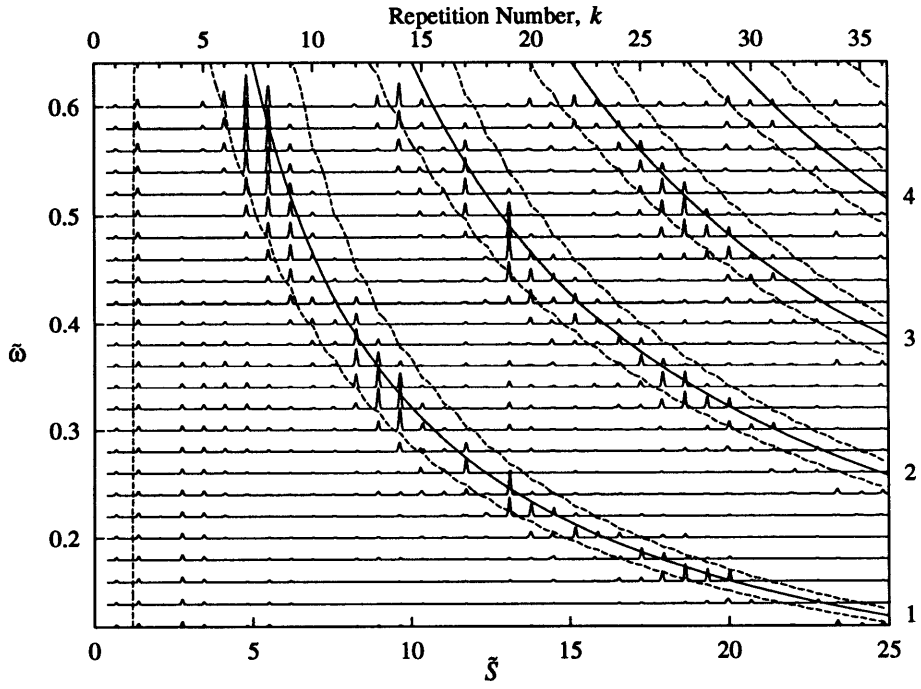

Figure 6-5: Semiquantal Floquet computation, $\epsilon = -0.4$, $\tilde{f} = 0.008$, $0.12 \leq \tilde{\omega} \leq 0.60$. Compare with Fig. 6-2.

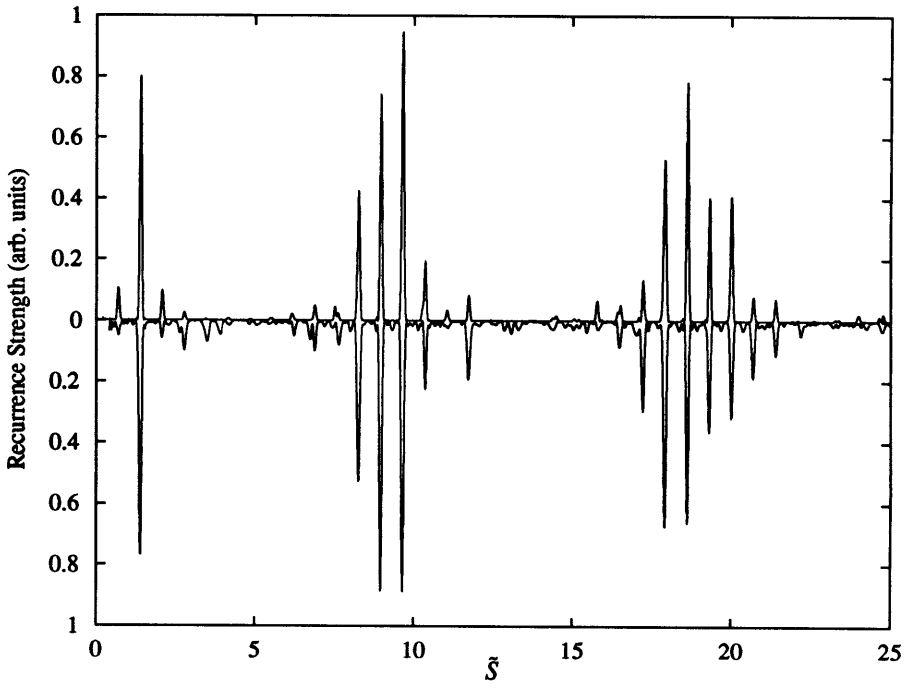

Figure 6-6: Recurrence spectra, $\epsilon = -0.4$, $\tilde{\omega} = 0.32$, $\tilde{f} = 0.005$. Top: Floquet computation. Bottom: Experiment. Overall strengths are scaled for best agreement.

of the rf field amplitude, described in Sec. 4.8, is accurate. Further comparisons with the experiment and closed orbit theory at other frequencies and field amplitudes are shown in Fig. 6-12.

6.1.2 A Test of Closed Orbit Theory

The spectra shown in the previous sections allow a detailed test of time-dependent closed orbit theory, described in Chapter 2. In this section, we make the simplifying approximation that each of the orbits has a period and an action equal to some repetition U_k of the uphill parallel orbit. We refer to this approximation as the "restricted" theory. With this simplification it is unnecessary to compute the recurrence strength of each orbit, for we need only examine the change in its strength relative to its unperturbed recurrence strength.

According to the discussion in [HD97], the magnitude of the ac dipole moment

for the kth repetition of the parallel orbit is related to that for the first by

$$\left|\tilde{Z}_k(\tilde{\omega})\right| = \left|\tilde{Z}_1(\tilde{\omega})\right| \left|\frac{\sin(k\tilde{\omega}\tilde{T}_1/2)}{\sin(\tilde{\omega}\tilde{T}_1/2)}\right| , \tag{6.2}$$

where $\tilde{T}_1$ is the period of the first repetition, U_1. It follows from Eq. (2.51) that as $\tilde{f}$ is increased at a fixed value of $\tilde{\omega}$, each recurrence is weakened by a factor a_k given by

$$a_k = J_0^2\left(\tilde{f}\left|\tilde{Z}_1(\tilde{\omega})\right| \left|\frac{\sin(k\tilde{\omega}\tilde{T}_1/2)}{\sin(\tilde{\omega}\tilde{T}_1/2)}\right| w\right) \equiv J_0^2(c_k\tilde{f}) . \tag{6.3}$$

Figure 6-7 shows the magnitude of the ac dipole moment, $|\tilde{Z}_k(\tilde{\omega})|$, as a function of repetition number and frequency, calculated as outlined in Sec. 2.3 for the uphill orbit. Because $|\tilde{Z}_k(\tilde{\omega})|$ is proportional to the falloff coefficient c_k, the factor a_k can be found from this surface using Eq. (6.3). Because a_k has a maximum value of unity where $c_k = 0$, the curved valleys in Fig. 6-7 correspond to the peaks in Figs. 6-1 and 6-2. The peaks in those recurrences are composed of orbits with small ac dipole moments which interact weakly with the oscillating field. From Eq. (6.2), the locations of these ridges are given by $k\tilde{\omega}\tilde{T}_1/2 = m\pi$, where m is an integer. From this, the condition $\tilde{T}_k = k\tilde{T}_1 = m\tilde{T}$ is found, where $\tilde{T}$ is the period of the field. We have already observed this result in Sec. 6.1, where we noted that recurrences with periods equal to an integer multiple of the period of the field were least perturbed. The ridges in Fig. 6-7, where orbits have large ac dipole moments, correspond to orbits that interact strongly with the field and thus show little or no recurrence strength in the oscillating field. Note that because Eq. (6.3) is just the *factor* by which the recurrence strength is reduced, weak recurrences along the ridges in Figs. 6-1 and 6-2 (see, for example, the $k = 10$ and $k = 11$ recurrences) do not conflict with the prediction of Fig. 6-7.

The dashed lines in Figs. 6-1 and 6-2 are contours corresponding to $a_k = 0.2$. Most strong recurrences fall inside these contours. A few recurrences, however, lie outside these regions. These are created by non-parallel orbits whose periods and shapes are different from the parallel orbit. For these orbits the restricted theory is not a good approximation. The treatment of these recurrences is discussed in the next section.

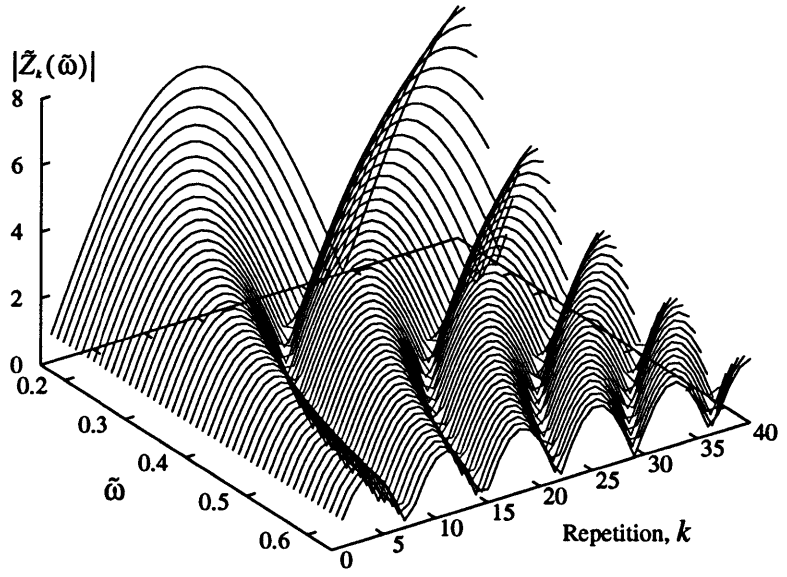

Figure 6-7: Classical calculation of the ac dipole moment $|\tilde{Z}_k(\tilde{\omega})|$ of the uphill parallel orbits U_k for $1 \leq k \leq 40$ and $0.12 \leq \tilde{\omega} \leq 0.64$ at $\epsilon = -0.4$. Although we plot it as a continuous function, $|\tilde{Z}_k(\tilde{\omega})|$ is defined only discretely at each closure.

Equation (6.3) predicts that as $\tilde{f}$ increases the recurrence strength of an orbit drops to zero and then shows second and successive maxima. Figure 6-8 compares the measured strength of the recurrence at U_2 with the prediction of Eq. (6.3) at $\tilde{\omega} = 0.32$. The experimental recurrence strength and the results of the Floquet computation are in good agreement with each other and with closed orbit theory. Because the energy $\epsilon = -0.4$ is close to the 1/2 bifurcation energy, $\epsilon = -0.397$, the 1/2 orbit contributes significantly to the recurrence and has nearly the same properties ($\tilde{S}$, $\tilde{T}$, $\tilde{Z}$) as U_2, and therefore the restricted theory should apply well. Indeed, classical calculations of c_k for the two orbits differ by only a part in a thousand. (The values of $|\tilde{Z}_k|$ for U_2 and 1/2 are 1.5814 and 1.5801, respectively.)

The curved solid lines in Figs. 6-3 and 6-4 plot the location of the first zero of the Bessel function (6.3) for the other repetitions of the uphill orbit. The overall structure is contained within the restricted theory, but there are some clear systematic differences. These are due to the approximation in the restricted theory and are explained in the detailed calculation described below.

We conclude this section by noting the similarity between the effect of the oscillating field shown in Fig. 6-8 and the recent results from the crossed-fields experiments in the Welge group [NUF+97]. They examine recurrence spectra of diamagnetic hydrogen as an electric field perpendicular to the magnetic field is turned on. They observed that recurrences fall off as squared Bessel functions. The reason for the similarity between these two seemingly different systems is that both involve symmetry breaking. The crossed-fields experiments involve spatial symmetry breaking, while the experiments here involve temporal symmetry breaking.

6.1.3 Detailed Closed Orbit Theory

Computing recurrence spectra in an oscillating field from time-dependent closed orbit theory is a complicated task. The first step is to find the closed orbits and their recurrence strengths in the time-independent system. Although these calculations are difficult because uniform approximations must be included near bifurcations, they have shown good agreement with experiments in electric fields [CJS+95]. Then, to

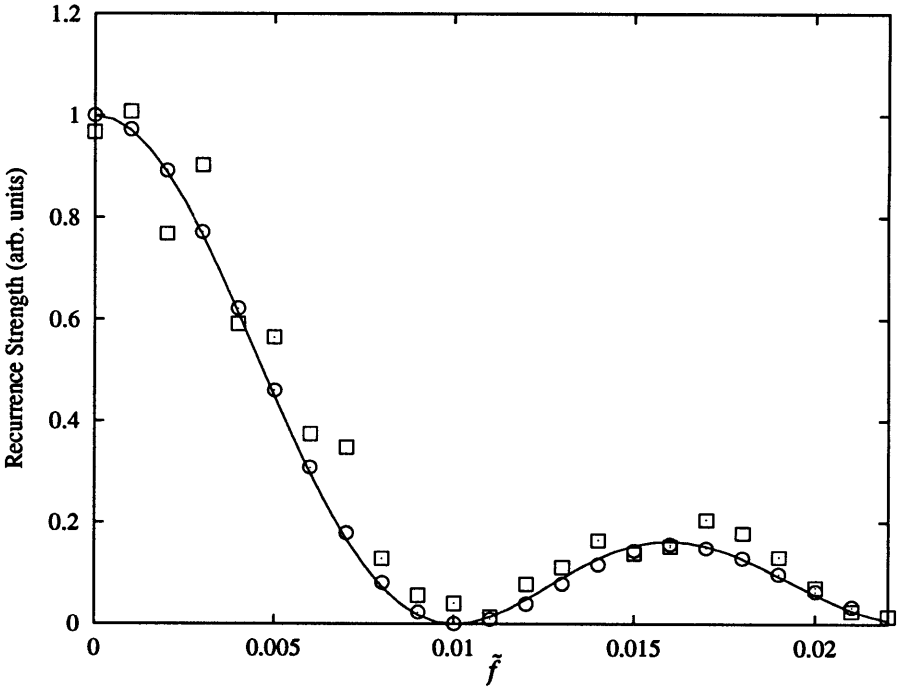

Figure 6-8: Strength of recurrence at U_2 vs. $\tilde{f}$ for $\epsilon = -0.4$ and $\tilde{\omega} = 0.32$. Squares: experiment. Circles: Floquet computation. Solid line: prediction of closed orbit theory for the uphill orbit U_2. The prediction for the $1/2$ orbit is indistinguishable from that for U_2 on this scale.

orbit	θ_0	$\tilde{S}$	$\tilde{T}$	$\left\|\tilde{Z}_k(\tilde{\omega}=0.32)\right\|$	$\tilde{f}_0 = 2.4/(\|\tilde{Z}_k\|w)$	Strength
U_{13}	0	8.973	17.57	1.223	0.013	4.9×10^{-4}
6/13	14.086891	8.968	18.45	0.662	0.024	6.4×10^{-3}
5/13	20.510503	8.939	20.02	0.193	0.082	2.0×10^{-3}

Table 6.1: Orbits contributing to the recurrence with action near the 13th repetition of the parallel orbit. θ_0 is the initial angle in degrees, $\tilde{f}_0$ is the field strength corresponding to the first zero in a_k. The column on the right is the relative recurrence strength of the orbits in a static field [Gao]. The calculations use the value $w = 152$ for comparison with the experiments.

incorporate the oscillating field, the ac dipole moment of each orbit at the frequency of interest must be computed. Finally, contributions from individual orbits are summed coherently and the result is convoluted with a Gaussian that matches the resolution of the experimental recurrence spectrum. We do not describe the details of such calculations here, but simply present results. A single orbit can dominate the strength of a recurrence, in which case it is adequate to calculate the falloff rate c_k of just that orbit. Before presenting general results, we illustrate the method for such a case.

The recurrence with action near the 13th repetition of the uphill parallel orbit, $\tilde{S} = 8.973$, is visible in Fig. 6-3, where it displays significant recurrence strength beyond the predicted zero at $\tilde{f} = 0.013$. Three orbits make large contributions to the strength of this peak: U_{13}, the 6/13 orbit, and the 5/13 orbit. Their properties are summarized in Table 6.1. The 6/13 and 5/13 orbits are illustrated in Figs. 6-9 and 6-10, respectively. They have similar actions, but periods that differ by more than 10%. The differences in the periods and the shapes of the orbits are manifest in their different ac dipole moments. The 6/13 orbit has the largest recurrence strength because it is close to its bifurcation energy. Its ac dipole moment indicates that this orbit should have a first zero at $\tilde{f} = 0.024$, and a glance at Fig. 6-3 shows that the recurrence does indeed approach zero close to this value, rather than near $\tilde{f} = 0.013$ as predicted for U_{13}. The small contribution from the parallel orbit quickly disappears, while the contribution of the 5/13 should persist to $\tilde{f} \approx 0.08$. This is our first example

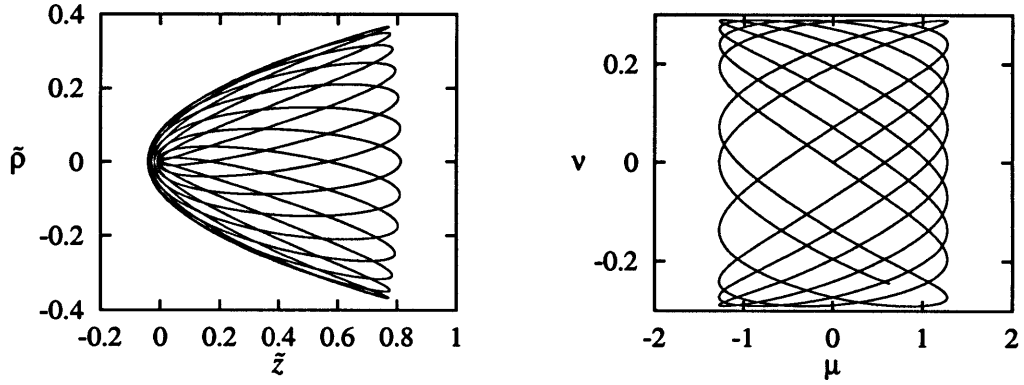

Figure 6-9: 6/13 orbit. Left: Trajectory in $(\tilde{z}, \tilde{\rho})$ coordinates. Right: Trajectory in (μ, ν) coordinates.

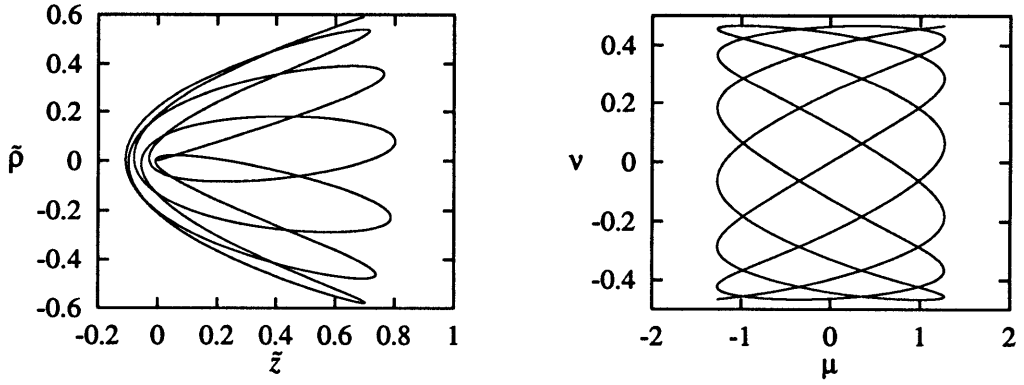

Figure 6-10: 5/13 orbit. Left: Trajectory in $(\tilde{z}, \tilde{\rho})$ coordinates. Right: Trajectory in (μ, ν) coordinates. Note that the scales differ from those in Fig. 6-9.

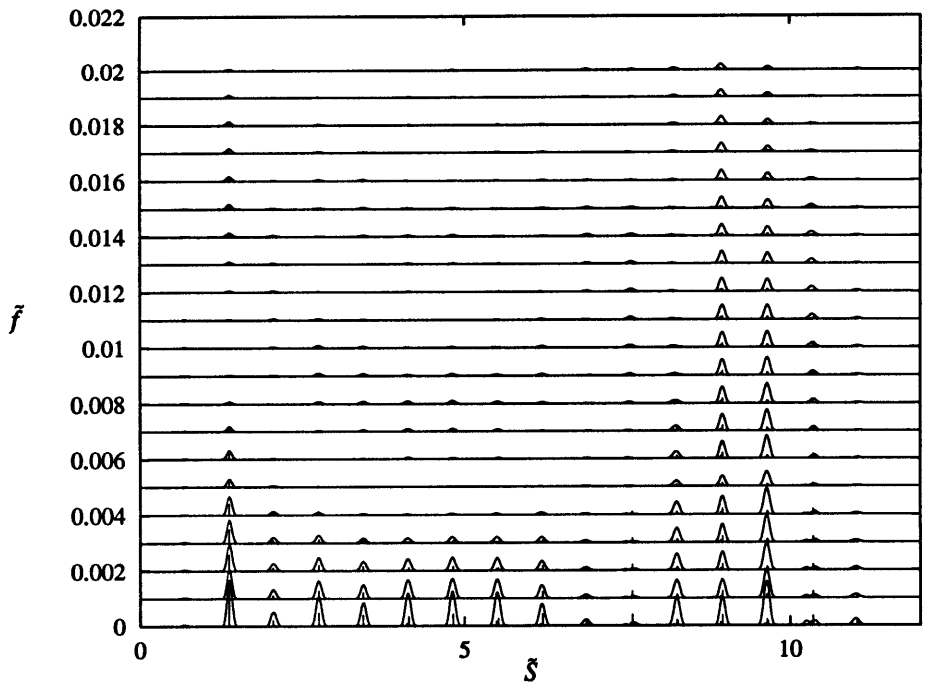

Figure 6-11: Closed orbit theory calculation of recurrence spectra, $\epsilon = -0.4$, $\tilde{\omega} = 0.32$, $0.0 \leq \tilde{f} \leq 0.020$. Compare with the experimental spectra in Fig. 6-3 and the semiquantal computations in Fig. 6-4.

of how the oscillating field serves as a tool to study the classical motion underlying these spectra: we clearly see that the 6/13 orbit is the primary constituent of the recurrence peak. The use of the oscillating field as a tool to study the properties of orbits is examined in greater detail in Chapter 7.

Figure 6-11 shows the results of detailed closed orbit calculations of the spectra at $\tilde{\omega} = 0.32$ [Gao]. These calculations were carried out for the same range of w as in the experiment. The needles are the strengths of each orbit, which are then convoluted to match the widths of the experimental peaks. Figure 6-12 compares the experiment with Floquet computation and closed orbit theory at several values of $\tilde{\omega}$. The Floquet computation and closed orbit theory show the greatest difference in the amplitude of the second repetition. for which the computation always predicts a larger amplitude. Comparison with experiment does not resolve which model, if either, is correct.

An efficient way to compare and summarize the predictions of the theoretical methods with the experimental data is to fit the peaks in Figs. 6-3, 6-4, and 6-11 to

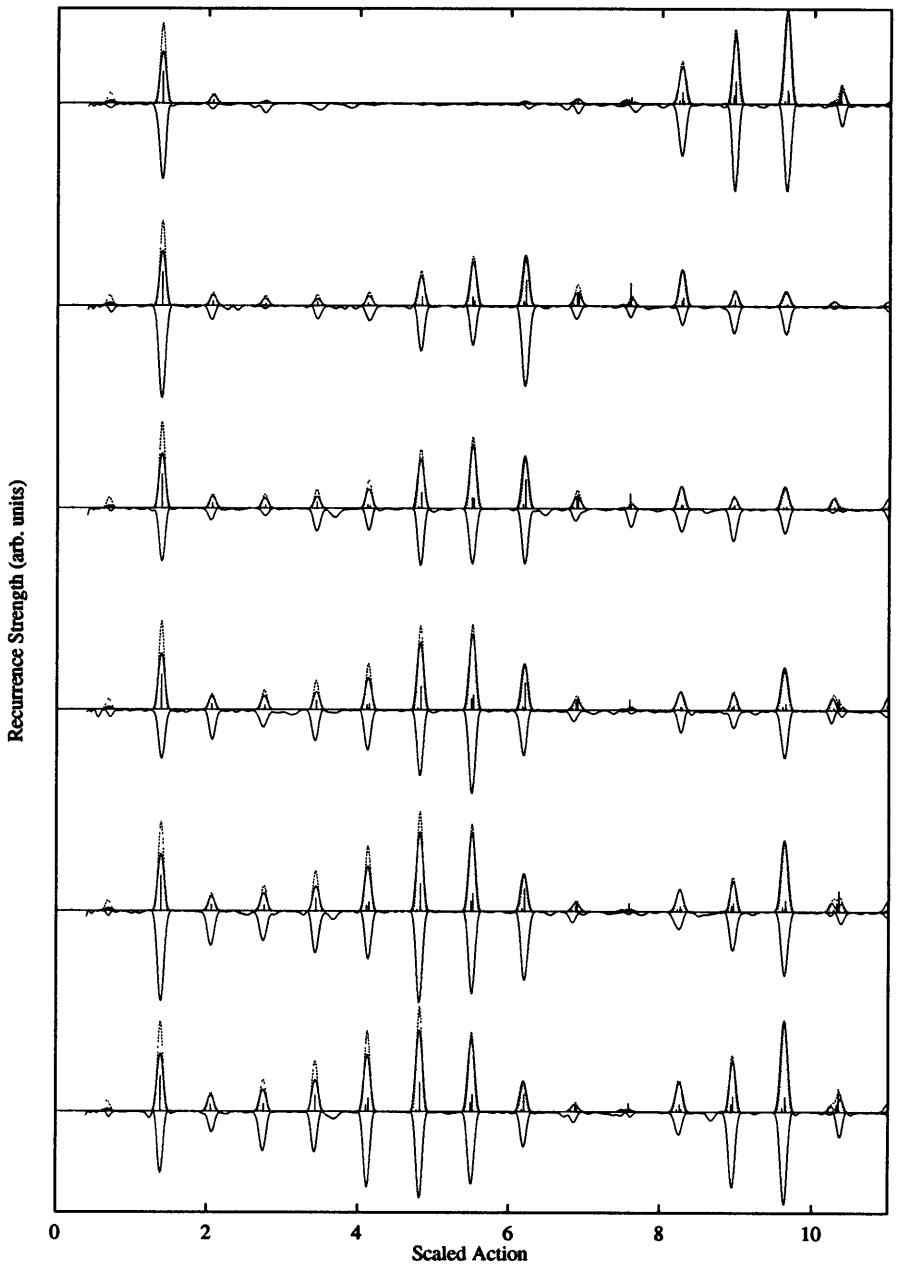

Figure 6-12: Comparison between closed orbit theory, Floquet computation, and experiment at $\epsilon = -0.4$, $\tilde{f} = 0.005$. Solid line: Closed orbit theory. Dashed line: Floquet computation. Inverted line: experiment. The values of $\tilde{\omega}$ from top to bottom are 0.32, 0.44, 0.48, 0.52, 0.56, 0.60. The dashed line is not visible in many places because of its good agreement with closed orbit theory. The overall scaling among the three approaches is adjusted for good agreement.

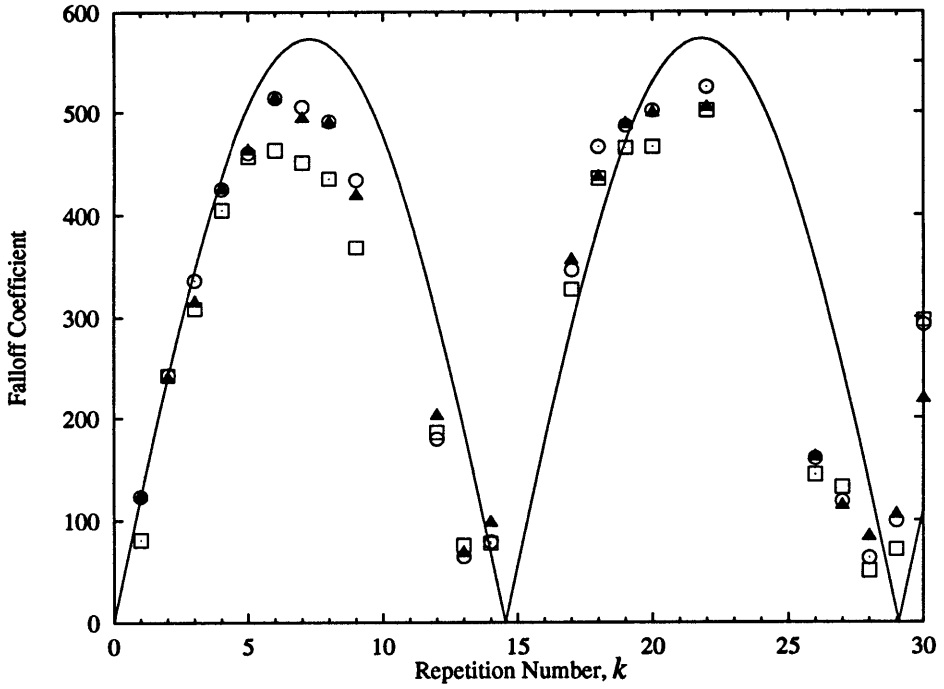

Figure 6-13: Falloff coefficients: experiment and theory. Solid line: Classical computation of $|\tilde{Z}_k(\tilde{\omega})|w$ for uphill orbits U_k for $\tilde{\omega} = 0.32$ and w=152. Points are fits of spectra at $\tilde{\omega} = 0.32$ to the form of Eq. (6.3). Squares are from experimental measurement (Fig. 6-3), circles are from Floquet computation (Fig. 6-4), and triangles are from closed orbit theory (Fig. 6-11).

the form of Eq. (6.3) and plot the resulting falloff coefficients c_k, as we have done in Fig. 6-13. Also shown is the prediction of the restricted theory, $c_k = |\tilde{Z}_k(\omega = 0.32)|w$, where $|\tilde{Z}_k|$ is computed for the uphill orbit. Note that many of the recurrences have several contributing orbits with different falloff coefficients, and therefore the general functional form is given by a sum of squared Bessel functions. Nevertheless, fitting to a single function is a useful way to summarize the data. The results reveal that while the restricted theory gives a good prediction of the overall behavior, an even better description is given by the detailed theory (triangles) that treats all of the orbits. The Floquet computations show excellent agreement with the closed orbit calculations. In the experimental data several repetitions show smaller falloff coefficients (e.g., $k = 6, 7, 8$). This is partially the result of noise. The recurrences with the largest coefficients have the fewest strong peaks in the spectrum, and consequently less averaging over noise occurs in the fitting process. The results could also indicate a slight under-calibration of the oscillating field strength. The size of miscalibration that this suggests is less than the estimated 10% accuracy of the calibration.

6.1.4 Untransformed Spectra

Recurrences arise from periodicities in the spectra, and so it is of some interest to look at the spectra themselves. Raw, untransformed spectra are shown in Fig. 6-14. As the strength of the oscillating field increases, the spectral lines develop sidebands which can combine with sidebands from other states to generate complex structures. Near $\tilde{f} = 0.005$, a pleasing orderly structure develops. This region is shown more clearly in Fig. 6-15.

These structures are examined and explained in [KD97a]. Figure 6-16 displays the development of the rf sidebands. Note that the step size in the experimental scans is similar to the width of the peaks, creating the pointed, triangular shaped peaks. Spectra with smaller step sizes can be obtained, but this time-consuming process is unnecesary for collecting recurrence spectra because they examine low-resolution behavior. In any case, the agreement between semiquantal computations and experiment at this level of detail give confidence in both.

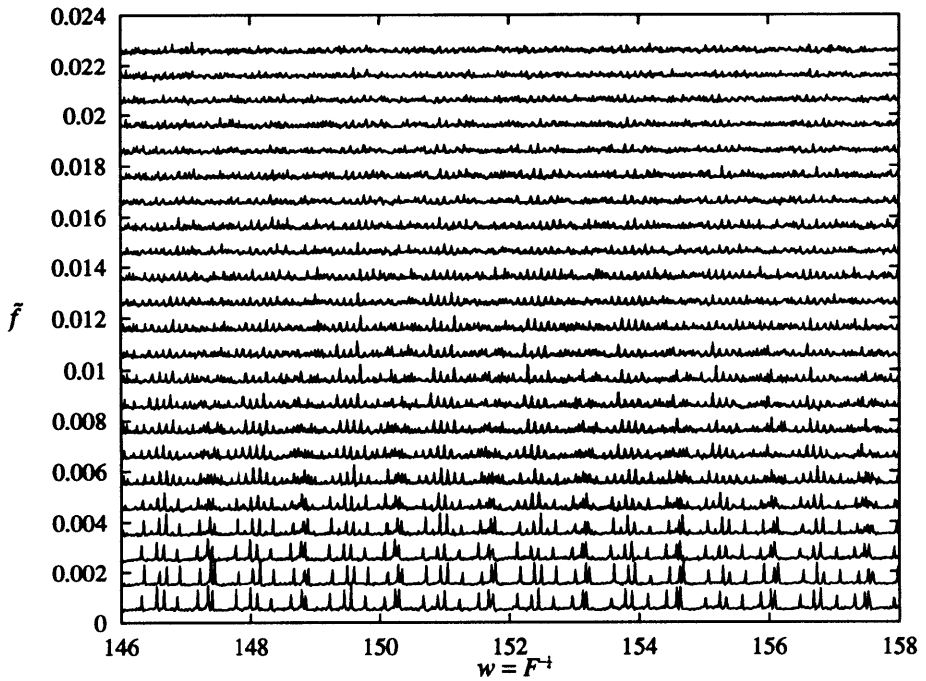

Figure 6-14: Untransformed experimental spectra, $\epsilon = -0.4$, $\tilde{\omega} = 0.32$, $0.0 \leq \tilde{f} \leq 0.022$. Each scan is offset from its baseline value due to a large continuum background.

Figure 6-3 reveals that many of the orbits do not contribute to the spectrum as $\tilde{f}$ becomes large. Indeed, there are just three sets of contributing orbits: the second repetition, a group centered on the 14th repetition, and a group centered on the 27th repetition. The uphill orbits U_k with action $\tilde{S} = 0.69k$ contribute periodicities at wavelengths $\Delta w = 1/\tilde{S} = 1/(0.69k)$, where k is the repetition number. The second repetition contributes to the spectrum with a wavelength of $\Delta w = 0.72$. The 14th repetition contributes with a wavelength $\Delta w = 0.1$, so it is related to the evenly spaced peaks. The 27th repetition contributes with a wavelength $\Delta w = 0.053$. It is the source of the very narrow lines in the figure. As $\tilde{f}$ becomes increasingly strong, all of the orbits lose strength and the spectrum evolves into a uniform continuum. A subject for further experimental study would be to perform detailed high-resolution measurements of the positions and widths of the states as ionization effects develop. This would be the energy-domain equivalent to time-domain microwave-ionization experiments. It is unclear whether anything new would be learned.

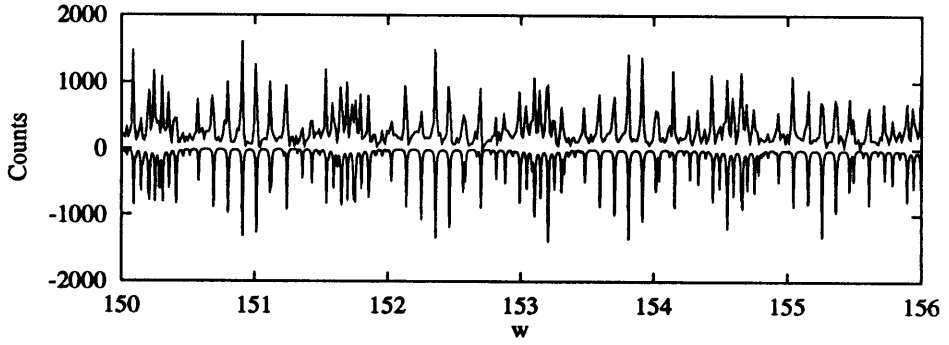

Figure 6-15: Untransformed experimental and computed spectra, $\epsilon = -0.4$, $\tilde{\omega} = 0.32$, $\tilde{f} = 0.005$. Top: experiment. Bottom: Floquet computation. A continuum background of 1200 counts is subtracted from the experimental data, which are shifted to the left by 0.04 to account for an offset resulting from a residual stray electric field.

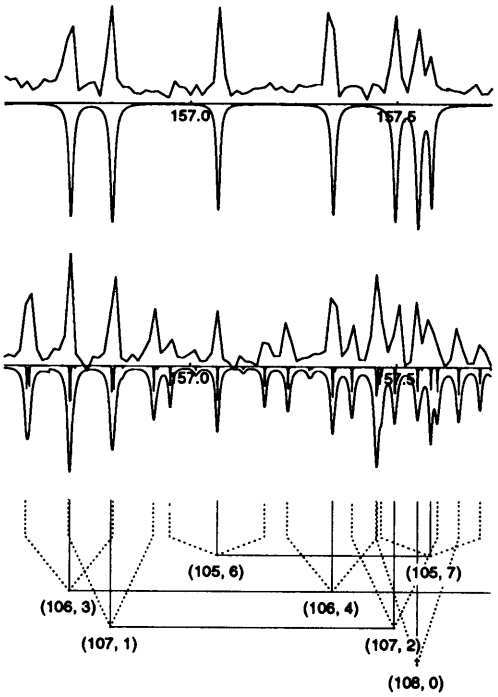

Figure 6-16: Untransformed experimental and computed spectra, plotted as a function of w. (Figure courtesy of Vladimir Kondratovich). The inverted spectrum is the computation. The upper spectrum is at $\tilde{f} = 0.0$; the lower spectrum is at $\tilde{f} = 0.005$. Both are at $\epsilon = -0.4$ and $\tilde{\omega} = 0.32$. The solid vertical lines on the bottom mark the positions of Stark states. The dotted lines indicate the positions of rf sidebands. The pairs (n_1, n_2) are the parabolic quantum numbers of the states.

6.1.5 High-Frequency Behavior of AC Dipole Moment

We learned in Sec. 6.1.2 that at low applied frequencies $|\tilde{Z}_k(\tilde{\omega})|$ is zero when the period of the uphill orbit U_k is an integer multiple of the period of the field. Here we examine the ac dipole moment of these orbits at frequencies up to and above the orbital frequency of the fundamental, U_1. We will learn that when the period of the applied field equals the period of U_1, all the repetitions U_k are strongly perturbed by the field.

Figure 6-17 shows $|\tilde{Z}_k(\tilde{\omega})|$ computed for the uphill orbit U_k as a function of $\tilde{\omega}$ and repetition number k using the method demonstrated in Sec. 2.4. Figure 6-18 shows slices through $|\tilde{Z}_k(\omega)|$ for several repetitions k with the computation extended to $\tilde{\omega} = 10$. The frequency of U_1 is $\tilde{\omega}_0 = 2\pi/\tilde{T} = 4.65$. An examination of the results for $k = 1$ and $k = 2$ reveals that $|\tilde{Z}_k(\tilde{\omega})|$ varies slowly as a function of $\tilde{\omega}$ for low repetition numbers. As the repetition number increases, $|\tilde{Z}_k(0)|$ and $|\tilde{Z}_k(\tilde{\omega}_0)|$ increase in a manner that appears linear in k in Fig. 6-17. This agrees with Eq. (6.2), which predicts that $|\tilde{Z}_k(m\tilde{\omega}_0)| = k|\tilde{Z}_1(m\tilde{\omega}_0)|$, where m is an integer. Furthermore, between 0 and $\tilde{\omega}_0$, $|\tilde{Z}_k(\tilde{\omega})|$ shows small local maxima spaced by nodes in Fig. 6-18. The number of nodes is one less than the repetition number of the orbit.

An examination of the result for $k = 15$ in Fig. 6-18 shows that as $\tilde{\omega}$ increases above $\tilde{\omega}_0$, $|\tilde{Z}_k|$ again decreases, until reaching another maximum at $\tilde{\omega} = 2\tilde{\omega}_0$. Resonant-like behavior in $|\tilde{Z}_k|$ can be seen at $\tilde{\omega} = \tilde{\omega}_0$ and $\tilde{\omega} = 2\tilde{\omega}_0$: as k increases, $|\tilde{Z}_k|$ narrows and increases in height. We now see that the general behavior of an orbit exposed to an oscillating field is to interact strongly with it when the frequency of the field is a multiple of the orbital frequency.

As the frequency increases more, $|\tilde{Z}_k(\tilde{\omega} = m\tilde{\omega}_0)|$ slowly decreases. As discussed in Chapter 7, $\tilde{Z}(\tilde{\omega})$ is the Fourier transform of the $z(t)$ motion of an orbit. Because the parallel orbit has high-frequency components resulting from sharp reflections off the Coulomb potential, these maxima at multiples of the orbital frequency extend to frequencies much higher than shown in the figures.

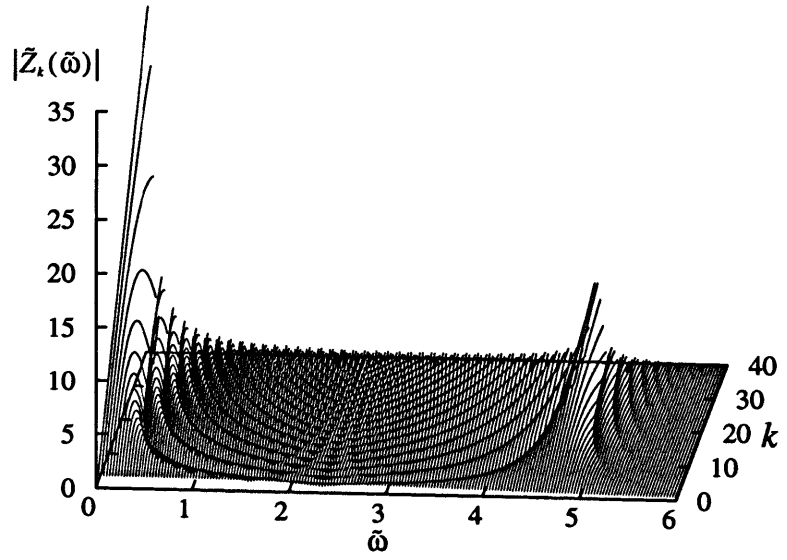

Figure 6-17: AC dipole moment of the uphill orbit U_k vs. $\tilde{\omega}$ and repetition number k at $\epsilon = -0.4$. Although $|\tilde{Z}(\tilde{\omega})|$ is plotted as a continuous function, it is defined only discretely at each repetition.

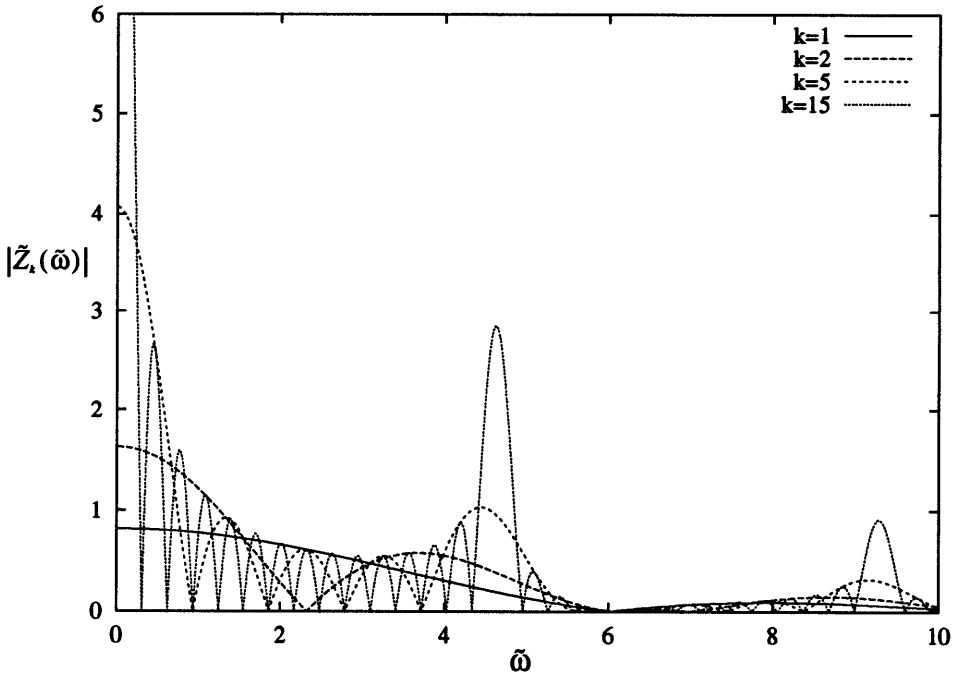

Figure 6-18: AC dipole moment for several repetitions of the uphill parallel orbit, U_k. The 15th repetition extends off scale to $|\tilde{Z}_{15}(0)| = 12.21$.

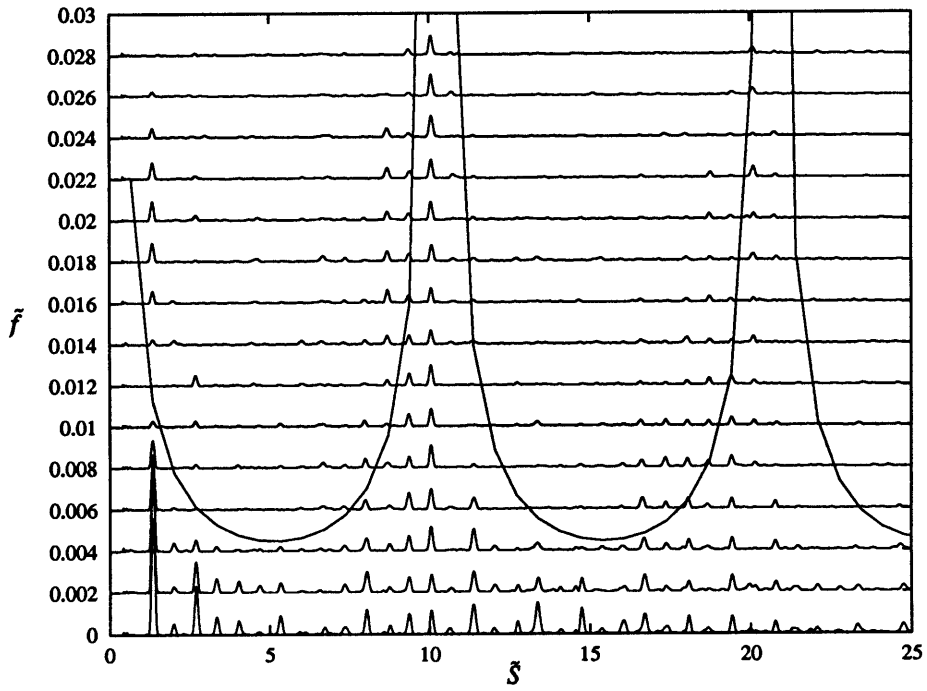

Figure 6-19: Experimental recurrence spectra, $\epsilon = -0.5$, $\tilde{\omega} = 0.32$. $144.5 < w < 154.3$. The solid lines mark the positions of the first zero in the recurrence strength as predicted by closed orbit theory restricted to the uphill parallel orbit.

6.2 Recurrence Spectra at $\epsilon = -0.5$

Data were also collected at $\epsilon = -0.5$ as an additional test of theory. Figure 6-19 shows experimental recurrence spectra measured at $\tilde{\omega} = 0.32$ as $\tilde{f}$ is varied from 0 to 0.028. There are no fundamental differences in the system at this energy compared with $\epsilon = -0.4$, except that the 1/2 bifurcation energy, $\epsilon = -0.397$, is farther away. This means that the 1/2 orbit moves farther off the z axis, and the restricted approximation is less valid than at $\epsilon = -0.4$. The solid curved line in Fig. 6-19 is the location of the first zero of a_k for the uphill orbit. It reveals that the restricted theory gives a good description of the overall structure of the system, although there are a few recurrences in the figure that are not well described. Although the detailed theory has not been applied at this energy, it is expected that it should be just as successful here as it is at $\epsilon = -0.4$.

Figure 6-20 shows the strength of the recurrence at the second repetition, extracted

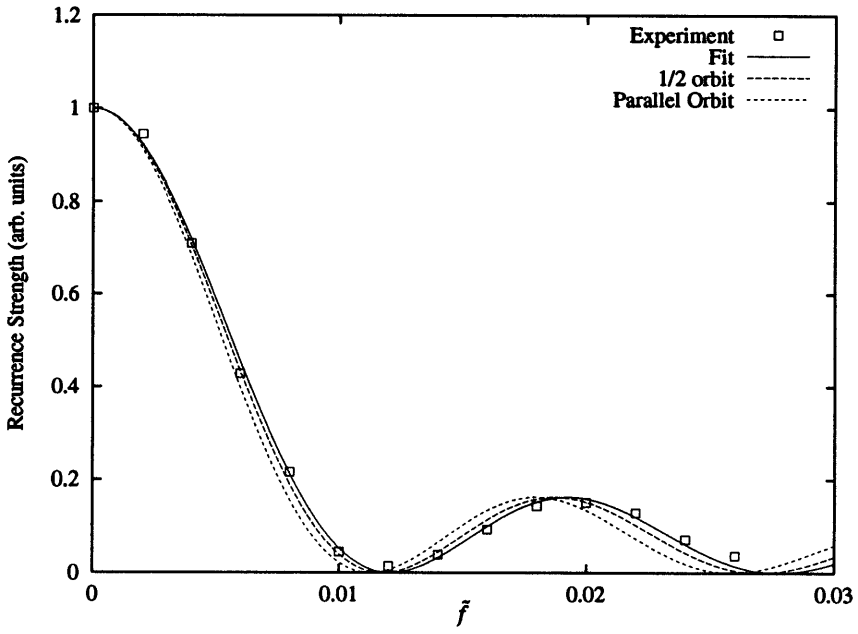

Figure 6-20: Strength of the recurrence at the action of the parallel orbit U_2, $\epsilon = -0.5$, $\tilde{\omega} = 0.32$. Squares are the measurement. The lines are plots of $J_0^2(c_k \tilde{f})$ for a fit to the experiment and for c_k computed for U_2 and the 1/2 orbit.

from Fig. 6-19. The solid line is a fit to a squared Bessel function. The extracted value $|\tilde{Z}(0.32)| = 1.33$ is close to the classical result for the orbit U_2, $|\tilde{Z}_2(0.32)| = 1.43$, and for the 1/2 orbit, $|\tilde{Z}_{1/2}(0.32)| = 1.37$. Recall that these two orbits could not be distinguished by the falloff rate at $\epsilon = -0.4$ because their values of $|\tilde{Z}|$ differed by only a part in a thousand. Here, however, we begin to distinguish their contributions to the recurrence strength. As expected from the proximity of the bifurcation, the 1/2 orbit gives the dominant contribution.

6.3 Computational Results, $\epsilon = -6$

We have seen in the previous sections that the experiment, closed orbit theory, and semiquantal computations provide a consistent description of the behavior of Rydberg atoms in oscillating fields at energies near $\epsilon = -0.4$. In the next chapter, spectra in oscillating fields are examined at energies near the saddle point, $\epsilon = -2$. There are

two other general regions of behavior, $\epsilon > 0$ and $\epsilon \ll -2$. We do not consider the positive energy region in this thesis. At low energies, experimental measurements of recurrence spectra are difficult because lower laser energies and higher rf frequencies, extending into the microwave region, are required. Gathering recurrence spectra is cumbersome at low energies because the classical scaling laws require that the laser must be manually mode-hopped and scanned over more modes than are required to measure a recurrence spectrum with equivalent action resolution at higher energies. For these reasons, experimental spectra for $\epsilon \ll -2$ have not been measured. Although the semiquantal computations described in Sec. 6.1.1 should give a good description of low-energy behavior in hydrogen, they do not treat alkali-metal atoms. In contrast to behavior at high energy, core-scattering is an important effect at low energies. Therefore, we turn to the quantum Floquet method described in Sec. 3.4 to compute recurrence spectra for hydrogen and lithium. We show that computations for hydrogen at $\epsilon = -6$ show good agreement with closed orbit theory before considering lithium at $\epsilon = -4$ in the following sections.

The energy $\epsilon = -6$ was selected because, due to the absence of n-mixing, the matrix to be diagonalized does not need to be excessively large. Additionally, the oscillating field strength is kept below $\tilde{f} = 0.1$ to minimize the number of Floquet sidebands. Up to ten sidebands on each side of each state were needed to produce converged results at $90 \leq w \leq 110$. We begin by discussing the spectrum in a static field.

6.3.1 Static Field Recurrence Spectra

Figure 6-21 shows hydrogen recurrence spectra at $\epsilon = -6$. There are strong recurrences for $\tilde{S} < 2$ and $12 < \tilde{S} < 17$. The uphill and downhill orbits have similar actions, $\tilde{S}_u = 0.2858$ and $\tilde{S}_d = 0.2918$, and similar periods, $\tilde{T}_u = 0.1435$ and $\tilde{T}_d = 0.1594$. The actions of repetitions of these orbits are indicated by arrows along the bottom of the figure. Strong recurrences are located where the action of a repetition of the uphill orbit equals that of some repetition of the downhill orbit. This is a consequence of the fact that orbits have a larger overlap with the nucleus under these circumstances,

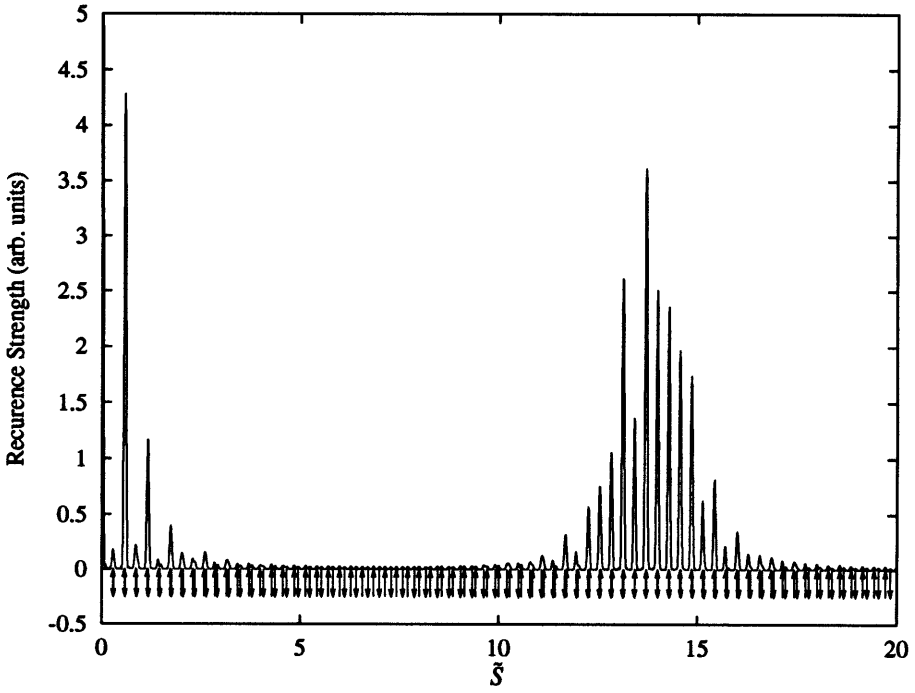

Figure 6-21: Computed recurrence spectra, hydrogen, $\epsilon = -6$. $90 \leq w \leq 110$. Down-pointing arrows mark the action of the downhill orbit. Up-pointing arrows mark the action of the uphill orbit.

as described in Sec. 2.5. Recurrences are weak where the actions of the uphill and downhill orbits are separated. While these weak regions would be difficult to study experimentally because of experimental noise, they are easily studied with computed recurrence spectra, which are noise free. For an examination of behavior in an oscillating field, the isolated orbits simplify comparison with closed orbit theory because they are composed of a single orbit.

6.3.2 Oscillating Field Recurrence Spectra

Figure 6-22 shows computed recurrence spectra in an oscillating field with frequency $\tilde{\omega} = 1.0$ and amplitude up to $\tilde{f} = 0.1$. The Floquet computations use a maximum of $q_{\max} = 10$ sidebands. The applied frequency is in the adiabatic regime, for the frequency of uphill motion at this energy is $\tilde{\omega}_0 = 43.8$. The strong recurrences from Fig. 6-21 interact weakly with the oscillating field, while the weak recurrences show a significant decrease in strength as $\tilde{f}$ increases.

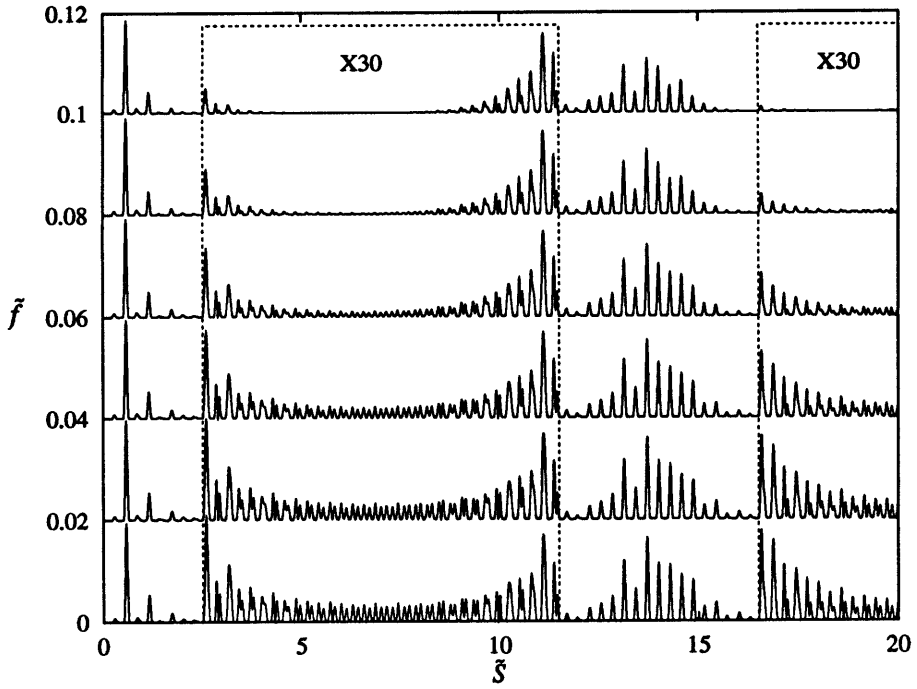

Figure 6-22: Computed recurrence spectra, hydrogen, $\epsilon = -6$, $\tilde{\omega} = 1.0$, $\tilde{f} \leq 0.1$. $90 \leq w \leq 110$. The region within the dashed boxes is scaled by a factor of 30.

Figure 6-23 shows the results of a classical computation of the ac dipole moments $|\tilde{Z}_k(1.0)|$ for the uphill and downhill orbits. Comparison with Fig. 6-22 reveals that the weak recurrences have large values of $|\tilde{Z}_k|$, while the strong recurrences have small values. This is consistent with the observation from Fig. 6-22 that the weak recurrences are affected by the oscillating field more strongly than the strong recurrences. Values for the falloff coefficients c_k, extracted from the computations by fitting to Eq. (6.3), are compared with classical values of $|\tilde{Z}_k(1.0)|$ for repetitions of the uphill and downhill orbits in Tables 6.2 and 6.3, respectively. Values are given only for some isolated recurrences, for the strong recurrences contain both uphill and downhill orbits which obscure the analysis. The results agree with the classical values to about 2%.

We have now shown that we have a computational method that generates recurrence spectra that are consistent with closed orbit theory at low energies and weak oscillating field strengths. Before examining results for lithium, we develop a theo-

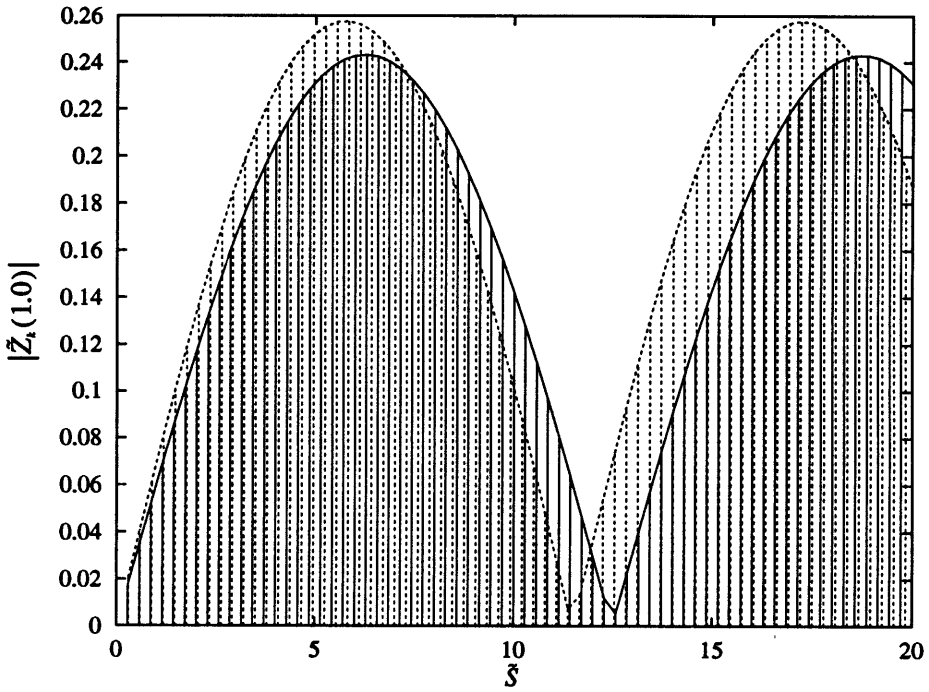

Figure 6-23: Classical computation of ac dipole moments $|\tilde{Z}_k(\tilde{\omega})|$ at $\epsilon = -6$ and $\tilde{\omega} = 1.0$. Solid lines: uphill orbits U_k; dashed lines: downhill orbits D_k. The values are plotted with impulses because $|\tilde{Z}_k|$ is defined only for discrete values of the action. Note that large values of $|\tilde{Z}_k|$ here correspond to the recurrences in Fig. 6-22 that are strongly perturbed by the oscillating field.

Repetition, k	$\left\|\tilde{Z}_k(\tilde{\omega}=1.0)\right\|$	c_k
10	0.1602	15.70
12	0.1848	18.35
13	0.1957	19.43
15	0.2143	21.30
20	0.2411	24.05
25	0.2370	24.10
30	0.2026	20.00
40	0.0638	6.118
60	0.2242	22.10
80	0.1231	11.37
120	0.1738	17.82

Table 6.2: Comparison between classical ac dipole moments, $|\tilde{Z}_k(\tilde{\omega})|$, and the falloff coefficient c_k extracted from computed hydrogen spectra at $\epsilon = -6$ and $\tilde{\omega} = 1.0$. Values for several easily studied repetitions k of the uphill orbit are given. Because $\overline{w} = 100$ for the computations, closed orbit theory predicts that $c_k = 100 \times |\tilde{Z}_k|$.

Repetition, k	$\left\|\tilde{Z}_k(\tilde{\omega}=1.0)\right\|$	c_k
10	0.1846	18.47
15	0.2400	23.68
20	0.2577	26.01
25	0.2349	23.37
30	0.1751	17.41
66	0.2189	21.68
80	0.0264	2.579
120	0.0396	3.485

Table 6.3: Comparison between classical ac dipole moments, $|\tilde{Z}(\tilde{\omega})|$, and the falloff coefficient c_k extracted from computed hydrogen spectra at $\epsilon = -6$ and $\tilde{\omega} = 1.0$. Values for several easily studied repetitions k of the downhill orbit are given. Because $\overline{w} = 100$ for the computations, closed orbit theory predicts that $c_k = 100 \times |\tilde{Z}_k|$.

retical framework for understanding the interaction of core-scattered orbits with an oscillating field.

6.3.3 Interaction of Core-Scattered Orbits with an Oscillating Field

Because core-scattered orbits can be viewed as combinations of hydrogenic orbits, it is reasonable to expect that they should interact with an oscillating field through their ac dipole moments, in the same way as hydrogenic orbits do. Here we outline the computation of $\tilde{Z}(\tilde{\omega})$ for core-scattered orbits. The computational method developed here is tested in the next section using a core-scattered orbit visible in computed lithium spectra at $\epsilon = -4$.

Consider a core-scattered trajectory composed of three orbits with trajectories $z_k(t)$ along the z axis. The z component of the composite trajectory can be written

$$z(t) = z_1(t) + z_2(t - T_1) + z_3(t - T_1 - T_2), \tag{6.4}$$

where $z_i(t)$ is zero unless $0 < t < T_i$ and T_i is the period of the orbit. From Eq. (2.43), the ac dipole moment is

$$Z(\omega) = Z_1 + Z_2 e^{-i\omega T_1} + Z_3 e^{-i\omega(T_1+T_2)}, \tag{6.5}$$

where Z_k is the ac dipole moment of the trajectory $z_k(t)$. The predicted falloff rate for the core-scattered orbit can then be found from the magnitude of Z. For $z_3(t) = 0$, $|Z|$ satisfies

$$|Z|^2 = |Z_1|^2 + |Z_2|^2 + 2\mathrm{Re}(Z_1 Z_2^* e^{i\omega T_1}). \tag{6.6}$$

In general, $|Z|$ depends on the order of the component trajectories. In principle, the application of the oscillating field could reveal this order. A simple illustration of this is at $\epsilon = -4$ and $\tilde{\omega} = 1.0$. Consider the (hypothetical) case of a core-scattered orbit composed of two repetitions of the uphill orbit U_1 and one repetition of the downhill orbit D_1. Because these three different core-scattered orbits have the same

action, they would be indistinguishable in static-field recurrence spectra. However, they have different ac dipole moments: the orders $U_1+U_1+D_1$ and $D_1+U_1+U_1$ have $|\tilde{Z}| = 3.84 \times 10^{-2}$ while the order $U_1 + D_1 + U_1$ has $|\tilde{Z}| = 2.09 \times 10^{-2}$. By examining the reduction in recurrence strength as an oscillating field is turned on, it should be possible to distinguish the orbit $U_1 + D_1 + U_1$ from the other two.

6.4 Computational Results, $\epsilon = -4$

To examine the interaction of the oscillating field with core-scattered orbits, computations have been performed at $\epsilon = -4$. At lower energies near $\epsilon = -6$, core-scattering is so strong that most recurrences have contributions from many core-scattered orbits. Because this complicates the analysis, we have chosen to work at $\epsilon = -4$, where core-scattering is relatively weak but nevertheless present.

6.4.1 Static Field Recurrence Spectra

Figure 6-24 shows hydrogen and lithium recurrence spectra at $\epsilon = -4$. The uphill and downhill orbits have similar actions, $\tilde{S}_u = 0.3459$ and $\tilde{S}_d = 0.3627$. At low action ($\tilde{S} < 10$), hydrogen and lithium have similar spectra. The positions of the peaks are identical within the resolution of the calculation, and there are only small differences in the recurrence strengths. The spectra differ at higher actions, where core-scattering occurs.

The clearest example of a core-scattered orbit is at $\tilde{S} = 14.8486$, indicated with the label (c) in Fig. 6-24. Table 6.4 lists the action, period, initial angle, and ac dipole moment of this core-scattered orbit and its possible components. The combination $D_{19}+U_{23}$, with $\tilde{S} = 14.8476$, is in best agreement with the action of the core-scattered orbit, and is therefore the most likely component. The two component orbits D_{19} and U_{23} are labeled in the figure with (a) and (b), respectively.

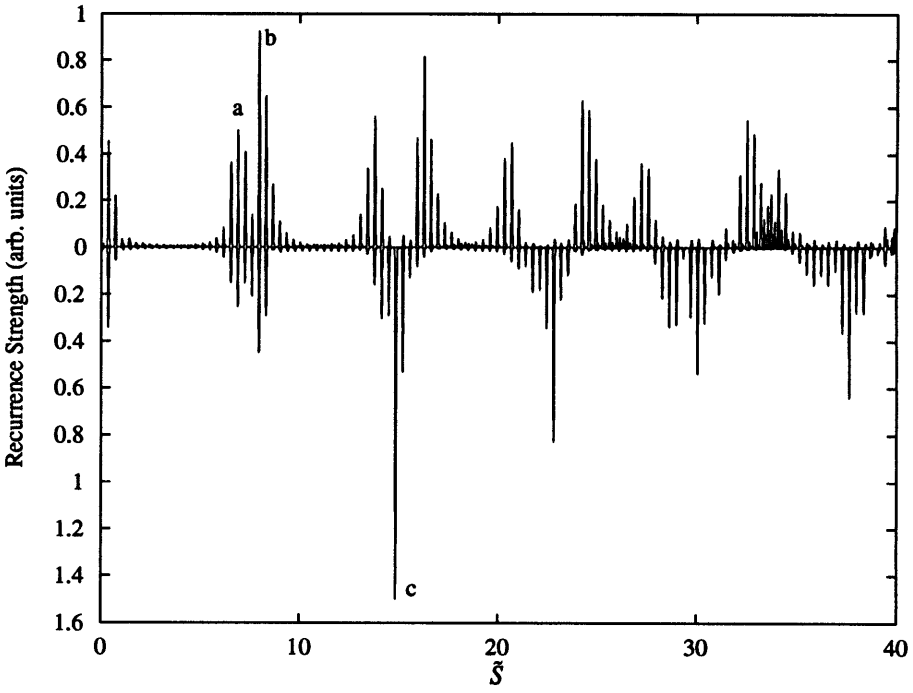

Figure 6-24: Computed recurrence spectra, $\epsilon = -4$, $90 \leq w \leq 110$. Top: hydrogen; bottom: lithium. The label (a) marks the recurrence D_{19}, (b) marks the recurrence U_{23}, and (c) marks the core-scattered recurrence discussed in the text, composed of D_{19} and U_{23}.

Orbit	$\tilde{S}$	$\tilde{T}$	θ_0	$\tilde{Z}(\tilde{\omega} = 1.0)$
U_1	0.3459	0.2496	0	0.0437-i0.0055
U_{22}	7.6104	5.4919	0	-0.1257-i0.0525
U_{23}	7.9563	5.7415	0	-0.0911-i0.0253
U_{24}	8.3024	5.9912	0	-0.0508-i0.0075
D_1	0.3627	0.3168	180	-0.0629+i0.0100
D_{18}	6.5286	5.7019	180	0.1107+i0.0003
D_{19}	6.8913	6.0187	180	0.0526+i0.0070
D_{20}	7.2540	6.3355	180	-0.0107+i0.0331
22/23	7.9542	5.9778	58.7096	-0.0241-i0.0037
19/20	6.8903	5.8324	135.576	0.0650+i0.0149
21/22	7.60304	5.93074	83.8946	-0.000637-i0.000113
23/24	8.30220	6.0236	20.9214	-0.0418-i0.00545
20/21	7.24846	5.8823	107.7504	-0.00588-i0.0296
$D_{19} + U_{23}$	14.8476	11.7602	–	–
$D_{20} + U_{22}$	14.8643	11.8274	–	–
$D_{18} + U_{24}$	14.8308	11.6931	–	–
19/20 + 22/23	14.8445	11.8102	–	–
(c)	14.8486	–	–	–

Table 6.4: Properties of possible constituents of the lithium core-scattered recurrence (c) in Fig. 6-24. These classical values are computed for $\epsilon = -4$. θ_0 is the initial angle of an orbit in degrees. The action listed for (c) is found from Fig. 6-24. It is in best agreement with the action of the combination $D_{19} + U_{23}$.

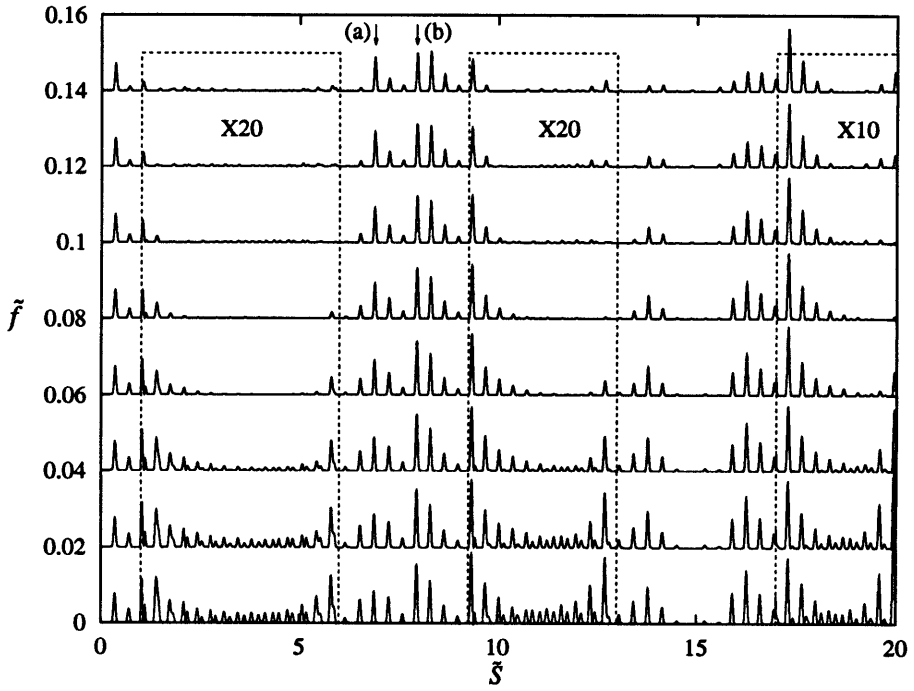

Figure 6-25: Computed recurrence spectra, hydrogen, $\epsilon = -4$, $\tilde{\omega} = 1.0$. $90 \leq w \leq 110$. The spectra within the dashed boxes are scaled by a factor 10 or 20, as indicated. The recurrences labeled (a) and (b) are discussed in the text.

6.4.2 Oscillating Field Recurrence Spectra

Figure 6-25 displays the effect of the oscillating field on hydrogen recurrence spectra at $\epsilon = -4$. The effects are much the same as at $\epsilon = -6$. Analysis reveals agreement similar to that at $\epsilon = -6$ between classical computations of $|\tilde{Z}_k|$ and falloff coefficients extracted from the spectra. Figure 6-26 displays the effect of the oscillating field on lithium recurrence spectra in the same region. A fit to the recurrence strength of the core-scattered orbit (c) gives $|\tilde{Z}(1.0)| = 0.081$. Table 6.5 gives the ac dipole moment for several combinations of hydrogenic orbits using their properties listed in Table 6.4 and the method described in Sec. 6.3.3. These disagree with the result from the lithium quantum computation for the core-scattered orbit (c) by close to a factor of two. It is unknown if the disagreement results from problems with the quantum computation or theory. More study is needed.

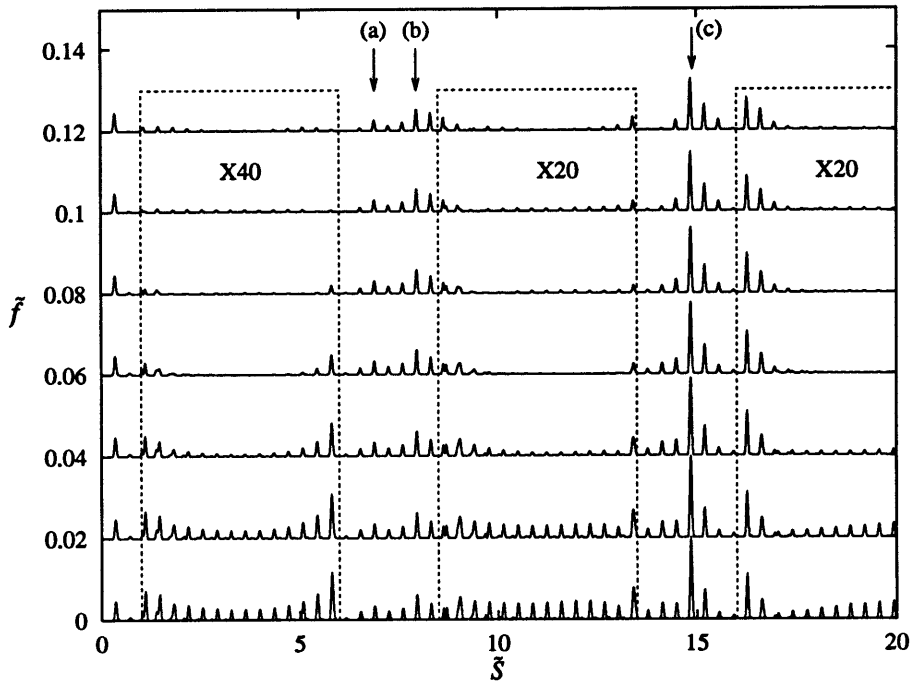

Figure 6-26: Computed recurrence spectra, lithium, $\epsilon = -4$, $\tilde{\omega} = 1.0$. $90 \leq w \leq 110$. The spectra within the dashed boxes are scaled by a factor 20 or 40, as indicated. The labels (a), (b), and (c) are defined in Fig. 6-24.

Combination	$\left\|\tilde{Z}(\tilde{\omega} = 1.0)\right\|$
$D_{19} + U_{23}$	5.02×10^{-2}
$19/20 + 22/23$	4.49×10^{-2}
$D_{19} + 22/23$	3.05×10^{-2}
$19/20 + U_{23}$	4.79×10^{-2}
(c)	8.1×10^{-2}

Table 6.5: Computed ac dipole moments for possible constituents of the core-scattered recurrence (c) in Fig. 6-24. The value given for (c) is found from a fit to the data in Fig. 6-25.

Chapter 7

Quantum Measurement of a Classical Trajectory

The previous chapters have shown that recurrence spectra measured in an oscillating field yield the magnitude of the ac dipole moment $\tilde{Z}_k(\tilde{\omega})$ of the classical trajectory of a closed orbit along the direction of an oscillating electric field, at the frequency of the field. Because $\tilde{Z}_k(\tilde{\omega})$ is the Fourier transform of the classical trajectory $z_k(t)$, measurements of $|\tilde{Z}_k(\tilde{\omega})|$ over a finite range of frequencies can be inverted to give a finite-resolution reconstruction of the trajectory. This represents a fundamental advance in semiclassical techniques. Previously, information that could be learned about an orbit from recurrence spectra was limited to its existence, action, period, and stability. In this chapter we describe the details of a measurement of the trajectories of the 2/3 and 3/4 orbits, and discuss the promise of the method as a general technique for measuring classical trajectories from quantum spectra.

7.1 Experimental Measurements

We demonstrate the method using the 2/3 and 3/4 orbits at $\epsilon = -2.05$. Their trajectories are shown in Fig. 7-1 and some of their properties are listed in Table 7.1. These orbits are well suited to the measurement because their motion is simple but not trivial and they are experimentally accessible over a range of frequencies large enough

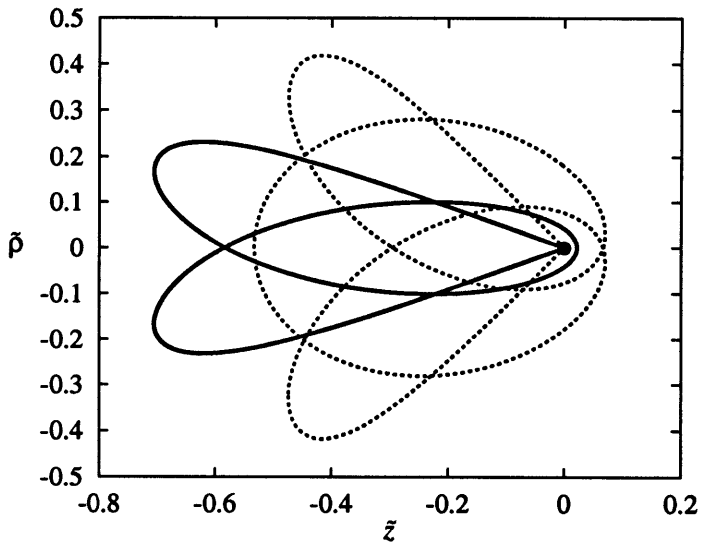

Figure 7-1: Classical trajectories of the 2/3 (solid line) and 3/4 (dotted line) orbits, $\epsilon = -2.05$.

Orbit	$\tilde{S}$	$\tilde{T}$	θ_0
2/3	1.151	3.719	155.5
3/4	1.700	3.914	128.2
D_2	1.153	4.546	180
D_3	1.730	6.820	180

Table 7.1: Action $\tilde{S}$, period $\tilde{T}$, and initial angle θ_0 (degrees) for several orbits which are important in the reconstruction at $\epsilon = -2.05$.

to extract meaningful results. We showed in Sec. 5.2 that the recurrence strengths of these orbits at $\epsilon = -2.05$ are larger than those of the corresponding repetitions of the downhill orbits D_2 and D_3, whose actions are nearly indistinguishable from the 2/3 and 3/4 orbits, respectively. The 2/3 recurrence is near its maximum strength at this energy, whereas the 3/4 recurrence is past its maximum. The ac dipole moments for the 2/3 and 3/4 orbits were measured at 17 frequencies between $\tilde{\omega} = 0.6$ and $\tilde{\omega} = 4.0$. Figure 7-2 shows a typical data set, revealing the effect of an oscillating field on the recurrence strength of the orbits. The frequency is $\tilde{\omega} = 1.4$. The recurrence strength falls off as predicted by Eq. (2.51), $J_0^2(c_k \tilde{f})$. $|\tilde{Z}_k(\tilde{\omega})|$ is extracted by fitting the data

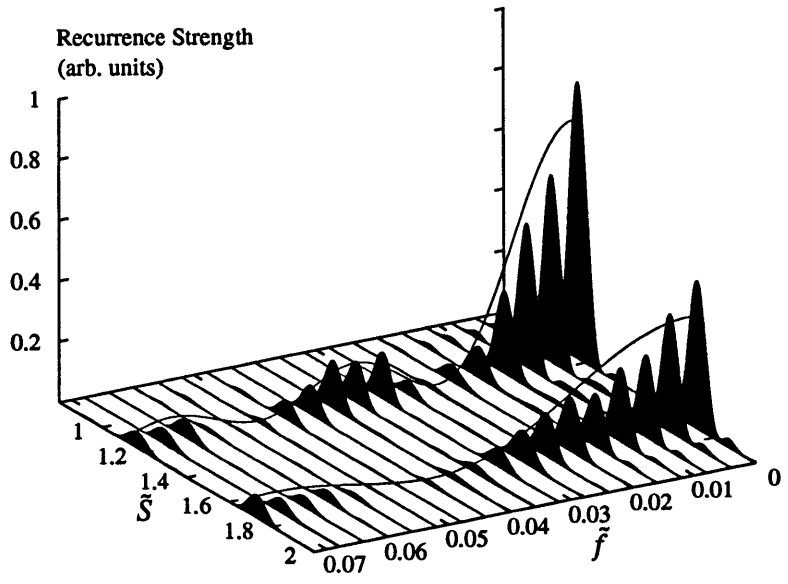

Figure 7-2: Experimental recurrence spectra, $\tilde{\omega} = 1.4$, $\epsilon = -2.05$. The two peaks are at the action of the 2/3 ($\tilde{S} = 1.15$) and 3/4 ($\tilde{S} = 1.70$) orbits. The solid lines are fits to a squared Bessel function, Eq. (2.51). The fits yield $|\tilde{Z}_{2/3}(1.4)| = 0.417$ and $|\tilde{Z}_{3/4}(1.4)| = 0.221$. (The classical values are $|\tilde{Z}_{2/3}(1.4)| = 0.437$ and $|\tilde{Z}_{3/4}(1.4)| = 0.219$.) These data were recorded from $w = 248.8$ to $w = 260.6$.

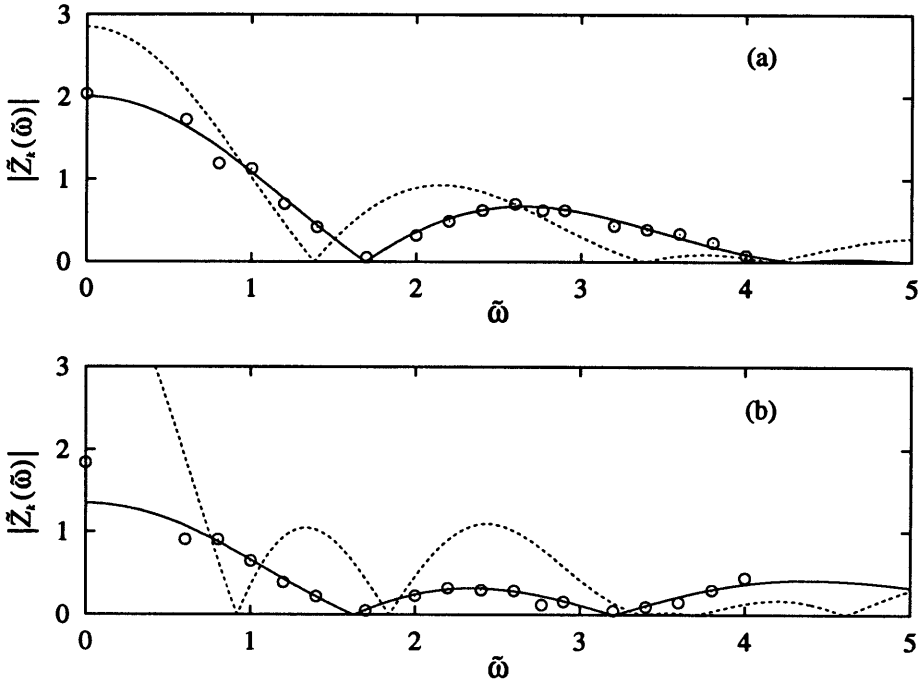

Figure 7-3: Experimental measurement of $|\tilde{Z}_k(\tilde{\omega})|$ for (a) 2/3 and (b) 3/4 orbits, $0.6 \leq \tilde{\omega} \leq 4.0$, $\epsilon = -2.05$. The circles are the experimental measurements and the solid lines are the classical values. To verify that these orbits are not downhill orbits, the dashed line shows $|\tilde{Z}_k(\tilde{\omega})|$ calculated for the downhill orbits (a) D_2 and (b) D_3. The points at $\tilde{\omega} = 0$ are found from Eq. (7.1).

to the predicted form as described in Chapter 6. The fits yield $|\tilde{Z}_{2/3}(1.4)| = 0.417$ and $|\tilde{Z}_{3/4}(1.4)| = 0.221$. These values are in good agreement with the classical values, $|\tilde{Z}_{2/3}(1.4)| = 0.437$ and $|\tilde{Z}_{3/4}(1.4)| = 0.219$.

Figure 7-3 shows the results of fits to measurements for frequencies between $\tilde{\omega} = 0.6$ and $\tilde{\omega} = 4.0$. The experimental values are in good agreement with the results of exact classical calculations also shown in the figure. Should there be any doubt that these are not downhill orbits, the results are clearly inconsistent with the values of $|\tilde{Z}_k(\tilde{\omega})|$ computed for the downhill orbits D_2 and D_3, also shown in Fig. 7-3. This provides strong support for the conclusion in Sec. 5.2 that the strengths of these recurrences are dominated by the 2/3 and 3/4 orbits.

To measure $|\tilde{Z}_k(\tilde{\omega})|$ accurately, it is desirable to choose a step size $\Delta\tilde{f}$ between scans small enough to provide five or six scans before reaching the first minimum of

the Bessel function. When the measurements were made the primary interest was in the 2/3 orbit, with only secondary consideration given to the 3/4 orbit. Therefore, at some frequencies the strength of the 3/4 orbit was measured with only a few steps in $\tilde{f}$ before its first minimum. Furthermore, because the 3/4 orbit is a weak recurrence, the measurement of its strength is relatively susceptible to noise. For these reasons, the experimental values of $|\tilde{Z}_{3/4}(\tilde{\omega})|$ are somewhat less accurate than those of $|\tilde{Z}_{2/3}(\tilde{\omega})|$. Nevertheless, the results for both orbits merit study.

The original motivation for examining this region was to study the downhill orbit at energies close to the saddle point, $\epsilon = -2$. For energies sufficiently close to the saddle point, the downhill orbit ionizes for phases of the field that lower the saddle point, while it is more stable for other phases that raise the saddle point. However, the importance of the 2/3 and 3/4 orbits was not understood until the oscillating field was applied and disagreement with the predicted classical behavior of the downhill orbit was observed. The original problem remains interesting, but needs to be studied in a region (perhaps at higher action) where the downhill orbit is clearly visible.

The lowest measured frequency was $\tilde{\omega} = 0.6$. While frequencies $\tilde{\omega} < 0.6$ affect the overall structure of the orbit, they do not determine fine details. For example, the $\tilde{\omega} = 0$ component, $\tilde{Z}_k(\tilde{0})$, is just a DC offset to the trajectory. Fortunately, we have two methods that determine the low-frequency components of $\tilde{Z}_k(\tilde{\omega})$. The first method, which we describe here, gives $\tilde{Z}_k(\tilde{\omega} = 0)$. The second, described in Sec. 7.3, incorporates approximate knowledge of the period to find low-frequency values of $\tilde{Z}_k(\tilde{\omega})$ in a fit to the data.

The static dipole moment of an orbit, $\tilde{Z}_k(\tilde{\omega} = 0)$, is a real quantity related to the action and period of the orbit by

$$\tilde{Z}_k(\tilde{\omega} = 0) = \frac{1}{2}\tilde{T}\epsilon + \frac{2\pi\tilde{S}_k}{4} . \tag{7.1}$$

This relation is found [Hag] using Eq. (2.36), this time to find the perturbation to

the action caused by the *static* field:

$$\frac{\partial S_k}{\partial F} = -\int_0^{T_k} \frac{\partial H}{\partial F} dt = -\int_0^{T_k} z_k(t) dt = -Z_k(\omega = 0). \tag{7.2}$$

This relation is expressed in unscaled coordinates. One arrives at Eq. (7.1) by expressing the derivative $\partial S/\partial F$ in scaled variables through the relationship

$$S = S(E, F) = 2\pi \tilde{S}(\epsilon) F^{-1/4}. \tag{7.3}$$

We evaluate Eq. (7.1) using experimentally measured quantities. The action is easily measured with a single recurrence spectrum. The experimental measurement of periods is discussed in Sec. 5.2. At $\epsilon = -2.05$, for the 2/3 orbit the experimental values $\tilde{S}_{2/3} = 1.15$ and $\tilde{T}_{2/3} = 3.75$ give $\tilde{Z}_{2/3}(0) = -2.04$. The exact classical value is $\tilde{Z}_{2/3}(0) = -2.004$. For the 3/4 orbit, the values $\tilde{S}_{3/4} = 1.70$ and $\tilde{T}_{3/4} = 4.4$ give $\tilde{Z}_{3/4}(0) = -1.84$. The classical value is $\tilde{Z}_{3/4}(0) = -1.341$. The agreement with theory for the 2/3 orbit is good. The discrepancy for the 3/4 orbit reflects the poor experimental measurement of $\tilde{T}_{3/4}$.

7.2 Determining the Phase

Measurement in the oscillating field yields values for $|\tilde{Z}_k(\tilde{\omega})|$. However, $\tilde{Z}_k(\tilde{\omega})$ is a complex function, and information about its phase is required to invert the Fourier transform. Fortunately, because the trajectories in an electric field are time-reversal symmetric, there is a method for extracting this phase. The argument is as follows [Hag]. The ac dipole moment of an orbit $z_k(t)$ is[1]

$$Z_k(\omega) = \int_0^{T_k} z_k(t) e^{-i\omega t} dt. \tag{7.4}$$

[1]We use unscaled variables for notational simplicity in the remainder of the chapter. The equations have identical forms in scaled variables.

This can be written

$$Z_k(\omega) = e^{-i\omega T_k/2}\left\{\int_0^{T_k} z_k(t)e^{-i\omega(t-T_k/2)}dt\right\} \quad (7.5)$$

$$= e^{-i\omega T_k/2}\left\{\int_{-T_k/2}^{T_k/2} z_k(T_k/2+t')e^{-i\omega t'}dt'\right\}. \quad (7.6)$$

Because of the time-reversal symmetry, $z_k(T_k/2+t')$ is an even function of t'. Because the Fourier transform of an even function is even and real, $Z_k(\omega)$ can be expressed as

$$Z_k(\omega) = e^{-i\omega T_k/2}Z_k^R(\omega), \quad (7.7)$$

where $Z_k^R(\omega)$ is an even, real function. Because it is the finite-time Fourier transform of a well-behaved function, $Z_k^R(\omega)$ is smooth and continuous.

The real function $Z_k^R(\omega)$ is found from $|Z_k(\omega)|$ as follows. The sign of $Z_k^R(\omega)$ at $\omega = 0$ is fixed using the value given by Eq. (7.1). Note that the accuracy of this value is not critical because only its sign is needed. This is important because the period is difficult to measure accurately. Values of $Z_k^R(\omega)$ for higher-frequency points are found from the requirement that $Z_k^R(\omega)$ be smooth and continuous. This criterion removes the "kinks" in the measured function at a zero-crossing like the one visible for the 2/3 orbit in Fig. 7-3 at $\tilde{\omega} = 1.6$. The resulting values of $Z_k^R(\omega)$ are shown in Fig. 7-6, which will be discussed in more detail later. We are now ready to invert Eq. (7.4) to find the trajectory $z_k(t)$.

7.3 Extracting the Trajectory

We use two methods to find $z_k(t)$ by inverting Eq. (7.4). The first method directly evaluates the inverse Fourier transform from the values of $Z_k^R(\omega)$ found directly from the experimental data, while the second method performs the inversion using a least squares fit to the data using a set of functions that form a basis for $Z_k^R(\omega)$. The latter method is well suited for dealing with noise in experimental data and for data collected over limited frequency ranges. The former method, which we now describe,

is simple and illustrative.

The measured trajectory $z_k(t)$ is derived from the ac dipole moment using the relation

$$z_k(t) = \frac{1}{2\pi}\int_{-\omega_{\max}}^{\omega_{\max}} Z_k(\omega)e^{i\omega t}d\omega, \tag{7.8}$$

where $\omega_{\max}$ is the maximum measured frequency. Although this inverse transform includes $\omega < 0$ terms, the symmetry of $z_k(t)$ guarantees that these are trivially related to the $\omega > 0$ terms. From Eq. (7.7), $Z_k^*(\omega) = Z_k(-\omega)$, from which it follows that

$$\begin{aligned} z_k(t) &= \frac{1}{2\pi}\int_0^{\omega_{\max}} \left(Z_k(\omega)e^{i\omega t} + Z_k^*(\omega)e^{-i\omega t}\right) d\omega & (7.9)\\ &= \frac{1}{2\pi}\int_0^{\omega_{\max}} Z_k^R(\omega)\left(e^{i\omega(t-T_k/2)} + e^{-i\omega(t-T_k/2)}\right) d\omega & (7.10)\\ &= \frac{1}{\pi}\int_0^{\omega_{\max}} Z_k^R(\omega)\cos[\omega(t-T_k/2)]d\omega. & (7.11) \end{aligned}$$

It is unfortunate that the period T_k appears explicitly in Eq. (7.11) because T_k is difficult to measure experimentally. We can avoid this problem by finding the function $z_k(t+T_k/2)$ rather than $z_k(t)$. From Eq. (7.11),

$$z_k(t+T_k/2) = \frac{1}{\pi}\int_0^{\omega_{\max}} Z_k^R(\omega)\cos(\omega t)d\omega. \tag{7.12}$$

The trajectory is found as follows. A cubic-spline interpolation to the measured values of $Z_k^R(\omega)$ shown in Fig. 7-6 provides values of $Z_k^R(\omega)$ on a grid of points on which Eq. (7.12), approximated by a finite discrete sum, is evaluated. The results of this method, applied to the 2/3 and 3/4 orbits, are shown in Fig. 7-4. Note that the reconstructed trajectories are symmetric because the time-reversal symmetry of the orbits has been built into the calculations. The trajectories are centered about $t = 0$ with no beginning or end specified because exact knowledge of the periods T_k is not used.

Because of the limited frequency range of the reconstruction, large differences between the exact trajectories and the reconstructions are apparent, particularly for the 3/4 orbit. These differences occur because the experimental frequency range is

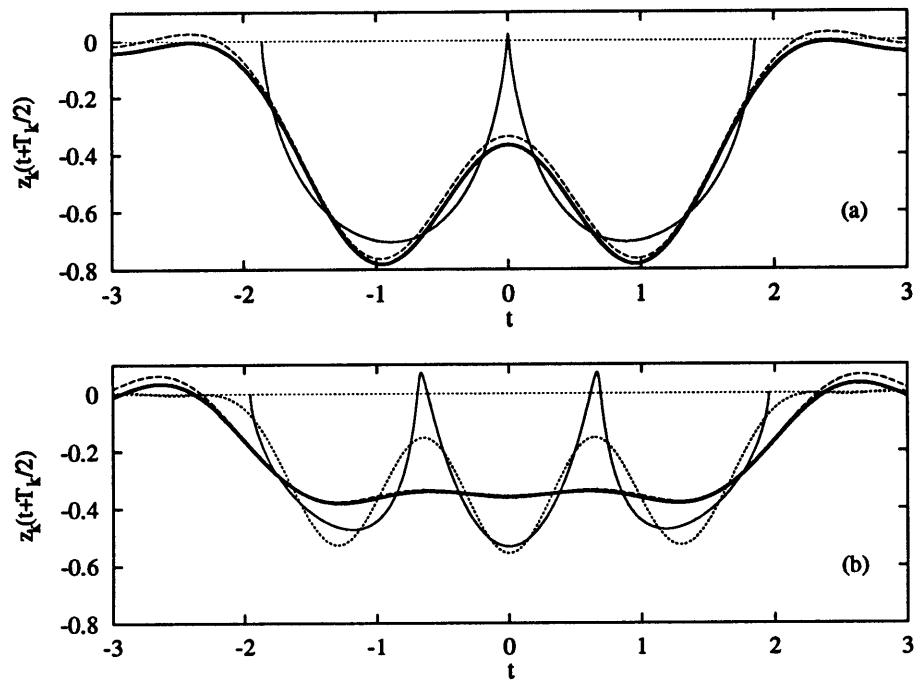

Figure 7-4: Reconstruction of $z_k(t + T_k/2)$ for (a) 2/3 and (b) 3/4 orbits at $\epsilon = -2.05$ using direct inversion. The light solid line is the exact classical trajectory. The heavy solid line is the experimental reconstruction. The dashed line (barely visible near the heavy solid line) is the reconstruction generated using the exact classical values over the experimental window of $0 \leq \tilde{\omega} \leq 4.0$. The fine dashed line in (b) (not to be confused with the x axis) is an exact reconstruction with the frequency range extended to $\tilde{\omega} \leq 6.0$. Note the contrast with the basis-function reconstruction, Fig. 7-7.

not sufficient to measure the high-frequency components that are characteristic of the motion of the electron near the nucleus, where it undergoes a sharp bounce. To assess the accuracy of the measurement, we have performed an identical Fourier transform using the exact classical values of $Z_k(\omega)$, windowed to include only the experimental frequency range $\tilde{\omega} \leq 4.0$. All other details of the process are the same. The results, which are also shown in the figure, are in good agreement with the experimental measurement. To illustrate the importance of higher frequencies, the exact windowed inversion for frequencies $\tilde{\omega} \leq 6.0$ is shown for the 3/4 orbit.

The direct inversion of the Fourier transform is less successful at determining the motion of the 3/4 orbit because, as a glance at Fig. 7-3 reveals, $|Z_{3/4}(\omega)|$ remains

larger than $|Z_{2/3}(\omega)|$ for $\tilde{\omega} > 4$. The direct inversion method can be sensitive to the cut-off frequency as well as to errors in the experimental values of $|Z_k(\omega)|$ and the measured period T_k. To alleviate these problems we turn to a more sophisticated method developed by M. Haggerty [Hag]. We outline the method here and discuss the results.

We begin by noting that $z_k(t)$ can be expressed as a discrete Fourier series:

$$z_k(t) = \sum_{n=0}^{\infty} a_n \cos(n\omega_0 t) = \sum_{n=0}^{\infty} \frac{a_n}{2}\left(e^{in\omega_0 t} + e^{-in\omega_0 t}\right) \equiv \sum_{n=0}^{\infty} a_n \phi_n(t), \tag{7.13}$$

where $\omega_0 = 2\pi/T_k$, $z_k(t=0) = z_k(T_k) = 0$, and $z_k(t) = z_k(T_k - t)$. (Only cosine terms are needed because $z_k(t)$ is even.) The functions $\phi_n(t) = \cos(n\omega_0 t)$ form a basis in which the orbital motion is decomposed.

A series expansion for $Z_k(\omega)$ is found from Eq. (7.13) by evaluating the Fourier transform (7.4). The result is

$$Z_k(\omega) = \sum_{n=0}^{\infty} \frac{a_n T_k}{2}(-1)^n e^{-i\omega T_k/2}\Phi_n(\omega) = Z_k^R(\omega)e^{-i\omega T_k/2}, \tag{7.14}$$

where

$$\Phi_n(\omega) = \frac{\sin[(n\omega_0 - \omega)T_k/2]}{(n\omega_0 - \omega)T_k/2} + \frac{\sin[(n\omega_0 + \omega)T_k/2]}{(n\omega_0 + \omega)T_k/2} \tag{7.15}$$

and $Z_k^R(\omega)$ is defined by Eq. (7.7). The time-domain basis functions $\phi_n(t)$ are related by a Fourier transform to the frequency-domain basis functions $\Phi_n(\omega)$, several of which are shown in Fig. 7-5.

Equations (7.4) and (7.14) form the basis of the method of analysis. Values of some number of coefficients a_n can be extracted from a least-squares fit of the basis functions $\Phi_n(\omega)$ to the measured values of $Z_k^R(\omega)$. The coefficients found in the fit can then be used in Eq. (7.13) to find the approximation to $z_k(t)$. This technique makes it possible to extract basis functions $\Phi_n(\omega)$ that have significant amplitude at frequencies higher than the experimental limit. Consider, for example, the $n = 3$ basis function, $\Phi_3(\omega)$, at $\omega = 4.0$. Its value is large enough relative to the $n = 2$ function that a_3 can be determined fairly accurately from the experimental data.

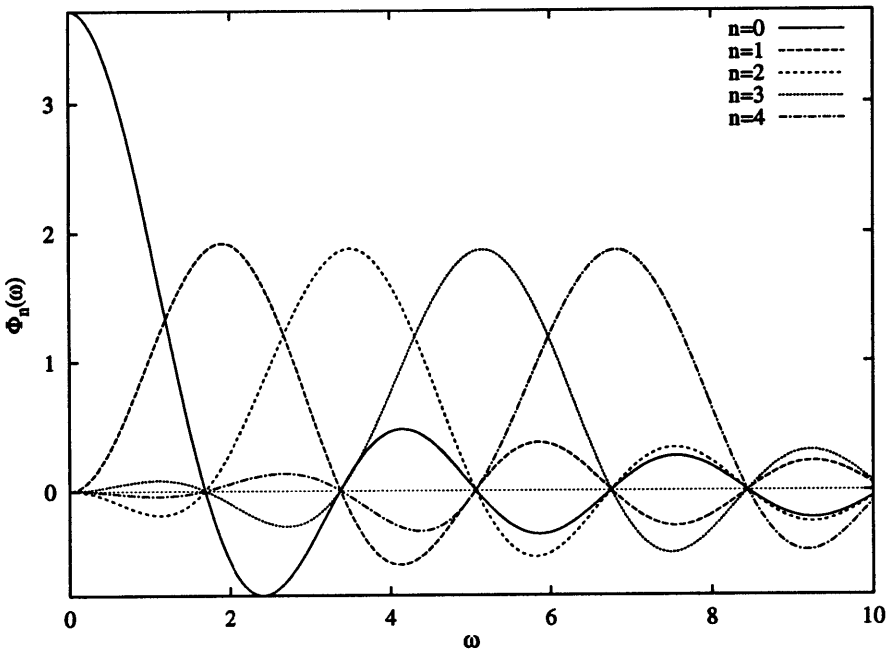

Figure 7-5: Plots of the basis functions $\Phi_n(\omega)$ (defined by Eq. (7.15)) for $0 \leq n \leq 4$.

Essentially, by oversampling $|Z_k(\omega)|$ for $\omega < 4.0$, higher n basis functions can be reconstructed. Additionally, because $\Phi_n(\omega)$ vanishes at $m\omega_0$ unless $n = m$, $|Z_k(\omega)|$ needs to be measured only at $m\omega_0$ to find a_m. For experimental data, however, it is better to make measurements at many frequencies in order to average over noise.

There are better basis functions to use than the functions $\phi_n(t) = \cos(n\omega_0 t)$. The smooth variation of these functions is not well suited to a description of the often sharp features that are characteristic of motion in an atomic system. A further disadvantage of the basis is that it explicitly includes the period $T_k = 2\pi/\omega_0$. It would be advantageous to choose a basis that does not require T_k. Before we introduce the functions that we will use, we must consider that the period affects two other aspects of the fit, the overall scaling and the phase (see Eq. (7.14)). The overall scaling can be removed by absorbing it into the functions $\Phi_n(\omega)$, and the phase disappears if we use the same time-shifted trajectory $z_k(t + T_k/2)$ that we used earlier in this section. Any basis function $\Phi_n(\omega)$ can be used to decompose the real function $Z_k^R(\omega)$

as $\sum_n a_n \Phi_n(\omega)$. The trajectory is then given by $z_k(t) = \sum_n a_n \phi_n(t)$, where

$$\phi_n(t) = \frac{1}{2\pi} \int_{-\infty}^{\infty} \Phi_n(\omega) e^{i\omega t} d\omega. \tag{7.16}$$

For the measurements here, the following temporal basis functions have been used:

$$\phi_n(t) = \frac{1}{2\sigma\sqrt{2\pi}} \left\{ e^{(t-t_n)^2/2\sigma^2} + e^{(t+t_n)^2/2\sigma^2} \right\}. \tag{7.17}$$

The t_n are equally spaced time offsets chosen so that the functions extend a little beyond the period T_k. The width σ is chosen so that neighboring $\phi_n(t)$ overlap. The convergence of the fit does not depend sensitively on the choice of the number of functions or the values of t_n and σ.

Figure 7-6 shows the function $Z_k^R(\omega)$ found by fitting to the measured values [Hag]. A windowed fit, found using the exact classical values rather than the experimental values, is also shown. Note that values of $Z_k^R(0)$ are not used in the fit, but only fix the overall sign of $Z_k^R(\omega)$. The method reproduces $Z_k^R(\omega)$ well at frequencies below the lower limit of the measurements, $\tilde{\omega} = 0.6$. Furthermore, a significant amount of Fourier power for $4 < \tilde{\omega} < 6$ is reconstructed for the 3/4 orbit. Figure 7-7 compares the measured trajectory with the exact classical trajectory and the windowed calculation [Hag]. The result for the 2/3 orbit is not significantly better than the result of the simple method shown in Fig. 7-4. This is because the reconstruction of $Z_k^R(\omega)$ does not recover much more Fourier power than is in the measurement. The power of the method is revealed for the 3/4 orbit, which is recognizable only with the basis-function method.

7.4 Resolution Limit of the Measurement

A measurement of $Z_k(\omega)$ over a range $0 \leq \omega \leq \omega_{\max}$ allows a reconstruction of $z_k(t)$ with a time-resolution $\Delta t \sim 1/\omega_{\max}$. As $\omega_{\max}$ becomes larger, finer and finer features are resolved. Eventually, the semiclassical approximation that underlies closed orbit theory breaks down and the orbital details are limited by the uncertainty principle. In

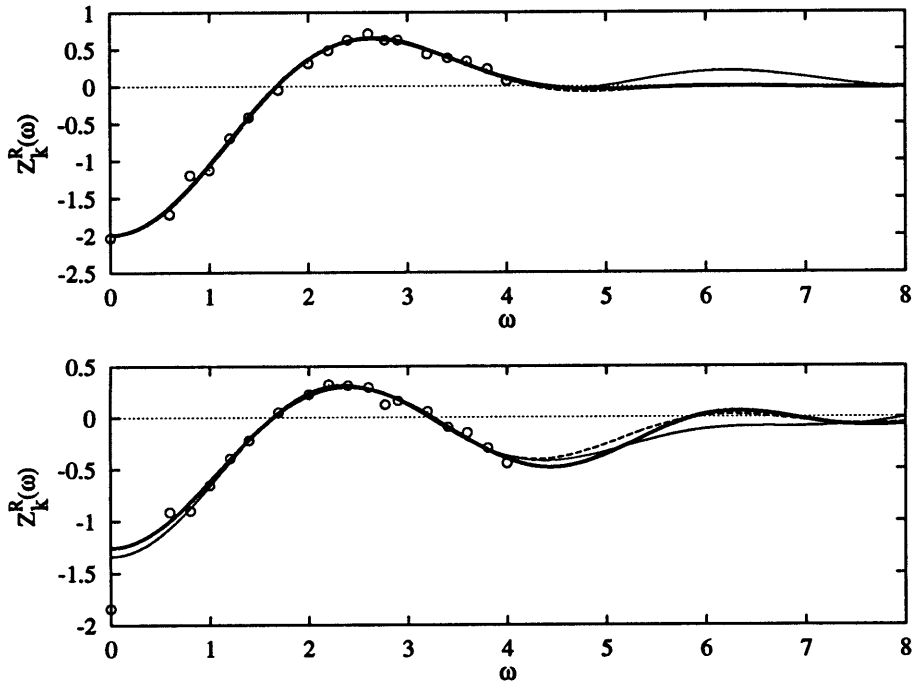

Figure 7-6: Gaussian-basis reconstruction of $Z_k^R(\omega)$ for (a) 2/3 and (b) 3/4 orbits. The light solid line is the exact classical value, the heavy solid line is the fit to the experimental data, and the dashed line is the filtered classical result (often indistinguishable from the solid lines). The circles are the experimental measurements of $|Z_k(\omega)|$ shown in Fig. 7-3 with a sign determined from the constraint that $Z_k^R(\omega)$ is smooth and continuous. The values at $Z_k^R(0)$ are found from Eq. (7.1). The poor agreement for $Z_{3/4}^R(0)$ is unimportant because its value only fixes the overall sign of $Z_{3/4}^R(\omega)$.

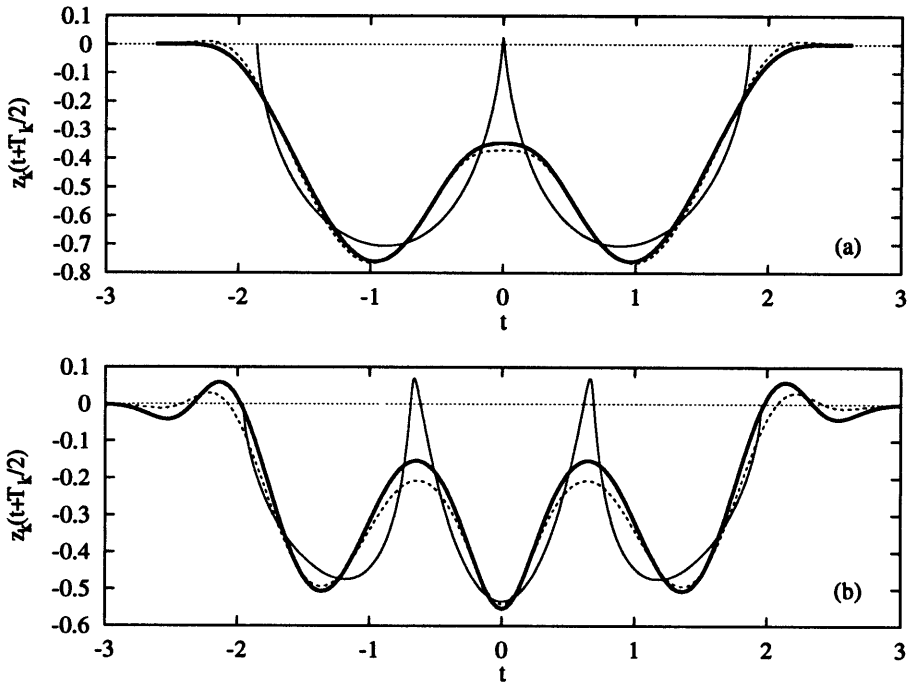

Figure 7-7: Basis-function reconstruction of $z_k(t+T_k/2)$ for (a) 2/3 and (b) 3/4 orbits at $\epsilon = -2.05$. The light solid line is the exact classical trajectory. The heavy solid line is the experimental reconstruction. The dashed line is the reconstruction generated using the exact classical values.

this section we show that differences between the reconstructed motion and the actual classical motion due to the breakdown of the semiclassical approximation are much smaller than the uncertainties arising from the limited resolution. In other words, the experiment could be pushed to much higher frequencies to yield much greater detail about the trajectories.

For a phase-space trajectory, we need values of $z_k(t)$ and the z-component of the momentum, $p_k(t)$. The former is given by Eq. (7.11), and the later is given by

$$p_k(t) = \frac{dz}{dt} = -\frac{1}{\pi}\int_0^{\omega_{\max}} Z_k^R(\omega)\omega \sin[\omega(t - T_k/2)]d\omega. \tag{7.18}$$

As $\omega_{\max}$ increases, an ever larger fraction of phase space is reconstructed. This is easy to see with the following argument. The area of (p_z, z) phase space enclosed by a closed orbit, $A = \int p_z dz$, can be found by parameterizing the trajectory with time, $z = z_k(t)$ and $p_z = p_k(t)$. (The symbol p_k represents the z component of the momentum of orbit k.) Then

$$A = \int_0^T p_k^2(t)dt = \int_{-\infty}^{\infty} p_k^2(t)dt, \tag{7.19}$$

where the limits on the integral have been extended to infinity because $z_k(t) = 0$ for $t < 0$ and $t > T_k$. The Parseval-Plancherel formula [CTDL77] enables us to relate $p_k(t)$ to its Fourier transform, $P_k(\omega)$. Then

$$A = \frac{1}{2\pi}\int_{-\infty}^{\infty} |P_k^2(\omega)|d\omega = \frac{1}{\pi}\int_0^{\infty} |P_k^2(\omega)|d\omega. \tag{7.20}$$

We see that the area of the reconstructed phase space is

$$A = \frac{1}{\pi}\int_0^{\omega_{\max}} \left|P_k^2(\omega)\right| d\omega = \frac{1}{\pi}\int_0^{\omega_{\max}} \omega^2 \left|\tilde{Z}_k^2(\omega)\right| d\omega, \tag{7.21}$$

where the relation $P_k(\omega) = \omega Z_k(\omega)$ has been used.

Figure 7-8 compares the phase-space reconstruction of the 2/3 orbit with an exact classical calculation and with a calculation windowed over the same frequency range,

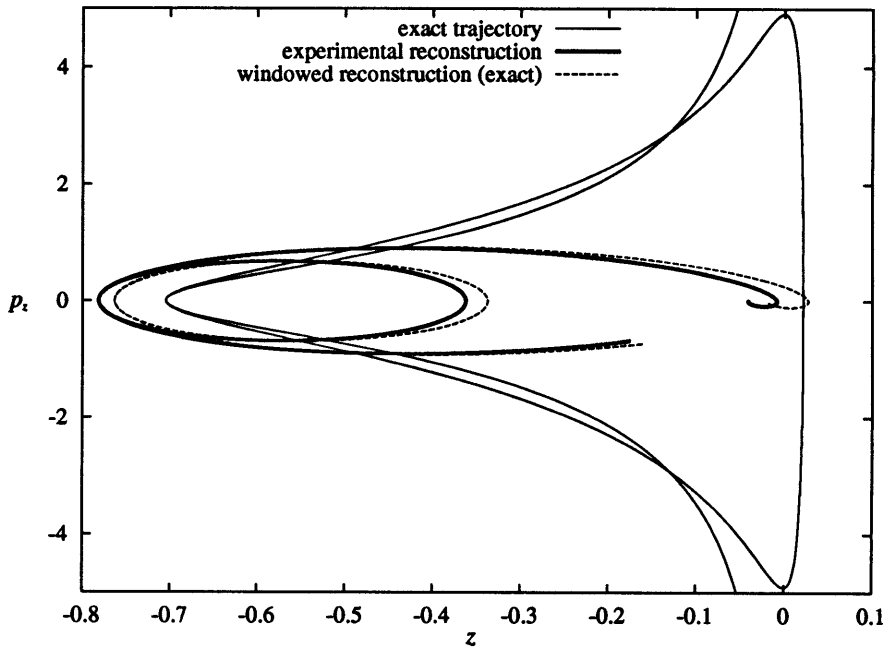

Figure 7-8: Phase-space reconstruction for the 2/3 orbit. The light solid line is the classical calculation. The heavy solid line is the experimental reconstruction. The dashed line is the windowed reconstruction for $\omega \leq 4.0$.

$\tilde{\omega} \leq 4.0$. An ever larger fraction of the phase space is reconstructed as the maximum frequency increases. A calculation shows that the 2/3 and 3/4 orbits enclose phase-space areas equal to 5.65 and 5.34, respectively. The windowed reconstruction with $\tilde{\omega} \leq 4.0$ recovers about 30% and 10% of the total phase space for the 2/3 and 3/4 orbits, respectively.

The uncertainty principle ultimately sets a limit $\Delta z \Delta p_z > \hbar = 1/w = 1/250 = 4 \times 10^{-3}$. The phase-space areas of the 2/3 and 3/4 orbits are of the order of $10^3\hbar$. Because the unreconstructed area of phase space is many $\hbar$, we can conclude that the reconstruction in no way approaches any fundamental limit of the uncertainty principle.

7.5 Discussion

We have seen that the oscillating field enables a finite-resolution measurement of a component of the trajectory of the 2/3 and 3/4 orbits at $\epsilon = -2.05$. Although the experimental challenge of extending the method is daunting, having established its validity experimentally it is worth considering the possibilities of extracting classical trajectories in more general circumstances. The experimental technique requires that only one orbit contribute significantly to a recurrence, and one must be able to measure its period. A more general method may be to extract $|Z(\omega)|$ for several orbits with similar actions by fitting the recurrence strength to a sum of Bessel functions. Because this approach would require large quantities of high-quality data, it would be more practical with computed spectra.

The method can in principle be extended to measure the full three-dimensional trajectory by successively applying an oscillating field along the x and y directions. Appendix B shows that the recurrence strength of an orbit subjected to an oscillating field perpendicular to the static field should decrease as $J_0^4(c\tilde{f})$, where c is related to the radial ac dipole moment of the orbit. Implementing this measurement experimentally is difficult because a perpendicular field must be applied without any component parallel to the static field. Otherwise, the first-order shift produced by the parallel component would obscure the results. A computational implementation is in principle possible, but would be difficult because of the large basis size required.

The requirement of time-reversal symmetry and knowledge of the period prevents this from being a general method for reconstructing trajectories. For example, the orbits in the diamagnetic system are not constrained by this symmetry. It is unclear whether this difficulty can be overcome.

Although the utility of the oscillating field as a tool for conducting useful experimental reconstructions of classical trajectories is questionable, the limitations for computed spectra are much less severe. We have a fundamentally new method for finding classical motion from quantum mechanics. Its useful applications remain to be determined.

Chapter 8

Conclusion

This thesis has presented an experimental and theoretical study of the recurrence spectra of Rydberg atoms in external fields. By applying an oscillating electric field parallel to a static field, the magnitude of the ac dipole moment of a given orbit along the direction of the field can be determined. The new observations include:

- Recurrence spectra at $\epsilon = -0.4$ show good agreement with closed orbit theory extended to a time-dependent system. Experiments at low frequency ($0.12 \leq \tilde{\omega} \leq 0.6$) have been compared with detailed closed orbit theory computations and semiquantal Floquet computations. All three show good agreement.

- The oscillating field yields new information about the strengths of orbits contributing to a recurrence in regions where multiple orbits with similar actions can not be resolved by traditional recurrence spectroscopy. This was first achieved in the $\epsilon = -0.4$ measurements in which differences between measured falloff rates and falloff rates predicted for the uphill orbit allow one to distinguish the contributions of the uphill orbit from bifurcated orbits. The clearest illustration is at $\epsilon = -2.05$, where it is shown that the recurrences with actions equal to two and three repetitions of the downhill orbit are dominated by the 2/3 and 3/4 orbits, respectively.

- Quantum Floquet computations of recurrence spectra of hydrogen and lithium at low energies and frequencies were described. The results for hydrogen showed

good agreement with time-dependent closed orbit theory. A model based on closed orbit theory was developed to describe the behavior of core-scattered orbits in an oscillating field. In principle, one should be able to distinguish different orders of core-scattering, although this has not been demonstrated.

- The $z(t)$ component of the 2/3 and 3/4 orbits at $\epsilon = -2.05$ was measured with finite time-resolution. Within the limited frequency resolution, the experiments and theory were in excellent agreement, demonstrating the power of the method.

Many questions about Rydberg atoms in oscillating fields remain to be studied.

- What is the behavior at higher field amplitudes $\tilde{f}$, where perturbation theory breaks down? The framework of closed orbit theory describes this regime, but it remains to be tested.

- To how high a frequency of applied field does closed orbit theory work? The measurements at $\epsilon = -2.05$ have shown that the description is valid when the frequency is close to three times the frequency of an orbit. At some large frequency, the semiclassical limit breaks down, but the nature of this breakdown is unclear. Two possibilities are that the initial state is affected by the oscillating field, or that the semiclassical approximation breaks down when the electron is far from the nucleus. The ability to conduct experiments over much higher frequency ranges with controlled amplitude would greatly aid this investigation.

- What is the effect of a perpendicular oscillating electric field? Appendix B is a theoretical description within the framework of closed orbit theory, but remains to be tested experimentally.

- How does the diamagnetic system behave in the presence of an oscillating electric field? Because the diamagnetic system is chaotic in some regimes, it provides a testing ground for the fundamental question of quantum chaos—can quantum systems show chaotic motion. Using an oscillating field to reveal classical closed orbits in a regime of chaos would be an important step toward

answering this question. Although orbits should interact according to their dipole moments, the lack of time-reversal symmetry would prevent our method of orbit reconstruction from working. It is unclear if this is just a detail, or if this is a sign that chaotic quantum systems are fundamentally different.

The achievements of closed orbit theory and recurrence spectroscopy are based on a relatively small amount of spectroscopic quantum information—energy levels and overlaps of eigenstates with a localized ground state. Much more information about classical motion is contained within the wave function itself, for the wave function is intimately linked with the classical trajectories through the semiclassical approximation to the wave function. However, there is no general and practical method for extracting the wave function experimentally. The introduction of an oscillating field has taken us a step closer toward extracting this information because it gives information about some of the trajectories—those of the closed orbits.

Appendix A

Scaling Properties of Assorted Systems

In this appendix we examine the scaling properties of the Stark system and two other prototype systems: the harmonic oscillator and an electron in a Coulomb potential. We derive the scaling laws and consider a few aspects of recurrence spectroscopy in these systems. Finally, we consider the effects of periodic perturbations, and what information about the nature of classical motion can be learned from the perturbations.

A.1 Hydrogen in a Static Electric Field

We consider the familiar Hamiltonian of a Rydberg atom in an external static electric field F,

$$H = \frac{p^2}{2} - \frac{1}{r} + Fz. \tag{A.1}$$

Let $\tilde{p} = F^a p$ and $\tilde{r} = F^b r$. Substitution into Eq. (A.1) gives

$$H = F^{-2a}\left(\frac{\tilde{p}^2}{2} - F^{b+2a}\frac{1}{\tilde{r}} + F^{1-b+2a}\tilde{z}\right). \tag{A.2}$$

This produces two constraints on a and b: $b = -2a$ and $b = 2a+1$. Their solution gives the familiar results $a = -1/4$ and $b = 1/2$. The scaled energy is $\epsilon = F^{2a}E = F^{-1/2}E$.

Note that only the classical Hamiltonian scales. Planck's constant sets an action scale for the quantum Hamiltonian, which does not scale because $p = -i\hbar\nabla$. When the above transformations $\tilde{p} = F^{-1/4}p$ and $\tilde{r} = F^{1/2}r$ are used, the Schrödinger equation becomes

$$\left[\frac{1}{2}\left(\frac{\hbar}{w}\right)^2 \tilde{\nabla}^2 - \frac{1}{\tilde{r}} + \tilde{z}\right]\psi = \epsilon\psi. \tag{A.3}$$

We see that $w = F^{-1/4}$ determines the effective size of Planck's constant. The semiclassical limit is approached as w becomes large.

The unit of scaled action is $\tilde{S} \sim \tilde{p}\tilde{q} \sim F^{a+b}S \sim F^{1/4}S$. Closed orbit theory asserts that each orbit with action S modulates the photoabsorption spectrum as $Df \sim \sin(S/\hbar) \sim \sin(\tilde{S}F^{-1/4})$. The spectrum should be measured with respect to the variable $w = F^{-1/4}$ in order that each orbit modulates the spectrum with the same frequency over the entire measurement range.

Closed orbit theory asserts the equivalence between the quantum spectrum measured with resolution δw and a sum over all closed orbits with action up to $\delta\tilde{S} = 2\pi/\delta w$. Unfortunately, the structure of both the quantum spectrum and the classical orbits is too complex to make much progress toward showing this equivalence analytically. We therefore turn to a simpler system.

A.2 Harmonic Oscillator

The Hamiltonian of the one-dimensional harmonic oscillator is

$$H = \frac{p^2}{2} + \frac{1}{2}kx^2. \tag{A.4}$$

This problem is different than the Stark problem because there is no external field with which to scale the position and momentum. However, we can scale these by the spring constant k. Scaling $\tilde{p} = k^a p$ and $\tilde{x} = k^b x$ as before gives

$$H = k^{-2a}\left(\frac{\tilde{p}^2}{2} + \frac{1}{2}k^{1-2b+2a}\tilde{x}^2\right). \tag{A.5}$$

In contrast to Eq. (A.2), there is only one condition on the scaling exponents: $2b = 1 + 2a$. With the simple choice $a = 0$, $b = \frac{1}{2}$, the scaled energy is $\epsilon = E$, the scaled action is $\tilde{S} = k^{1/2}S$, and $w = k^{-1/2}$.

The quantum-mechanical energy levels are $E_n = n\sqrt{k}$ (neglecting the zero-point energy). Recurrence spectroscopy could be performed (at least numerically, if not experimentally) by recording the transition strength from the ground state to an excited state as the energy and spring constant are varied to maintain a constant scaled energy. This is done simply by holding E constant while k is changed and the spectrum is recorded as a function of $w = k^{-1/2}$. The spectrum would reveal equally spaced peaks at $w = 2n/\epsilon$. The factor 2 arises from the fact that states with even and odd n have even and odd parity, respectively. While the energy levels occur at each n, a transition from the ground state occurs only to states of opposite parity. The Fourier transform of such a recurrence spectrum reveals peaks at actions $\tilde{S} = N2\pi/\delta w = N2\pi\epsilon/2 = N\pi\epsilon$, where N is an integer. In this simple system, we can find the closed orbits analytically and show that the result is what one expects classically

The scaled Hamiltonian has the simple form

$$\epsilon = \frac{\tilde{p}^2}{2} + \frac{\tilde{x}^2}{2}. \tag{A.6}$$

The motion of a particle with energy ϵ is

$$\tilde{x}(\tilde{t}) = \sqrt{2\epsilon}\sin\tilde{t}. \tag{A.7}$$

The primitive *closed* orbit is the trajectory that leaves the origin ($\tilde{x} = 0$) traveling along the positive x axis, stops at a distance $x_{\max}$, and returns to $\tilde{x} = 0$. The motion continues along the negative x axis, and its second return to $\tilde{x} = 0$ completes the first *periodic* orbit.

The action of the primitive closed orbit is

$$\tilde{S} = \oint \tilde{p}d\tilde{q} \tag{A.8}$$

$$= 2\int_0^{\tilde{x}_{\max}} \sqrt{2\epsilon - \tilde{x}^2}\, d\tilde{x} \tag{A.9}$$

$$= 2(2\epsilon)\int_0^{\pi/2} \cos^2\theta\, d\theta \tag{A.10}$$

$$= \pi\epsilon. \tag{A.11}$$

This agrees with the result expected from the quantum-mechanical analysis given above. Periodic orbit theory relates the quantum-mechanical *density of states* to a sum over all *periodic* orbits. The fundamental periodic orbit has an action of $2\pi\epsilon$, which is consistent with the fact the lowest frequency modulation of the density of states is twice as large as the lowest frequency modulation of the oscillator strength.

A.3 Charged Particle Bound by a Coulomb Potential

The Hamiltonian of an electron bound by a Coulomb potential with charge α is

$$H = \frac{p^2}{2} - \frac{\alpha}{r}. \tag{A.12}$$

There is no parameter here that can be varied experimentally to perform recurrence spectroscopy. However, the strength of the binding potential α can be varied numerically. Scaling $\tilde{p} = \alpha^a p$ and $\tilde{r} = \alpha^b r$ gives

$$H = \alpha^{-2a}\left(\frac{\tilde{p}^2}{2} - \frac{1}{\tilde{r}}\alpha^{b+2a+1}\right). \tag{A.13}$$

With $a + 2b = -1$, the Hamiltonian is that of a hydrogen atom. Choosing $a = 0$ and $b = -1$ gives a scaled energy $\epsilon = E$, scaled action $\tilde{S} = S/\alpha$, and $w = \alpha$.

The energy levels of the Hamiltonian (A.12) are given by $E_n = -\alpha^2/2n^2$. When the spectrum is recorded as a function of w, equally spaced levels at $w = \sqrt{-2\epsilon}n$ are found. The Fourier transform of the spectrum thus reveals peaks at actions $\tilde{S} = 2\pi/\sqrt{-2\epsilon}$.

The scaled Hamiltonian separates in semiparabolic coordinates to give two inde-

pendent harmonic oscillators,

$$h = \frac{\tilde{p}_\mu^2}{2} + \frac{\tilde{p}_\nu^2}{2} - \epsilon(\mu^2 + \nu^2) = 2. \tag{A.14}$$

Identical closed orbits exist at all initial angles θ. For $\theta = 0$, $\mu(t) = \sqrt{-2/\epsilon}\sin(\sqrt{-\epsilon}t)$. The action of this orbit is $\tilde{S} = 2\pi/\sqrt{-2\epsilon}$, in agreement with the expectation from the quantum spectrum.

A.4 Periodic Perturbations to Simple Scaling Systems

Here we examine the effect of periodic perturbations to the above systems. We begin by adding an oscillating "electric" field $F_1 x \cos\omega t$ to the harmonic oscillator Hamiltonian Eq. (A.4). The scaled Hamiltonian (A.5) becomes

$$\epsilon = \frac{\tilde{p}^2}{2} + \frac{\tilde{x}^2}{2} + \tilde{f}\tilde{x}\cos(\tilde{\omega}\tilde{t}), \tag{A.15}$$

where $\tilde{f} = k^{2a-b}F_1 = k^{-1/2}F_1$ and $\tilde{\omega} = k^{a-b}\omega = k^{-1/2}\omega$. The semiclassical theory discussed in Chapter 2 indicates that the perturbation to the action $\tilde{S}$ caused by the oscillating field is, from Eq. (2.37),

$$\frac{d\tilde{S}}{d\tilde{f}} = \int_0^{\tilde{T}} \tilde{x}(\tau)\cos(\tilde{\omega}\tau)d\tau. \tag{A.16}$$

Because this integral is a time-integrated ac dipole moment, the result is the same as that found for a Rydberg atom in combined parallel and static oscillating electric fields: orbits interact with the oscillating field through their ac dipole moments.

We find different behavior if we consider a periodic variation of the spring constant, $k + k_1\cos\omega t$. The scaled Hamiltonian (A.5) becomes

$$\epsilon = \frac{\tilde{p}^2}{2} + \left(1 + \tilde{f}\cos(\tilde{\omega}\tilde{t})\right)\frac{\tilde{x}^2}{2} \tag{A.17}$$

where $\tilde{f} = k_1/k$ and $\tilde{\omega} = \omega k^{a-b} = k^{-1/2}\omega$. The perturbation to the action $\tilde{S}$ is

$$\frac{d\tilde{S}}{d\tilde{f}} = \int_0^{\tilde{T}} \frac{1}{2}\tilde{x}^2(\tau)\cos(\tilde{\omega}\tau)d\tau. \tag{A.18}$$

A given orbit interacts here as a time-integrated mean-square dipole moment.

Finally, we consider a periodic variation to the Coulomb potential described in Sec. A.3. Adding a periodic variation of the charge, $\alpha + \alpha_1 \cos\omega t$, leads to a scaled Hamiltonian

$$H = \frac{\tilde{p}^2}{2} - \frac{1}{\tilde{r}}\left(1 + \tilde{\alpha}\cos(\tilde{\omega}\tilde{t})\right), \tag{A.19}$$

where $\tilde{\alpha} = \alpha_1/\alpha$ and $\tilde{\omega} = \alpha^{a-b}\omega = \alpha\omega$. The perturbation to the action $\tilde{S}$ is

$$\frac{d\tilde{S}}{d\tilde{\alpha}} = \int_0^{\tilde{T}} \frac{1}{\tilde{r}}\cos(\tilde{\omega}\tau)d\tau. \tag{A.20}$$

We see that in this case the oscillating field yields information about the average value of $1/\tilde{r}$.

Appendix B

Some Results for a Perpendicular Field

In this appendix we develop some results about the effect of an oscillating electric field with a direction perpendicular to a static electric field. The description of time-dependent closed orbit theory given in Sec. 2.3 holds for an oscillating field with any direction. That description relates the effect of an oscillating field on a recurrence to the perturbation to the action of an orbit. The Hamiltonian for a Rydberg atom in a static electric field F along the z axis and an oscillating electric field F_1 polarized along the x axis is

$$H = \frac{p^2}{2} - \frac{1}{r} + Fz + F_1 x \cos(\omega t + \alpha). \tag{B.1}$$

We calculate from Eq. (2.37) the effect of the oscillating field by considering the perturbation to the action of an orbit.

With just a static field along the z axis, the orbits are two-dimensional, defined by z and ρ coordinates, where ρ is the cylindrical-radial distance from the z axis. Because the perpendicular field breaks the cylindrical symmetry of the system, orbits moving along the x direction are perturbed differently than orbits moving along the y direction. A orbit k with period T_k and action S_k exists in the (z, ρ) plane, and can

be described by a trajectory $(z_k(t), \rho_k(t))$. The perturbation to its action is

$$\frac{dS_k}{dF_1} = -\int_{t-T_k}^{t} x_k(\tau')\cos(\omega\tau' + \alpha)d\tau', \tag{B.2}$$

where $x_k(t) = \rho_k(t)\cos\varphi$ and φ is the azimuthal angle.

The calculation proceeds in the same manner as the calculation in Sec. 2.3.1 for the parallel oscillating field. The action is

$$S_k(t) = S_k^0 - F_1\,|Z_k(\omega)|\cos(\varphi)\cos(\omega t + \phi_k), \tag{B.3}$$

where $Z_k(\omega)$ is redefined as

$$Z_k(\omega) = \int_0^{T_k} \rho_k(\tau)e^{-i\omega\tau}d\tau. \tag{B.4}$$

and ϕ_k is defined by Eq. (2.44). The excitation rate (2.46) in scaled coordinates becomes

$$R_f = R_0 + \overline{\sum_k C_k(\tilde{t})\sin\left[2\pi\tilde{S}_k^0 w + (\tilde{f}|\tilde{Z}_k(\tilde{\omega})|w)\cos(\varphi)\cos(\tilde{\omega}\tilde{t} + \phi_k) - \gamma_k\right]}\,, \tag{B.5}$$

where the overline indicates an average over a cycle of the field *and* over φ. The averaging proceeds by expanding the sine term. One term averages to zero while the other term leads to the integral

$$\begin{aligned} R_x &= R_0 + \sum_k C_k \sin\left(2\pi\tilde{S}_k^0 w - \gamma_k\right) \\ &\times \frac{1}{2\pi}\int_0^{2\pi} d\varphi \frac{1}{2\pi}\int_0^{2\pi} d(\tilde{\omega}\tilde{t})\cos\left[\tilde{f}|\tilde{Z}_k(\tilde{\omega})|w\cos(\varphi)\cos(\tilde{\omega}\tilde{t} + \phi_k)\right]. \end{aligned} \tag{B.6}$$

The integral over $\tilde{\omega}\tilde{t}$ introduces a Bessel function, giving

$$R_x = R_0 + \sum_k C_k \sin\left(2\pi\tilde{S}_k^0 w - \gamma_k\right)\frac{1}{2\pi}\int_0^{2\pi} d\varphi J_0\left[\tilde{f}|\tilde{Z}_k(\tilde{\omega})|w\cos(\varphi)\right]\,. \tag{B.7}$$

This equation is simplified with the identity [GR80]

$$\int_0^{\pi/2} J_0(2z\cos x)dx = \frac{\pi}{2}J_0^2(z). \tag{B.8}$$

The result is

$$R_x = R_0 + \sum_k C_k J_0^2\left(\tilde{f}|\tilde{Z}_k(\tilde{\omega})|w/2\right)\sin\left(2\pi\tilde{S}_0 w - \gamma_k\right). \tag{B.9}$$

A given orbit loses strength as J_0^4 as $\tilde{f}$ is increased. Although this function falls off faster than J_0^2, this does not mean that the perpendicular field has a stronger effect on the spectrum because most orbits in the electric field have larger dipole moments along the z direction than along the radial direction.

Appendix C

Atomic Units

Most of the equations in this thesis are given in atomic units. This system of units is defined by setting $\hbar = m = e = 1$, where m is the reduced mass of the atom and e is the electron charge. The values of these units depend on the atom because the reduced mass of the atomic system is used. Table C.1 shows the values of several units for ^{7}Li and H. It is important to use the appropriate values in the quantum Floquet computations because incorrect values produce shifts that are larger than the experimental resolution.

The energy of a Rydberg state is given by

$$E_n = -\frac{1}{2(n-\delta_l)^2}, \tag{C.1}$$

where δ_l is the quantum defect of the state. The quantum defect for ^{7}Li is given by the recursive formulas [Kas88, Joh59]

$$\delta_s = 0.399,491,74 + 0.029,483t + 0.002,24t^2 \tag{C.2}$$

$$\delta_p = 0.047,160,1 - 0.022,816t + 0.007,82t^2 \tag{C.3}$$

$$\delta_d = 0.001,932,0 - 0.004,11t \tag{C.4}$$

$$\delta_f = 0.000,310,3 - 0.001,27t. \tag{C.5}$$

The variable t is defined by $t = |E_n|/R$ where R is the Rydberg constant for ^{7}Li,

Quantity	Formula	^{7}Li	H
Energy (cm^{-1})	$me^4/\hbar^2$	$2.194,574,700(2) \times 10^5$	$2.193,551,660(2) \times 10^5$
Length (cm)	$\hbar^2/me^2 = a_0$	$5.292,1863(2) \times 10^{-9}$	$5.294,6545(2) \times 10^{-9}$
Velocity (cm/s)	$e^2/\hbar = v_0$	$2.187,69(2) \times 10^8$	$2.187,69(2) \times 10^8$
Electric Field (V/cm)	e/a_0^2	$5.141,4041(5) \times 10^9$	$5.136,611(1) \times 10^9$
Magnetic Field (T)	$\hbar/ea_0^2$	$2.350,150(3) \times 10^5$	$2.347,960(3) \times 10^5$
Frequency (s^{-1})	v_0/a_0	$4.133,80(6) \times 10^{16}$	$4.131,88(6) \times 10^{16}$

Table C.1: Atomic units for ^{7}Li and H. The uncertainty in the last digit is given in parentheses.

which equals half the atomic unit of energy given in Table C.1.

The energy of the transition from $3s$ to a Rydberg state is given by $E = E_{3s} - |E_n|$, where the $3s$ binding energy is $E_{3s} = 16,281.064(1)$ cm^{-1} [Kas88].

Appendix D

Paper: Recurrence Spectroscopy of a Time-Dependent System: A Rydberg Atom in an Oscillating Field

Recurrence Spectroscopy of a Time-Dependent System: A Rydberg Atom in an Oscillating Field

Neal Spellmeyer and Daniel Kleppner
Research Laboratory of Electronics, George R. Harrison Spectroscopy Laboratory, and Department of Physics, Massachusetts Institute of Technology, 77 Massachusetts Avenue, Cambridge, Massachusetts 02139

M. R. Haggerty, V. Kondratovich, and J. B. Delos
Physics Department, College of William and Mary, Williamsburg, Virginia 23187

J. Gao
Chemistry and Physics Department, Kean College, Union, New Jersey 07083
(Received 28 April 1997)

We report the results of an experimental and theoretical investigation of the recurrence spectra of Rydberg atoms in a static plus weak oscillating electric field. Experiments reveal the systematic weakening of orbits in a recurrence spectrum as the oscillating field strength and frequency are changed. We describe a generalization of closed orbit theory to time-dependent systems and show that it provides a qualitative and quantitative description of the phenomena. [S0031-9007(97)03947-1]

PACS numbers: 32.60.+i, 03.65.Sq, 05.45.+b

In the quest for a satisfactory understanding of the connections between quantum and classical descriptions of simple Hamiltonian systems, Rydberg atoms in applied fields provide prototypes for experiment and theory [1]. Recurrence spectroscopy and closed orbit theory have proven to be powerful tools for these studies [2–4]. A recurrence spectrum is the Fourier transform of a photoexcitation spectrum that is taken with the field varying with energy according to a classical scaling rule that keeps the classical motion unchanged at all points in the spectrum [2]. It can be shown that each closed classical orbit of the electron generates a peak in the recurrence spectrum at the action of the orbit. Consequently, the recurrence spectrum provides a quantum picture of classical behavior. Studies of recurrence spectra have led to observations of the creation of new orbits through bifurcations [5,6], the onset of irregular behavior through core scattering [7–10], symmetry breaking in crossed fields [11], and the identification of numerous closed orbits [1].

We have extended this line of inquiry by investigating the recurrence spectrum of a Rydberg atom in a field that is oscillating with a period which is comparable to the period of its classical orbits. The underlying thought is that periodic orbits should be sensitive to periodic perturbations, and that this sensitivity should be revealed by recurrence spectra. Recurrences with periods that are integer multiples of the period of the perturbing field might be expected to be most affected. We report here the first results of such a study. The experimental observations are surprising: Recurrences with periods near integer multiples of the period of the perturbation survive, while those that are out of "resonance" with the field are weakened or eliminated. We have been able to interpret these results by generalizing closed orbit theory to incorporate periodic fields, obtaining both a qualitative and quantitative description of the phenomena.

Our study employs a lithium Rydberg atom in a static electric field—a system we have previously studied [8]—but now with the addition of an oscillating field. At the low actions studied in these experiments, the spectrum is regular and can be understood by considering only the closed orbits of hydrogen. Experimentally, introducing an rf field is a straightforward task. (We use "rf" to signify the oscillating field though the actual frequency may be in the microwave regime.)

The Hamiltonian of a Rydberg atom in an electric field F along the z axis and an rf field with amplitude F_1 oscillating at angular frequency ω, also polarized along the z axis, is taken to be (in atomic units)

$$H = \frac{p^2}{2} - \frac{1}{r} + Fz + F_1 z\cos(\omega t). \qquad (1)$$

Recurrence spectroscopy is possible because the classical Hamiltonian can be expressed completely in scaled variables. We define $\tilde{r} = F^{1/2}r$, $\tilde{p} = F^{-1/4}p$, $\tilde{t} = F^{3/4}t$, $\tilde{\omega} = F^{-3/4}\omega$, and $\tilde{f} = F^{-1}F_1$. This yields the scaled Hamiltonian

$$\tilde{H} = \frac{\tilde{p}^2}{2} - \frac{1}{\tilde{r}} + \tilde{z}[1 + \tilde{f}\cos(\tilde{\omega}\tilde{t})] = F^{-1/2}E(t). \qquad (2)$$

In the oscillating field, the electron energy $E(t)$ is not constant. We define $\epsilon \equiv F^{-1/2}E^{\text{out}}$ to be the scaled energy of the electron as it leaves the atom. The scaled action is $\tilde{S} = F^{1/4}S$ [12]. To obtain a recurrence spectrum we simultaneously vary the laser energy, static and rf field amplitudes, and the rf frequency so as to keep the scaled parameters (ϵ, $\tilde{f}$, and $\tilde{\omega}$) constant as we record the photoabsorption spectrum.

The experimental setup is similar to that described in [8]. Lithium is excited to the $3s$ state by two-step

 0031-9007/97/79(9)/1650(4)$10.00

resonant excitation $2s \rightarrow 2p \rightarrow 3s$ and then to an $m = 0$ Rydberg state by a tunable laser. The scaled energy and frequency are known to an accuracy of about 0.1%. The rf field amplitude was calibrated by measuring sidebands on various states in a Stark manifold [13], yielding an overall accuracy in F_1 of 10%, with 1% accuracy at selected calibration points. In our experiments, we measure actions up to $\tilde{S} \approx 150$.

We chose to study behavior at scaled energy $\epsilon = -0.4$, which we had mapped previously for a static electric field [6]. Because this energy lies above the saddle point threshold for ionization ($\epsilon = -2$), orbits directed towards the negative z direction are absent. The most important orbit is the parallel "uphill" orbit lying along the positive z axis, and its repetitions. These form a spectrum of recurrences equally spaced in action at an interval $\Delta\tilde{S} = 4.337$. The second repetition lies close to a bifurcation point at $\epsilon = -0.397$ [14], which strongly enhances its recurrence strength. In contrast, the first repetition is extremely weak. We mapped recurrence spectra with constant scaled amplitude $\tilde{f}$ and also constant scaled frequency $\tilde{\omega}$.

Figure 1 displays a panoramic map of recurrence spectra at $\tilde{f} = 0.005$, with $\tilde{\omega}$ varying from 0.12 to 0.60. The most conspicuous feature is a series of regions where the recurrences are practically annihilated and a series of regions where they survive. The periods of the surviving orbits are near integer multiples of $2\pi/\tilde{\omega}$, shown by dark lines in the plot. In addition, the strong second repetition persists at all frequencies measured.

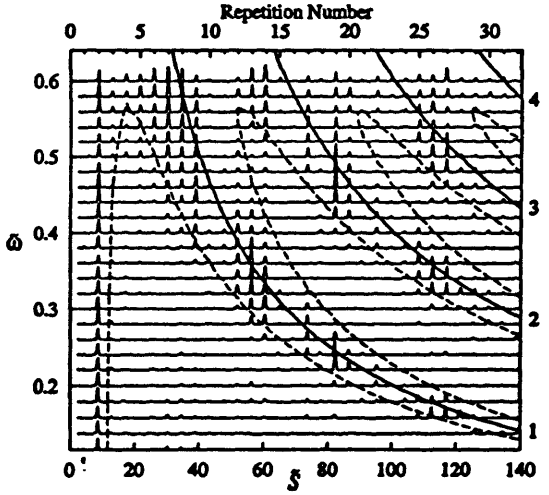

FIG. 1. Experimental recurrence spectra recorded at $\epsilon = -0.4$ and $\tilde{f} = 0.005$, with scaled frequency $\tilde{\omega}$ between 0.12 and 0.60 in steps of 0.02. The dashed lines are contours generated from Eq. (10) where $a_n = 0.2$. The solid curved lines mark the action at which a repetition of the parallel orbit has a period that is an integer multiple n of the period of the applied field. The values of n are listed on the right.

Figure 2 displays a map at fixed frequency $\tilde{\omega} = 0.32$, with $\tilde{f}$ varying from 0.0 to 0.022. As $\tilde{f}$ increases, all the peaks lose strength. Some recurrences are very sensitive and fall off rapidly as $\tilde{f}$ increases; others persist to much higher $\tilde{f}$. As the rf field is made yet stronger, many of the peaks revive, some more than once.

The peaks in Figs. 1 and 2 are manifestations of recurrences—classical orbits which go out from the nucleus and return. To interpret the data, we briefly review the ideas of closed orbit theory and then discuss its extension to a time-periodic Hamiltonian. The theory of recurrences begins from the usual quantum theory of photoexcitation: As the laser radiation causes transitions between the initial state and high energy eigenstates of H, there is a well-defined rate of absorption. The smoothed or large scale structure of the spectrum can be expressed as an oscillator strength density, which we denote $Df(E,F)$. The oscillator strength density can be separated into two parts:

$$Df(E,F) = Df_0 + Df_1(E,F). \quad (3)$$

Df_0 is a smooth (practically constant) background that is approximately the same as for the field-free atom at the ionization threshold. $Df_1(E,F)$, which varies rapidly with E and F, is due to recurrences that arise in the following manner. The laser radiation produces a stream of outgoing waves which, in the semiclassical approximation, follow classical trajectories. As the trajectories travel outward, some are turned back by the combined Coulomb and applied fields and return to the atom. These interfere with the outgoing waves (and with each other), giving rise to oscillatory patterns in the absorption spectrum. Each returning orbit k gives a sinusoidal

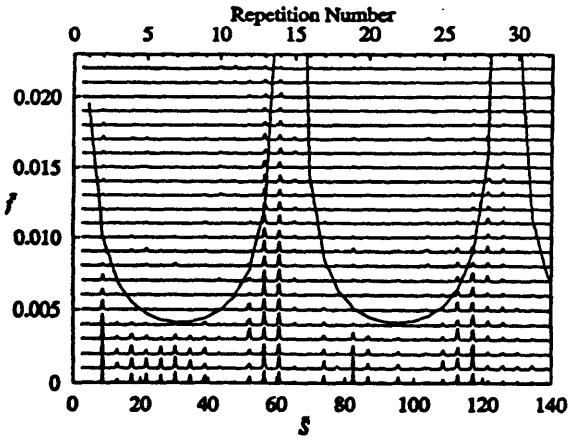

FIG. 2. Experimental recurrence spectra recorded at $\epsilon = -0.4$ and $\tilde{\omega} = 0.32$ with scaled rf field amplitude $\tilde{f}$ between 0.0 and 0.022. The solid curved lines mark the location of the first zero in the recurrence strength as predicted by the restricted semiclassical theory, Eq. (10).

contribution to the oscillator strength density,

$$Df_{1,k}(E,F) = C_k \sin[S_k^0(E,F)/\hbar + \gamma_k]. \quad (4)$$

The corresponding expression in scaled variables is

$$Df_{1,k}(\epsilon,w) = C_k \sin[\tilde{S}_k^0(\epsilon)w + \gamma_k]. \quad (5)$$

$S_k^0(E,F) = \int \mathbf{p}\cdot d\mathbf{q}$ is the classical action around the closed orbit, $\tilde{S}_k^0(\epsilon)$ is its scaled counterpart $w = F^{-1/4}$, and γ_k is a phase correction associated with Maslov indices. C_k is the recurrence amplitude, which is approximately independent of E and F. The absolute square of the Fourier transform of the absorption spectrum with respect to w gives the recurrence spectrum, which reveals peaks at the scaled actions of the closed orbits.

We have generalized closed orbit theory to incorporate a time-dependent Hamiltonian. We summarize the main features here—a full description will be published elsewhere. The explicit time dependence of the Hamiltonians in Eqs. (1) and (2) means that many aspects of recurrence theory need to be reexamined. It can be shown [15] that at each time t, it is possible to define an instantaneous oscillator strength density $Df(E,F;F_1,\omega,t)$ out of the initial state into a band of excited states. Df can be separated again as in Eq. (3), with Df_1 arising from closed orbits. The physical picture is much as before. The laser produces a steady stream of outgoing waves, which now propagate in the oscillating electric field. The result is a time-dependent wave function that in the semiclassical description is "supported" by time-dependent classical trajectories. Each returning orbit in the static field represents a continuous family of identical orbits, each starting at a different time. With the oscillating field turned on, the orbits in a family are no longer identical because their properties then depend on the phase of the rf field when they left the atom. We call this splitting of a single orbit into a continuous family of orbits "temporal symmetry breaking," because of its close analogy to cylindrical symmetry breaking [11,15]. The component of Df_1 arising from each family oscillates at the rf frequency, and the measurement averages it over many cycles.

The returning wave can be calculated using a semiclassical approximation in an extended phase space $(\mathbf{p},\mathbf{q},E,t)$ where time is regarded as a dynamical variable. The conjugate variable E is not conserved because of the temporal symmetry breaking. The action associated with the returning wave is again the classical action, but now in the extended phase space:

$$R(t) = \int \{\mathbf{p}\cdot d\mathbf{q} - [H(t) - E^{\text{out}}]dt\}. \quad (6)$$

This generalized action depends on the phase of the field relative to the orbit. For some phases, the orbit is stretched and its action increases, while for others, the orbit is compressed, and its action decreases. At small rf amplitudes, there is a smooth sinusoidal change between these two extremes. Using first order classical perturbation theory, the generalized action is found to be

$$R_k(t) \approx S_k^0(E,F) + F_1|Z_k(\omega)|T_k\cos(\omega t - \alpha_k), \quad (7)$$

where T_k is the period of the orbit, $Z_k(\omega)$ is the time-averaged ac electric dipole moment of the *unperturbed* orbit $(1/T_k)\int_0^{T_k} z(\tau)e^{-i\omega\tau}d\tau$, and α_k is the phase of the rf field for which the maximal action is attained.

Substituting Eq. (7) into Eq. (5), averaging over a cycle of the field, and recasting it in scaled variables yields

$$Df_{1,k} = C_k J_0(\tilde{f}|\tilde{Z}_k(\tilde{\omega})|\tilde{T}_k w)\sin[\tilde{S}_k^0(\epsilon)w + \gamma_k]. \quad (8)$$

This result provides a general description of the absorption spectrum of a Rydberg atom in a weak oscillating electric field. Comparing Eq. (8) with Eq. (5), we see that the perturbation weakens the recurrence amplitude by a factor given by a Bessel function. The argument of the Bessel function is the perturbation to the semiclassical phase of the extreme orbits in the family—proportional to the product of the perturbing field and the ac dipole moment of the unperturbed orbit.

In principle one must evaluate $\tilde{Z}_k(\tilde{\omega})$ separately for each unperturbed closed orbit. However, in the regime observed here, the z motion of every orbit is similar to that of the parallel orbit or one of its repetitions. We approximate $\tilde{Z}_k(\tilde{\omega})$ by that of the corresponding repetition of the parallel orbit in what we call the restricted semiclassical theory. Additionally, the ac dipole moment for the nth repetition of the parallel orbit is related to that for the 1st repetition:

$$|\tilde{Z}_n(\tilde{\omega})| = |\tilde{Z}_1(\tilde{\omega})|\left|\frac{\sin(n\tilde{\omega}\tilde{T}_1/2)}{\sin(\tilde{\omega}\tilde{T}_1/2)}\right|. \quad (9)$$

Using these approximations in (8), we find that every recurrence peak is weakened by a factor a_n given by

$$a_n = J_0^2\left(\tilde{f}\tilde{Z}_1(\tilde{\omega})\left|\frac{\sin(n\tilde{\omega}\tilde{T}_1/2)}{\sin(\tilde{\omega}\tilde{T}_1/2)}\right|\tilde{T}_1 w\right) \equiv J_0^2(c_n\tilde{f}). \quad (10)$$

(In our experiment the range of w is small so it can be taken to be a constant.) We shall refer to the quantity c_n defined in Eq. (10) as the falloff coefficient.

We now can examine Figs. 1 and 2 in detail. The dashed lines in Fig. 1 are contours generated from Eq. (10) that show where the recurrence strength should be reduced by 80% ($a_n = 0.2$). The solid line in Fig. 2 shows the location of the first zero of the Bessel function $c_n\tilde{f} \approx 2.4$. This simple calculation predicts the large scale features in the data, and even some details. To further test the experiment and semiclassical theory, we have compared our results with approximate quantum mechanical Floquet calculations of the recurrence spectrum. Details of these calculations will be published elsewhere [16]. Figure 3 compares the experimental recurrence strength of the second repetition in Fig. 2 with the prediction of Eq. (10). The experimental results and

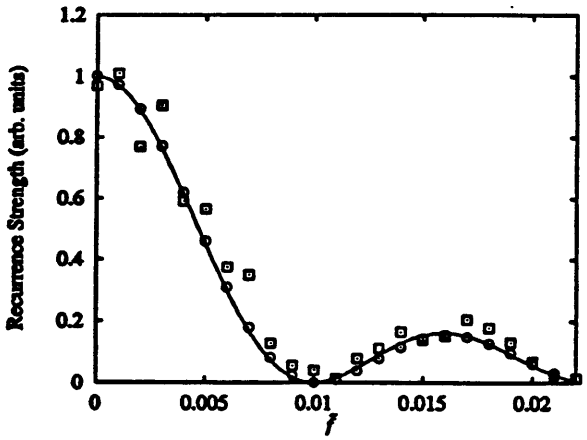

FIG. 3. Recurrence strength of the second repetition at $\epsilon = -0.4$ and $\tilde{\omega} = 0.32$ vs scaled rf field amplitude, $\tilde{f}$. Squares are experimental recurrence strengths, circles are from the Floquet computation. The solid line is the prediction of Eq. (10), scaled to agree near $\tilde{f} = 0$.

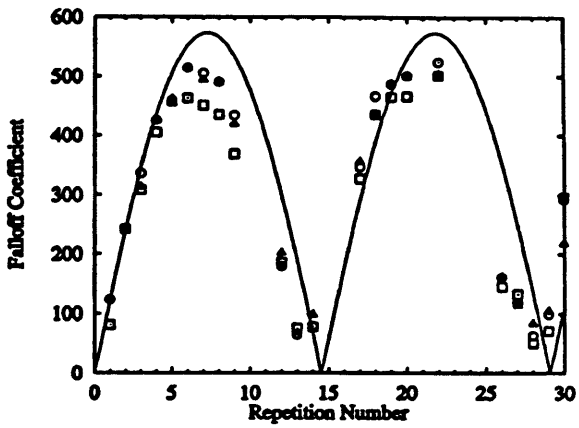

FIG. 4. Falloff coefficient c_n [defined in Eq. (10)] for the first 30 repetitions of the parallel orbit. Squares are experiment, circles are Floquet computation, and solid triangles are the unrestricted semiclassical theory. The solid line is the prediction of the restricted semiclassical theory.

the two theoretical calculations are in generally good agreement.

The restricted semiclassical theory neglects the differences between the parallel and nonparallel orbits. These differences produce, for example, the small discrepancies between the experiment and restricted semiclassical theory seen in Fig. 2. We have included the exact properties of the nonparallel orbits in what we call the unrestricted semiclassical theory. A convenient way to summarize the results is to fit them to the form of Eq. (10) and express the result in terms of the falloff coefficients c_n. Values of c_n from the experiment, the Floquet computation, and the unrestricted semiclassical model are compared with Eq. (10) in Fig. 4. The restricted semiclassical model can be seen to provide a good approximate picture, which is made even better by the unrestricted calculation.

Our recurrence spectra show the systematic elimination of recurrences. We have confirmed these effects in quantum mechanical Floquet calculations. We have shown how these results can be explained to be a consequence of the destructive averaging of orbits returning to the nucleus at different times. These results provide a firm foundation for the investigation and interpretation of recurrence spectra in time-periodic potentials.

The work at MIT is supported by NSF Grant No. PHY-9221489 and ONR Grant No. N00014-96-1-0484, and the work at W&M by NSF Grant No. PHY-9630372 and ONR Grant No. N00014-94-1-0930. N. S. acknowledges support by an AASERT fellowship from ONR. J. G. acknowledges support from the donors of the Petroleum Research Fund administrated by the American Chemical Society and from an award from Research Corporation.

The authors thank the Alexander-von-Humboldt-Stiftung for partial support of this work under the Max-Planck-Forschungspreis program.

[1] A collection of recent work is given in the Special Issue on Atoms in External Fields, edited by J. P. Connerade [J. Phys. B 27, 2659 (1994)].
[2] A. Holle, J. Main, G. Wiebusch, H. Rottke, and K. H. Welge, Phys. Rev. Lett. 61, 161 (1988).
[3] M. L. Du and J. B. Delos, Phys. Rev. A 38, 1896 (1988).
[4] E. B. Bogomol'nyĭ, Zh. Eksp. Teor. Fiz. 96, 487 (1989) [Sov. Phys. JETP 69, 275 (1989)].
[5] J. Main, G. Wiebusch, K. Welge, J. Shaw, and J. B. Delos, Phys. Rev. A 49, 847 (1994).
[6] M. Courtney, H. Jiao, N. Spellmeyer, D. Kleppner, J. Gao, and J. B. Delos, Phys. Rev. Lett. 74, 1538 (1995).
[7] M. Courtney, H. Jiao, N. Spellmeyer, and D. Kleppner, Phys. Rev. Lett. 73, 1340 (1994).
[8] M. Courtney, N. Spellmeyer, H. Jiao, and D. Kleppner, Phys. Rev. A 51, 3604 (1995).
[9] P. A. Dando, T. S. Monteiro, D. Delande, and K. T. Taylor, Phys. Rev. Lett. 74, 1099 (1995).
[10] B. Hüpper, J. Main, and G. Wunner, Phys. Rev. Lett. 74, 2650 (1995).
[11] C. Neumann, R. Ubert, S. Freund, E. Flöthmann, B. Sheehy, K. H. Welge, M. R. Haggerty, and J. B. Delos, Phys. Rev. Lett. 78, 4705 (1997).
[12] We omit a factor of 2π often used in this subfield.
[13] H. B. van Linden van den Heuvell, R. Kachru, N. H. Tran, and T. F. Gallagher, Phys. Rev. Lett. 53, 1901 (1984).
[14] J. Gao and J. B. Delos, Phys. Rev. A 49, 869 (1994).
[15] M. Haggerty *et al.* (to be published).
[16] V. Kondratovich *et al.* (to be published).

Bibliography

[AS72] M. Abramowitz and I.A. Stegun, editors. *Handbook of Mathematical Functions.* National Bureau of Standards, 1972.

[BD95] A. Buchleitner and D. Delande. Nondispersive Electronic Wave Packets in Multiphoton Processes. *Phys. Rev. Lett.*, **75**(8):1487, 1995.

[BGD94] A. Buchleitner, B. Grémaud, and D. Delande. Wavefunctions of atomic resonances. *J. Phys. B*, **27**(13):2663, 1994.

[BK74] J.E. Bayfield and P.M. Koch. Multiphoton Ionization of Highly Excited Hydrogen Atoms. *Phys. Rev. Lett.*, **33**(5):258, 1974.

[Bog89] E.B. Bogomol'nyĭ. Photoabsorption by atoms in external fields near the ionization threshold. *Sov. Phys. JETP*, **69**(2):275, 1989.

[Boh67] N. Bohr. On the quantum theory of line-spectra. *Mémoires de l'Académie Royale des Sciences et des Lettres de Danemark*, Copenhague, Section des Sciences, IV.1, 1-3, pp. 1-36, (1918), reprinted in *Sources of Quantum Mechanics*, pp. 95-137, B.L van der Waerden, ed., Dover, New York, 1967.

[BS57] H.A. Bethe and E.E. Salpeter. *Quantum Mechanics of One- and Two-Electron Atoms.* Springer-Verlag, New York, 1957.

[BS87] R. Blümel and U. Smilansky. Microwave Ionization of Highly Excited Hydrogen Atoms. *Z. Phys. D*, **6**(2):83, 1987.

[CCSG87] G. Casati, B.V. Chirikov, D.L. Shepelyansky, and I. Guarneri. Relevance of classical chaos in quantum mechanics: the hydrogen atom in a monochromatic field. *Phys. Rep.*, **154**(2):77, 1987.

[CJS+95] M. Courtney, H. Jiao, N. Spellmeyer, D. Kleppner, J. Gao, and J.B. Delos. Closed Orbit Bifurcations in Continuum Stark Spectra. *Phys. Rev. Lett.*, **74**(9):1538, 1995.

[CJSK94] M. Courtney, H. Jiao, N. Spellmeyer, and D. Kleppner. Long-Period Orbits in the Stark Spectrum of Lithium. *Phys. Rev. Lett.*, **73**(10):1340, 1994.

[Coo61] J.W. Cooley. An improved Eigenvalue Corrector Formula for Solving the Schrödinger Equation for Central Fields. *Math. Comput.*, **15**(73):363, 1961.

[Cou95] M. Courtney. *Rydberg Atoms in Strong Fields: a Testing Ground for Quantum Chaos.* PhD thesis, Mass. Inst. Tech., 1995.

[CSJK95] M. Courtney, N. Spellmeyer, H. Jiao, and D. Kleppner. Classical, semiclassical, and quantum dynamics in the lithium Stark system. *Phys. Rev. A*, **51**(5):3604, 1995.

[CTDL77] C. Cohen-Tannoudji, B. Diu, and F. Laloë. *Quantum Mechanics*, volume 2. John Wiley & Sons, New York, 1977.

[DBG91] D. Delande, A. Bommier, and J.C. Gay. Positive-Energy Spectrum of the Hydrogen Atom in a Magnetic Field. *Phys. Rev. Lett.*, **66**(8):141, 1991.

[DD88a] M.L. Du and J.B. Delos. Effect of closed classical orbits on quantum spectra: Ionization of atoms in a magnetic field. II. Derivation of formulas. *Phys. Rev. A*, **38**(4):1913, 1988.

[DD88b] M.L. Du and J.B. Delos. Effect of closed classical orbits on quantum spectra: Ionization of atoms in a magnetic field. I. Physical picture and calculations. *Phys. Rev. A*, **38**(4):1896, 1988.

[DG84] D. Delande and J.C. Gay. Group theory applied to the hydrogen atom in a strong magnetic field. Derivation of the effective diamagnetic Hamiltonian. *J. Phys. B.*, **17**(11):L335, 1984.

[DMDT95] P.A. Dando, T.S. Monteiro, D. Delande, and K.T. Taylor. Beyond Periodic Orbits: An Example in Nonhydrogenic Atoms. *Phys. Rev. Lett.*, **74**(7):1099, 1995.

[Edm70] A. Edmonds. The Theory of the Quadratic Zeeman Effect. *J. Phys. (Paris)*, **31**(C4):71, 1970.

[Ein17] A. Einstein. Zum Quantensatz von Sommerfeld und Epstein. *Verh. Deutsch. Phys. Ges.*, **19**:82, 1917.

[ER80] T. Ericsson and A. Ruhe. The Spectral Transformation Lanczos Method for the Numerical Solution of Large Sparse Generalized Symmetric Eigenvalue Problems. *Mathematics of Computation*, **35**(152):1251, 1980.

[ERWS88] U. Eichmann, K. Richter, D. Wintgen, and W. Sander. Scaled-Energy Spectroscopy and Its Relation with Periodic Orbits. *Phys. Rev. Lett.*, **61**(21):2438, 1988.

[FMR78] A.G. Fainshtein, N.L. Manakov, and L.P. Rapoport. Some general properties of quasi-energetic spectra of quantum systems in classical monochromatic fields. *J.Phys. B*, **11**(14):2561, 1978.

[FY91] D. V. Fursa and G. L. Yudin. Algebraic theory of the dynamical Stark-Zeeman effect for hydrogenlike atoms. *Phys. Rev. A*, **44**(11):7414, 1991.

[Gal92] T.F. Gallagher. Orderly microwave ionization. In Jean-Claude Gay, editor, *Irregular Atomic Systems and Quantum Chaos.* Gordon and Breach, 1992.

[Gal94] T. Gallagher. *Rydberg Atoms.* Cambridge University Press, Cambridge, 1994.

[Gao] J. Gao (private communication).

[GD92] G. Gao and J.B. Delos. Closed-orbit theory of oscillations in atomic photoabsorption cross sections in a strong electric field. II. Derivation of formulas. *Phys. Rev. A*, **46**(3):1455, 1992.

[GD94] J. Gao and J.B. Delos. Resonances and recurrences in the absorption spectrum of an atom in an electric field. *Phys. Rev. A*, **49**(2):869, 1994.

[GD97] J. Gao and J.B. Delos. Quantum manifestations of bifurcations of closed orbits in the photoabsorption spectra of atoms in electric fields. *Phys. Rev. A*, **56**(1):356, 1997.

[GK87] V. Gontis and B. Kaulakys. Stochastic dynamics of hydrogenic atoms in the microwave field: modelling by maps an quantum description. *J. Phys. B*, **20**(19):5051, 1987.

[GL78] S. Gerstenkorn and P. Luc. *Atlas of the Absorption Spectra of Molecular Iodine for 14,800 cm^{-1} to 20,000 cm^{-1}.* C.N.R.S, Paris, 1978.

[GNS94] Z.D. Gaeta, M.W. Noel, and C.R. Stroud. Excitation of the Classical-Limit State of an Atom. *Phys. Rev. Lett.*, **73**(5):636, 1994.

[Gol80] H. Goldstein. *Classical Mechanics.* Addison-Wesley, Reading, Massachusetts, 1980.

[GR80] I.S. Gradshteyn and I.M. Ryzhik. *Table of Integrals, Series, and Products.* Academic Press, Inc., Orlando, 1980.

[GT69] W.R.S. Garton and F.S. Tomkins. Diamagnetic Zeeman Effect and Magnetic Configuration Mixing in Long Spectral Series of Ba I. *Astrophys. J.*, **158**(1):839, 1969.

[Gut70] M.C. Gutzwiller. Energy Spectrum According to Classical Mechanics. *J. Math. Phys*, **11**(6):1791, (1970).

[Gut71] M.C. Gutzwiller. Periodic Orbits and Classical Quantization Conditions. *J. Math. Phys*, **12**(3):343, 1971.

[Gut90] M.C. Gutzwiller. *Chaos in Classical and Quantum Mechanics.* Springer-Verlag, New York, 1990.

[Haa91] F. Haake. *Quantum Signatures of Chaos.* Springer-Verlag, Berlin, 1991.

[Hag] M. Haggerty (private communication).

[HD97] M.R. Haggerty and J.B. Delos. Closed orbit theory in a time-dependent system. *Submitted to Phys. Rev. A*, 1997.

[HKTG84] H.B. van Linden van den Heuvell, R. Kachru, N.H. Tran, and T.F. Gallagher. Excitation Spectrum of Na Rydberg States in a Strong Microwave Field: A Connection Between Two Points of View. *Phys. Rev. Lett.*, **53**(20):1901, 1984.

[HMW+88] A. Holle, J. Main, G. Wiebusch, H. Rottke, and K.H. Welge. Quasi-Landau Spectrum of the Chaotic Diamagnetic Hydrogen Atom. *Phys. Rev. Lett.*, **61**(2):161, 1988.

[HMW95] B. Hüpper, J. Main, and G. Wunner. Photoabsorption of Nonhydrogenic Rydberg Atoms in a Magnetic Field: Effects of Core-Scattered Classical Orbits. *Phys. Rev. Lett.*, **74**(14):2650, 1995.

[HT93] E.J. Heller and S. Tomsovic. Postmodern Quantum Mechanics. *Physics Today*, **49**(7):38, 1993.

[Iu91] C. Iu. *Energy Level Structure of Atoms in Magnetic Fields.* PhD thesis, Mass. Inst. Tech., 1991.

[Jia96] H. Jiao. *Experimental and Theoretical Aspects of Quantum Chaos in Rydberg Atoms in Strong Fields.* PhD thesis, Mass. Inst. Tech., 1996.

[Joh59] I. Johansson. The infared spectrum of Li I. *Arkiv för Fysik*, **15**:169, 1959.

[Kas88] M.M. Kash. *Rydberg Atom Diamagnetism.* PhD thesis, Mass. Inst. Tech., 1988.

[KD97a] V. Kondratovich and J.B. Delos. Scaled-Energy Floquet Spectroscopy in a Strong Electric Field: A Semiquantal Calculation of the Recurrence Spectrum. *Submitted to Phys. Rev. A*, 1997.

[KD97b] V. Kondratovich and J.B. Delos. Semiclassical formula for oscillator strengths in atomic spectra. *Phys. Rev. A*, **56**(1):R5, 1997.

[Kel58] J. B. Keller. Corrected Bohr-Sommerfeld Quantum Conditions for Non-separable Systems. *Ann. Phys. (N.Y.)*, **4**:180, 1958.

[KL95] P.M. Koch and K.A.H. van Leeuwen. The importance of resonances in microwave "ionization" of excited hydrogen atoms. *Phys. Rep.*, **255**(5):289, 1995.

[Koc78] P.M. Koch. Resonant States in the Nonperturbative Regime: The Hydrogen Atom in an Intense Electric Field. *Phys. Rev. Lett.*, **41**(2):99, 1978.

[Kon] V. Kondratovich (private communication).

[Lan50] C. Lanczos. An Iteration Method for the Solution of the Eigenvalue Problem of Linear Differential and Integral Operators. *J. Res. Nat. Bur. Stand.*, **45**(4):255, 1950.

[Lib84] R.L. Liboff. The correspondence principle revisited. *Phys. Today*, **37**(2):50, 1984.

[LP78] J.G. Leopold and I.C. Percival. Microwave Ionization and Excitation of Rydberg Atoms. *Phys. Rev. Lett.*, **41**(14):944, 1978.

[MRB+94] F.L. Moore, J.C. Robinson, C. Bharucha, P.E. Williams, and M.G. Raizen. Observation of Dynamical Localization in Atomic Momentum Transfer: A New Testing Ground for Quantum Chaos. *Phys. Rev. Lett.*, **73**(22):2974, 1994.

[MWHW86] J. Main, G. Wiebusch, A. Holle, and K.H. Welge. New Quasi-Landau Structure of Highly Excited Atoms: The Hydrogen Atom. *Phys. Rev. Lett.*, **57**(22):2789, 1986.

[MWW+94] J. Main, G. Wiebusch, K.H. Welge, J. Shaw, and J.B. Delos. Recurrence spectroscopy: Observation and interpretation of large-scale structure in the absorption spectra of atoms in magnetic fields. *Phys. Rev. A*, **49**(2):847, 1994.

[NUF+97] C. Neumann, R. Ubert, S. Freund, E. Flöthmann, B. Sheehy, K. H. Welge, M. R. Haggerty, and J. B. Delos. Symmetry Breaking in Crossed Magnetic and Electric Fields. *Phys. Rev. Lett.*, **78**(25):4705, 1997.

[Ort67] J. Ortega. The Givens-Householder method for symmetric matrices. In A. Ralston and H.S. Wilf, editors, *Mathematical Methods for Digital Computers*. Wiley, 1967.

[PTVF92] W.H. Press, S.A. Teukolsky, W.T. Vetterling, and B.P. Flannery. *Numerical Recipes in C*. Cambridge University Press, Cambridge, 1992.

[RBM+95] J.C. Robinson, C. Bharucha, F.L. Moore, R. Jahnke, G.A. Georgakis, Q. Niu, and M.G. Raizen. Study of Quantum Dynamics in the Transition from Classical Stability to Chaos. *Phys. Rev. Lett.*, **74**(20):3963, 1995.

[RFW91] G. Raithel, M. Fauth, and H. Walther. Quasi-Landau resonances in the spectra of rubidium Rydberg atoms in crossed electric and magnetic fields. *Phys. Rev. A*, **44**(3):1898, 1991.

[Sak85] J.J. Sakurai. *Modern Quantum Mechanics*. Addison-Wesley Pubishing Company, Inc., Redwood City, California, 1985.

[Sam73] Hideo Sambe. Steady States and Quasienergies of a Quantum-Mechanical System in an Oscillating Field. *Phys. Rev. A*, **7**(6):2203, 1973.

[Shi65] Jon H. Shirley. Solution of the Schrödinger Equation with a Hamiltonian Periodic in Time. *Phys. Rev.*, **138**(4B):B979, 1965.

[SKH+97] N. Spellmeyer, D. Kleppner, M. Haggerty, V. Kondratovich, J. Delos, and J. Gao. Recurrence Spectroscopy of a Dynamical System: a Rydberg Atom in an Oscillating Field. *Phys. Rev. Lett.*, **79**(9):1650, 1997.

[STG88] R.C. Stoneman, D.S. Thomson, and T.F. Gallagher. Microwave multiphoton transitions between Rydberg states of potassium. *Phys. Rev. A*, **37**(5):1527, 1988.

[Tab89] M. Tabor. *Chaos and Integrability in Nonlinear Dynamics.* Wiley Inter-Science, Tabor, 1989.

[VWH93] T. van der Veldt, W. Wassen, and W. Hogervorst. Quasi-Landau Structure of Diamagnetic Helium Rydberg Atoms. *Europhys. Lett.*, **21**(9):903, 1993.

[Wel89] G.R. Welch. *High Resolution Spectroscopy of Rydberg Atoms in a Magnetic Field.* PhD thesis, Mass. Inst. Tech., 1989.

[WNLH88] A. ten Wolde, L.D. Noordam, A. Lagendijk, and H.B. van Linden van den Heuvell. Observation of Radially Localized Atomic Electron Wave Packets. *Phys. Rev. Lett.*, **61**(18):2099, 1988.

[YRM+93] J.A. Yeazell, G. Raithel, L. Marmet, H. Held, and H. Walther. Observation of Wave Packet Motion along Quasi-Landau Orbits. *Phys. Rev. Lett.*, **70**(19):2884, 1993.

[YS88] J.A. Yeazell and C.R. Stroud. Observation of Spatially Localized Atomic Electron Wave Packets. *Phys. Rev. Lett.*, **60**(15):1494, 1988.

[ZLKK79] M.L. Zimmerman, M.G. Littman, M.M. Kash, and D. Kleppner. Stark structure of the Rydberg states of alkali-metal atoms. *Phys. Rev. A*, **20**(6):2251, 1979.

Acknowledgments

As many years of formal education come to an end, I look back with the feeling that, overall, it has been a great experience. A principal reason for this has been that I have been surrounded by many wonderful people, and have enjoyed working and interacting with them. The work described in this thesis would not have been possible without the assistance of many people. Because it is impossible to thank everyone who has assisted me, I apologize to those whom I omit.

I joined the Kleppner group when the chaos experiment was run by Michael Courtney and Hong Jiao. They taught me most of what I know about running the experiment, were good to me, and made me feel a part of the team from the beginning. I particularly thank Hong. His presence made life around the lab interesting and enjoyable, and he gave me much help as I took over the experiment. My progress would have been much slower without his help.

The other Kleppner group members in Building 26 when I began here were Robert Lutwak and Jeff Holley. Robert was an invaluable resource to everyone on the floor. He always dropped everything to answer any questions I had, be they about the experiment, computers, or anything else. He was particularly helpful in teaching me some of the secrets of UNIX system administration. I also thank him and his wife Elizabeth for the many rides in the evening, as well as the occasional meals at their house.

Jeff Holley has been a pleasure to work with. His easy-going spirit gives the lab a nice atmosphere. Jeff is very smart, and has deep insight into most everything. He is the most patient person I know, and this is reflected in the quality of his work. I especially thank him for arranging the party after my thesis defense. Joel DeVries

joined the group shortly after I did, and we were office-mates for a few years. I have enjoyed his company and friendship, and wish him the best when he inherits a difficult experiment.

Daniel Ripin worked on this experiment for a year. I thank him for his assistance, and wish him success in his current research. I have had the good fortune to share an office with Lyndie Williamson for the last year. I have enjoyed all our conversations, and hope she goes on to achieve great things.

I thank all the other people who have inhabited Building 26 during my time here. Among these are Michael Andrews, Michael Bradley, Michael Chapman, Ken Davis, Klaasjan van Druten, Dallin Durfee, Troy Hammond, Shin Inouye, David Kokarowski, Dan Kurn, Alan Lenef, Hans-Joachim Miesner, Marc-Oliver Mewes, Fred Palmer, Trey Porto, Simon Rainville, Chandra Raman, Richard Rubenstein, Ed Smith, and Chris Townsend. They have all made it a great place to work.

Dale Fried, Tom Killian, David Landhuis, Steve Moss, Adam Polcyn, and Lorenz Willmann compose the Building 13 contingent of the Kleppner group. They have always been a good resource for ideas, equipment, and friendship.

There have been many others who have made my stay at MIT enjoyable. I thank Bernard Beard, Andrew Berger, Danielle Kleinberg, Arthur Lue, and Steve Nahn their friendship and help studying physics. All are keen physicists and just great people. I have learned as much about life as about physics from them. I look forward to continuing our friendship far into the future.

Peggy Berkowitz and Pat Solakoff in the Graduate Physics Office have made MIT a nice place to be. I thank Carol Costa for lending a secretarial hand.

John Brandenberger of Lawrence University spent a year on sabbatical in our group. I learned a lot from him, and valued and enjoyed his advice and assistance. Ted Ducas of Wellesley College has visited the group every Friday. Fridays won't be the same without lunch with Ted at the Royal East.

I have had the good fortune of interacting with Prof. John Delos of William and Mary, and his coworkers, Michael Haggerty, Vladimir Kondratovich, and Jing Gao. It is only with their assistance that the data were understood. I thank Profs. Michel

Baranger and Ray Ashoori for serving on my thesis committee.

I thank the group in Bielefeld, Germany, Eugen Flöthmann, Stefan Freund, Cornelius Neumann, Ralf Übert, and Prof. Karl Welge, for their hospitality during my visits.

I thank my family for their many forms of support. My mother and father, Marjorie and Robert, have always had encouraging words for me, and without their many years of encouragement I could not have achieved this goal. My brother Grant has been similarly supportive. Few people have had better big brothers. I also thank my sister-in-law Sarah for her support and encouragement.

I thank Grace Carpenter, whom I met as my time here was coming to an end, for her love and friendship.

I thank Beatrice Kleppner for her kind hospitality during the fall visits to Vermont and at the parties in Belmont.

Finally, I thank Dan Kleppner. Dan gave me a job here, paid me, and motivated my research. Few physicists have achieved what Dan has done—to run a successful research group almost exclusively using graduate students. Dan teaches as any good teacher or parent does—by example. He works harder and has a schedule busier than I would ever be able to maintain, and yet he has (almost) always had time to talk with me. I thank him for giving me so many ideas to work with, and then giving me the freedom to follow the ones I thought were best. Dan conceived the idea of applying an oscillating field, and always seemed certain that there would be interesting results. I thank him for his careful editing of this thesis. Finally, I thank him for always giving me an honest opinion, letting me know when he was not satisfied with something, for without such words I would have learned much less in graduate school. I will miss the opportunity of doing physics with Dan.